

Internal Report  
DESY F35D-95-04  
July 1995

# Measurement of the Proton Diffractive Structure Function at HERA Using the ZEUS Detector

by

M. Przybycień



**DESY behält sich alle Rechte für den Fall der Schutzrechtserteilung und für die wirtschaftliche Verwertung der in diesem Bericht enthaltenen Informationen vor.**

**DESY reserves all rights for commercial use of information included in this report, especially in case of filing application for or grant of patents.**

**"Die Verantwortung für den Inhalt dieses  
Internen Berichtes liegt ausschließlich beim Verfasser"**

# Measurement of the Proton Diffractive Structure Function at HERA Using the ZEUS Detector

PhD Thesis

Mariusz Przybycień ✓

Institute of Physics, Jagellonian University,  
ul. Reymonta 4, 30-059 Cracow, Poland

## Abstract

This thesis presents a measurement of the proton diffractive structure function in  $ep$  deep inelastic scattering at HERA using the ZEUS detector. The events used in the analysis are characterized by a gap in pseudorapidity between the diffractively scattered proton and the rest of hadronic system. The proton diffractive structure function  $F_2^{diff}$  is measured as a function of  $x_P$  (momentum fraction of the proton carried by the pomeron), of  $\beta$  (momentum fraction of the pomeron carried by the struck quark) and of  $Q^2$ . The data confirm factorization of  $F_2^{diff}(x_P, \beta, Q^2)$  to the pomeron flux factor and to the pomeron structure function. The  $x_P$  dependence of  $F_2^{diff}$  in all  $\beta$  and  $Q^2$  bins has the same form  $(x_P)^b$  where  $b = -1.25 \pm 0.07(\text{stat}) \pm 0.09(\text{sys})$ . The  $\beta$  dependence of the pomeron structure function  $F_2^P(\beta, Q^2)$  requires both a hard and a soft component for the quark content of the pomeron. For fixed  $\beta$  values the data approximately scale with  $Q^2$ . This also supports the idea of the pomeron in the diffractive  $ep$  deep inelastic scattering behaving effectively as a particle, which consists of point-like constituents.



# Contents

<b>1</b>	<b>Introduction</b>	<b>1</b>
<b>2</b>	<b>Diffractive <math>ep</math> deep inelastic scattering</b>	<b>2</b>
2.1	Deep inelastic scattering . . . . .	2
2.1.1	Kinematics in DIS . . . . .	2
2.1.2	DIS cross sections . . . . .	4
2.2	Diffractive hard scattering . . . . .	6
2.2.1	Kinematics . . . . .	8
2.2.2	Diffractive structure function . . . . .	9
2.3	The pomeron and its phenomenological models . . . . .	10
2.3.1	Ingelman–Schlein model . . . . .	10
2.3.2	Donnachie–Landshoff model . . . . .	11
2.3.3	Nikolaev–Zakharov model . . . . .	12
<b>3</b>	<b>ZEUS – a detector at HERA</b>	<b>16</b>
3.1	The HERA accelerator . . . . .	16
3.2	The ZEUS detector . . . . .	16
3.2.1	Central tracking system . . . . .	18
3.2.2	Calorimeter . . . . .	19
3.2.3	Other components . . . . .	23
3.3	Luminosity measurement in 1993 . . . . .	23
3.4	The ZEUS trigger and the data acquisition system in 1993 . . . . .	25
<b>4</b>	<b>Reconstruction of kinematics at HERA</b>	<b>29</b>
4.1	Reconstruction methods . . . . .	29
4.2	Smearing of kinematic variables . . . . .	31

<b>5 Monte Carlo simulation</b>	<b>36</b>
<b>6 Data selection</b>	<b>38</b>
6.1 Selection of diffractive NC DIS events . . . . .	38
6.2 Background estimation . . . . .	41
6.2.1 Photoproduction background . . . . .	41
6.2.2 Beam-gas interactions . . . . .	43
6.2.3 Non-diffractive DIS background . . . . .	43
6.2.4 Background from double diffractive events . . . . .	43
<b>7 Characteristics of the diffractive DIS events</b>	<b>45</b>
7.1 Estimation of diffractive fraction in the DIS cross section . . . . .	45
7.2 Inclusive properties of events with a large rapidity gap . . . . .	47
<b>8 Determination of <math>F_2^{diff}(x_P, \beta, Q^2)</math></b>	<b>50</b>
8.1 Bin selection and acceptances . . . . .	50
8.2 Unfolding procedure . . . . .	55
8.3 Presentation of the final results . . . . .	57
8.4 Systematic errors . . . . .	59
8.5 Test of the factorization theorem . . . . .	60
8.6 Comparison with theoretical models . . . . .	66
<b>9 Conclusions</b>	<b>69</b>
<b>Acknowledgments</b>	<b>71</b>
<b>Bibliography</b>	<b>72</b>

# 1 Introduction

Our present understanding of the structure of matter has been established in early fixed target lepton scattering experiments. On the basis of the results from these experiments the theory of strong interactions, Quantum Chromodynamics (QCD), was developed. The theory describes interactions between quarks and gluons in hadrons.

In 1992 the new electron-proton collider HERA (**H**adron **E**lektron **R**ing **A**nlage) at DESY (**D**eutsches **E**lektronen **S**ynchrotron) in Hamburg has been put into operation. HERA provides collisions between 26.7 GeV electrons and 820 GeV protons. The energy available in the center of mass system, 296 GeV, is one order of magnitude higher than the one at previous fixed target experiments. This new energy range allows to measure the structure of the proton at Bjorken  $x$  down to  $\sim 10^{-4}$ , which is two orders of magnitude smaller than previously.

Presently two experiments, H1 and ZEUS, are performed at the HERA collider. First results from the two collaborations concerning deep inelastic scattering cross section and proton structure function have been already published [1, 2]. Recently both collaborations have observed in the deep inelastic scattering (DIS) event sample a fraction of events with a large gap in pseudorapidity between the scattered proton and the hadronic activity in the calorimeter [3, 4]. This class of DIS events can be explained by the hypothesis that the DIS process involves the interaction of the virtual photon with a colorless object in the proton like the pomeron. Evidence for a partonic structure of the pomeron was first observed by the UA8 Collaboration [5].

This thesis presents the general characteristics of events with large rapidity gap and the method and the measurement of the proton diffractive structure function, the pomeron flux factor and the pomeron structure function, using the ZEUS detector.

In Section 2 we present a brief description of the QCD and general characteristics of standard and diffractive deep inelastic scattering processes. The most popular models of the diffractive scattering are also reviewed. General design parameters of the HERA collider and a description of the relevant in this analysis ZEUS detector components are presented in Section 3. The Section 3 explains also the method of the luminosity measurement in the ZEUS experiment and the ZEUS trigger and data acquisition system. Different reconstruction methods of the kinematic variables at HERA are compared in Section 4. The Monte Carlo simulation and reconstruction programs are described in Section 5. Selection cuts used to obtain a clean DIS sample and to extract the diffractive subsample are presented in Section 6. In that Section we also explain methods of estimating and removing main background sources from the data sample. A general characteristic of the inclusive properties of the diffractive events are reviewed in Section 7. The contribution of diffractive events to the total DIS cross section is evaluated. Data are compared with the MC predictions. In Section 8 we present the method used to unfold the data and to extract the diffractive structure function of the proton. The measured  $F_2^{diff}(x_P, \beta, Q^2)$  is then factorised to the flux of pomerons in the proton and to the pomeron structure function. A summary of the results presented in this thesis is given in Section 9.

## 2 Diffractive $ep$ deep inelastic scattering

### 2.1 Deep inelastic scattering

One of the methods of testing QCD is probing the parton structure of a nucleon with a pointlike lepton. In  $ep$  deep inelastic scattering (DIS) at high energies the electron interacts with the constituents of the proton. The effective probe of the structure within the nucleon is the exchanged virtual vector boson carrying the four-momentum  $q$ , where  $-q^2 \equiv Q^2 > 0$ . The resolving power of this probe is the wavelength  $1/Q$  (we assume  $\hbar = c = 1$ ) and so the degree of structure revealed increases with  $Q^2$ . The DIS at small Bjorken  $x$  is probing the parton distributions in the proton in a limit where the momentum fraction carried by a parton is very small. The understanding of the parton distributions in that limit is one of the most interesting problems in QCD [10, 11].

In most cases the proton breaks up during the interaction and many particles are produced in the final state. We can distinguish two different types of  $ep$  DIS:

$$e + p \rightarrow e + X \quad \text{and} \quad e + p \rightarrow \nu + X$$

where  $X$  represents the hadronic final state. The first reaction is known as a neutral current (NC) DIS, because the intermediate vector boson is neutral ( $\gamma, Z^0$ ), whereas in the second process, so called charged current (CC) DIS, the intermediate vector boson is charged ( $W^\pm$ ) and the initial electron converts to a neutrino.

In the following we will restrict to the NC DIS processes, where the momentum transfer is high ( $Q^2 \gg \Lambda^2$ ). We confine our discussion to the case where only a single virtual photon is exchanged, because this process is most significant at HERA energies. The analysis is also restricted to collisions with unpolarized beams.

#### 2.1.1 Kinematics in DIS

A schematic view of the NC DIS is shown in Fig 2.1. The incident electron carrying a four-momentum  $k$  is scattered off the proton with a four-momentum  $p$  through the exchange of a single virtual photon whose four-momentum is denoted by  $q$ . The scattered electron has a four-momentum  $k'$  and  $X$  denotes the hadronic final state. The analysis in this thesis is restricted to the inclusive NC DIS, so we are not interested in identifying specific particles in the hadronic final state  $X$ .

Below we introduce variables describing the DIS kinematics. The virtuality of the exchanged photon sets the scale of the interaction because the resolution is proportional to  $1/|q|$ . Using the notation given in Fig 2.1 we define:

$$Q^2 \equiv -q^2 = -(k - k')^2 > 0 \tag{2.1}$$

In fixed target experiments the most useful reference frame was the proton rest frame, which was simultaneously the laboratory frame (LAB). In the case of colliders both beam

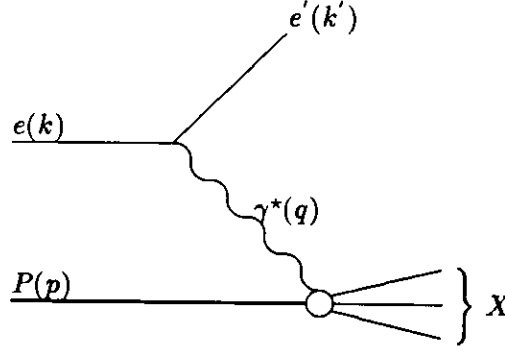


Figure 2.1: Schematic view of  $ep$  DIS in one photon exchange approximation.

particles are moving in the LAB frame. This results in a much more higher center of mass energies which are available (for example the HERA collider is equivalent to the fixed target experiment with 52 TeV electrons colliding with protons at rest). In the proton rest frame we can express the four-momentum transfer squared  $q^2$  by the energy  $E'$  and the polar angle  $\theta$  of the scattered electron. Neglecting the mass of the electron we obtain:

$$-q^2 = 4EE' \sin^2 \frac{\theta}{2} \quad (2.2)$$

In the same frame the energy loss of the lepton reads:

$$\nu = \frac{p \cdot q}{M} = E - E' \quad (2.3)$$

It is useful to introduce two Bjorken scaling variables. The first one reads:

$$x = \frac{Q^2}{2p \cdot q} = \frac{-t}{u + s} \quad (2.4)$$

and is interpreted as the fraction of the proton momentum carried by the struck quark in the parton model. The second variable:

$$y = \frac{p \cdot q}{p \cdot k} = \frac{u + s}{s} = \frac{Q^2}{xs} \quad (2.5)$$

is the fraction of the energy lost by the electron in the frame for which the proton is at rest. In equations (2.4) and (2.5),  $s$ ,  $u$ ,  $t$  are the commonly used Mandelstam variables. In particular,  $s$  is the center of mass energy squared, which by neglecting the proton mass, equals:

$$s = (k + p)^2 = 4EE_p \quad (2.6)$$

where  $E$  and  $E_p$  are energies of the electron and proton beams respectively. The invariant mass of the hadronic final state  $X$  is given by:

$$W^2 = (p + q)^2 = Q^2 \left( \frac{1}{x} - 1 \right) + m_p^2 = s + t + u \quad (2.7)$$

where  $m_p$  is the proton mass.

The kinematical variables, only two of which are independent, can be determined either from the scattered electron or from the hadronic system.

### 2.1.2 DIS cross sections

The simplest DIS cross section that one can measure is the inclusive one, when we observe only the scattered electron and sum over all final hadronic states. Using the electron variables, the differential  $ep$  DIS cross section reads [13, 14]:

$$\frac{d^2\sigma}{d\Omega dE'} = \frac{\alpha^2 E'}{q^4 E} l^{\mu\nu} W_{\mu\nu} \quad (2.8)$$

where

$$l_{\mu\nu} = 2(k_\mu k'_\nu + k'_\mu k_\nu + \frac{q^2}{2} g_{\mu\nu})$$

$$W_{\mu\nu}(p, q) = \left[ -\left(g_{\mu\nu} - \frac{q_\mu q_\nu}{q^2}\right) W_1(\nu, Q^2) + \left(p_\mu - \frac{pq}{q^2} q_\mu\right) \left(p_\nu - \frac{pq}{q^2} q_\nu\right) \frac{W_2(\nu, Q^2)}{M^2} \right]$$

are respectively lepton and hadron tensors.  $W_{1,2}$  are Lorentz invariant proton structure functions of scalar variables  $Q^2$  and  $\nu$  in the proton rest frame. It is more convenient, however, to use Lorentz invariant variables defined in the previous paragraph. The cross section can be rewritten in the form:

$$\frac{d^2\sigma}{d\Omega dE'} = \frac{\alpha^2}{4E^2 \sin^4 \frac{\theta}{2}} \left( 2W_1(\nu, Q^2) \sin^2 \frac{\theta}{2} + W_2(\nu, Q^2) \cos^2 \frac{\theta}{2} \right) \quad (2.9)$$

The differential DIS cross section can be expressed in different independent variables using the relations:

$$\nu(s - M^2) \frac{d^2\sigma}{d\nu dQ^2} = \frac{2\pi M\nu}{E'} \frac{d^2\sigma}{d\Omega dE'} = x(s - M^2) \frac{d^2\sigma}{dx dQ^2} \quad (2.10)$$

If large  $Q^2$  virtual photons resolve point-like constituents inside the proton then the structure functions  $W_1$  and  $\nu W_2$  become functions of the single variable  $x = \frac{Q^2}{2M\nu}$ :

$$MW_1(\nu, Q^2) \rightarrow F_1(x) \quad (2.11)$$

$$\nu W_2(\nu, Q^2) \rightarrow F_2(x) \quad (2.12)$$

This property, first postulated by Bjorken [6], and called *scale invariance*, is experimentally observed [7] for  $Q^2 > 1 \text{ GeV}^2$ . In the naive parton model the proton consists of point-like partons, from which the electron scatters coherently. This model provides an explanation for the observed scaling behavior. Callan and Gross predicted that for spin 1/2 partons the ratio of structure functions  $2xF_1/F_2$  equals one, while for integer spin partons the ratio would equal zero [8]. The data give evidence for spin 1/2 partons [9]. In terms of quark momentum distributions, the structure function in the naive parton model can be written as:

$$2xF_1(x) = F_2(x) = \sum_f e_f^2 [xq_f(x) + x\bar{q}_f(x)] \quad (2.13)$$

where the sum runs over all flavors  $f$ .

If we sum over the momenta of all partons inside the proton we must reconstruct the total momentum of the proton. Data show that about half of the proton momentum is, however, carried by something which does not couple to the photon. Quantum Chromodynamics (QCD) postulates that the missing momentum of the proton is carried by gluons. The gluons carry the strong color force and bind the quarks within the proton. The addition of gluons leads to the  $F_2$  scaling violation and the quark densities become functions of both  $x$  and  $Q^2$ . The  $Q^2$  evolution of the parton densities is determined by perturbative QCD from the Gribov–Lipatov–Altarelli–Parisi (GLAP) equations [15, 16]:

$$\frac{dq_i(x, Q^2)}{d \ln Q^2} = \frac{\alpha_s(Q^2)}{2\pi} \int_x^1 \frac{dy}{y} \left( q_i(y, Q^2) P_{qq} \left( \frac{x}{y} \right) + g(y, Q^2) P_{qg} \left( \frac{x}{y} \right) \right) \quad (2.14)$$

$$\frac{dg(x, Q^2)}{d \ln Q^2} = \frac{\alpha_s(Q^2)}{2\pi} \int_x^1 \frac{dy}{y} \left( \sum_i q_i(y, Q^2) P_{gq} \left( \frac{x}{y} \right) + g(y, Q^2) P_{gg} \left( \frac{x}{y} \right) \right) \quad (2.15)$$

where the strong coupling constant is given by:

$$\alpha_s(Q^2) = \frac{12\pi}{(33 - 2n_f) \ln(Q^2/\Lambda^2)} \quad (2.16)$$

The parameter  $\Lambda$  sets the scale at which perturbative approach is not justified, and  $n_f$  denotes the number of quark flavors. The evolution is governed by the  $P_{qq}$ ,  $P_{gq}$ ,  $P_{qg}$ ,  $P_{gg}$  functions which can be calculated within QCD. The lowest order expressions read:

$$P_{qq}(z) = \frac{4}{3} \left( \frac{1+z^2}{1-z} \right) \quad (2.17)$$

$$P_{qg}(z) = \frac{1}{2} (z^2 + (1-z)^2) \quad (2.18)$$

$$P_{gq}(z) = \frac{4}{3} \frac{1 + (1-z)^2}{z} \quad (2.19)$$

$$P_{gg}(z) = 6 \left( \frac{1-z}{z} + \frac{z}{1-z} + z(1-z) \right) \quad (2.20)$$

The physical meaning of the  $P$  functions is the following. The quantity:

$$\mathcal{P}_{qq}(z, Q^2) \equiv \delta(1-z) + \frac{\alpha_s}{2\pi} P_{qq}(z) \ln \frac{Q^2 + \delta Q^2}{Q^2} \quad (2.21)$$

is interpreted as the probability density of finding a quark inside a quark with fraction  $z$  of the parent quark momentum, when the scale at which partons are observed, is changed by  $\delta Q^2$ , to first order in  $\alpha_s$ . The term  $\delta(1-z)$  corresponds to there being no change in  $q(x, Q^2)$ .

Due to emission of gluons, quarks are given a transverse momentum and the Callan–Gross relation is no longer valid. The correlation between both structure functions is predicted by QCD through the longitudinal structure function  $F_L = F_2 - 2xF_1$ . The compact form of the differential  $ep$  DIS cross section in terms of the structure functions  $F_2$  and  $F_L$  reads:

$$\frac{d^2\sigma}{dx dQ^2} = \frac{4\pi\alpha^2}{xQ^4} \left[ \left(1 - y + \frac{y^2}{2}\right) F_2(x, Q^2) - \frac{1}{2} y^2 F_L(x, Q^2) \right] \quad (2.22)$$

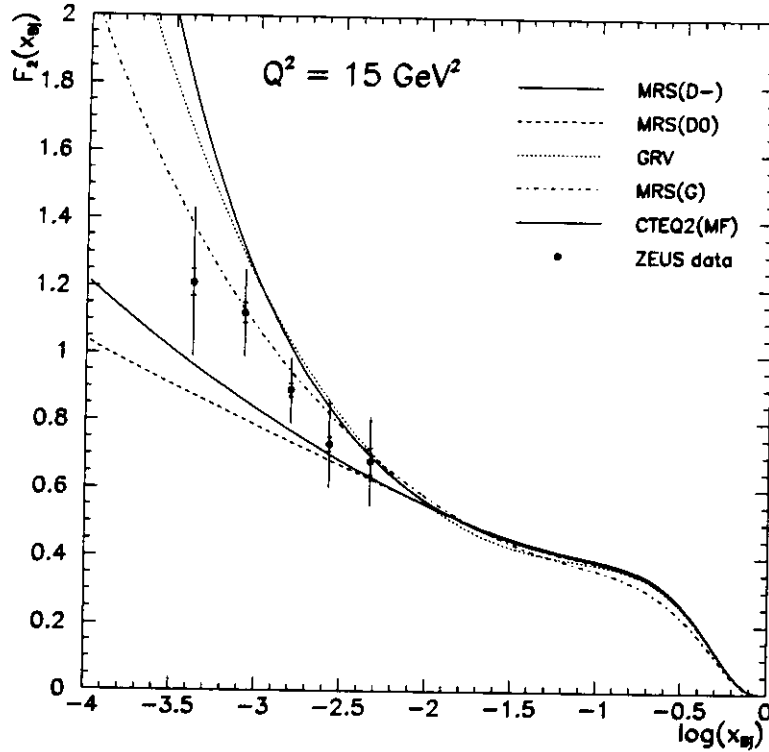


Figure 2.2:  $F_2$  proton structure function for some recent parton parameterizations. 1993 ZEUS data are also shown.

Assuming that the effect of the  $F_L$  term is small we can rewrite the cross section in the simple form:

$$\frac{d^2\sigma}{dx dQ^2} = \frac{2\pi\alpha^2}{xQ^4} [1 + (1-y)^2] F_2(x, Q^2) \quad (2.23)$$

The QCD provides an interpretation of the cross section in terms of quark densities. However, QCD predicts only the  $Q^2$  evolution of the parton distribution, but does not provide any particular form of them. There are many different predictions of the  $F_2$  proton structure function. They are based on the fits to the data with some theoretical assumption. A few of these parameterizations are presented in Fig.2.2.

## 2.2 Diffractive hard scattering

In the standard  $ep$  DIS (standard means the type of DIS described in the previous paragraph), a quark or a gluon is scattered off the proton and it leaves a colored proton remnant because the struck parton itself carries color. There are color strings between the hard scattered partons and the remnant of the proton. This is schematically shown in Fig.2.3 a,b. The hadronization process combines somehow all colored partons to give observed, colorless hadrons. Particles produced in that process fill the region between the hard scattered parton and the proton remnant.

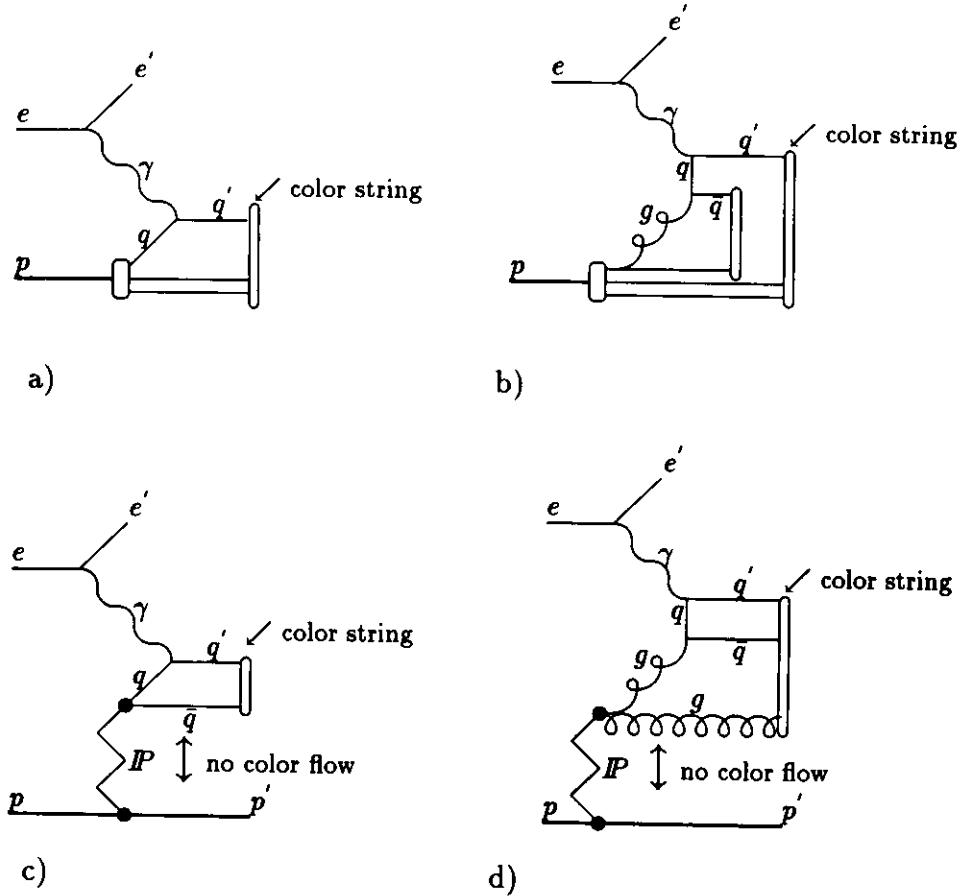


Figure 2.3: *Basic processes for electron–proton and electron–pomeron deep inelastic scattering: a) Lowest order  $\mathcal{O}(\alpha_{em})$  process in ep DIS, b) Gamma–gluon fusion  $\mathcal{O}(\alpha_{em}\alpha_s)$  in ep DIS, c) Lowest order  $\mathcal{O}(\alpha_{em})$  process in eP diffractive DIS, d) Gamma–gluon fusion  $\mathcal{O}(\alpha_{em}\alpha_s)$  in eP diffractive DIS. The color string is indicated on the pictures. Because the pomeron is a colorless object there is no color flow between diffractively scattered proton and particles from the hard interaction.*

However there is a fraction of events in ep DIS which have a large gap in pseudorapidity<sup>1</sup> between the scattered proton and other hadrons. These events cannot be fully explained by standard ep DIS, because in standard DIS the gap can be produced only by QCD fluctuations of the hadronization process. They should appear very seldom, because they are exponentially suppressed<sup>2</sup>.

<sup>1</sup>Pseudorapidity of a particle scattered at the angle  $\theta$  equals to  $\eta = -\ln \tan \frac{\theta}{2}$ .

<sup>2</sup>If we define  $\Delta\eta$  as a difference between the pseudorapidities of the proton remnant and the struck parton, than  $\Delta\eta \sim \ln 1/x$ . In the hadronization process, however, the mean number of produced particles  $\langle n_h \rangle$  increases faster with  $1/x$  as the  $\Delta\eta$ . If we assume Poisson distribution in  $\eta$  for the produced hadrons, the probability that there are no particles in the gap  $\Delta\eta$  is proportional to  $\exp(-\langle n_h \rangle)$ .

Events with large rapidity gaps could be explained by diffractive scattering through an exchange of a colorless object with vacuum quantum numbers, called pomeron. One can imagine that the proton emits a pomeron and that the electron is scattered off the pomeron. In this approach there is no color flow between the scattered proton and the struck parton. Particles resulting from the hard scattering are therefore separated in pseudorapidity from the fast moving proton. This is schematically shown in Fig.2.3 c,d. The formal definition of diffractive processes proposed by Bjorken [17] reads:

*A processes is diffractive if, and only if, there is a large rapidity gap in the produced particle phase space which is not exponentially suppressed.*

### 2.2.1 Kinematics

A schematic view of the diffractive DIS is shown in Fig.2.4. Assuming that diffractive DIS holds through an exchange of the pomeron we have two distinct vertices. The pomeron–proton vertex is characterized by a four–momentum transfer squared  $t = (p - p')^2$  from the initial to the scattered proton and by the fraction  $x_P$  of the longitudinal momentum of the proton carried by the pomeron.  $t$  is also the invariant mass squared of the pomeron. This vertex can be described by the flux  $f_{P/p}(x_P, t)$  of pomerons in the proton. The second vertex,  $\gamma^*$ –pomeron, is characterized by the invariant mass squared of the virtual photon,  $-Q^2$ , and the Bjorken scaling variable:

$$\beta = \frac{Q^2}{2\delta \cdot q} \quad (2.24)$$

where  $\delta$  denotes the four–momentum of the pomeron.  $\beta$  can be interpreted as the fraction of the pomeron momentum carried by the struck parton. In order to parameterize the  $\gamma^*P$  vertex we introduce the pomeron structure function  $F_2^P(\beta, Q^2)$ . We call the pomeron structure function 'hard' when a single constituents carry a large fractions of the total momentum. If most constituents carry a small fraction of the total momentum the pomeron structure function is called 'soft'.

The variables  $\beta$  and  $x_P$  are connected through the relation:

$$x_{Bj} = \beta x_P \quad (2.25)$$

The invariant mass squared of the hadronic final state (without the final state proton) is given by:

$$m_X^2 = (q + p - p')^2 = -Q^2 + syx_P + t \quad (2.26)$$

If we neglect  $t$  in the last formula, we derive the following expression for  $\beta$ :

$$\beta = \frac{Q^2}{Q^2 + m_X^2} \quad (2.27)$$

This formula is independent of the microscopic nature of the  $\gamma^*P$  vertex and can be used in models in which the pomeron is not treated as a particle.

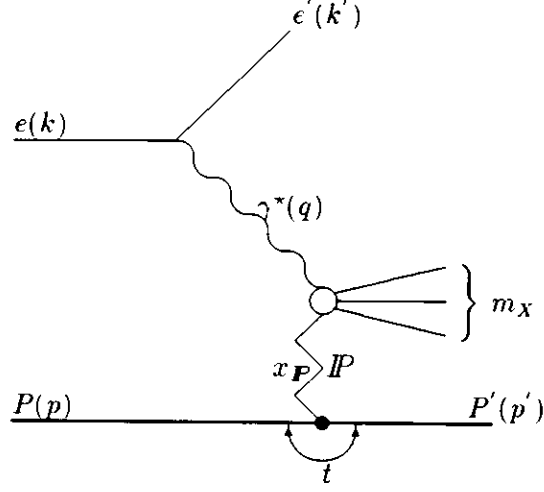


Figure 2.4: Schematic view of diffractive ep deep inelastic scattering.

## 2.2.2 Diffractive structure function

In analogy with ordinary DIS we can write the diffractive DIS cross section as:

$$\frac{d\sigma(ep \rightarrow epX)}{dx_{\mathbf{P}} dt d\beta dQ^2} = \frac{4\pi\alpha^2}{\beta Q^4} \left[ \left(1 - y + \frac{y^2}{2}\right) F_2^{diff}(x_{\mathbf{P}}, t; \beta, Q^2) - \frac{y^2}{2} F_L^{diff}(x_{\mathbf{P}}, t; \beta, Q^2) \right] \quad (2.28)$$

The effect of the  $F_L^{diff}$  term has been studied in reference [18]. It is of importance only for  $\beta$  less than 0.1 or for  $Q^2$  less than 10 GeV<sup>2</sup>, and therefore it has been neglected in this analysis. Neglecting the  $F_L^{diff}$  term, the diffractive cross section can be written in the form:

$$\frac{d\sigma(ep \rightarrow epX)}{dx_{\mathbf{P}} dt d\beta dQ^2} = \frac{2\pi\alpha^2}{\beta Q^4} [1 + (1 - y)^2] F_2^{diff}(x_{\mathbf{P}}, t; \beta, Q^2) \quad (2.29)$$

where the standard proton  $F_2$  structure function has been replaced by a corresponding diffractive one,  $F_2^{diff}$ , with  $x_{\mathbf{P}}$  and  $t$  specifying the diffractive conditions.

$F_2^{diff}$  is given in terms of quark densities which under diffractive conditions specify the probability to find a parton with a momentum fraction  $x$  of the original proton momentum. Assuming factorization these densities are given by the convolution of the probability to find a pomeron with a fraction  $x_{\mathbf{P}}$  of the proton momentum and the probability to find a quark with a momentum fraction  $\beta$  in the pomeron:

$$q^{diff}(x) dx = \int_0^1 dx_{\mathbf{P}} d\beta f_{\mathbf{P}/p}(x_{\mathbf{P}}) q^{\mathbf{P}}(\beta) \delta(x - \beta x_{\mathbf{P}}) \quad (2.30)$$

Integrating over  $\beta$  and summing over quark flavors we can make the replacement:

$$F_2^{diff}(x_{\mathbf{P}}, t; x, Q^2) \longrightarrow F_2^{diff}(x_{\mathbf{P}}, t; \beta, Q^2) = f_{\mathbf{P}/p}(x_{\mathbf{P}}, t) F_2^{\mathbf{P}}(\beta, Q^2) \quad (2.31)$$

The pomeron flux factor can be written as:

$$f_{\mathbb{P}/p}(x_{\mathbb{P}}, t) = \frac{d\sigma/dx_{\mathbb{P}}dt}{\sigma(\mathbb{P}p \rightarrow X)} \quad (2.32)$$

where  $\sigma(\mathbb{P}p \rightarrow X)$  is the total pomeron–proton cross section. The pomeron structure function can be expressed in terms of the density distributions for quarks and antiquarks of flavor  $f$  in the pomeron:

$$F_2^{\mathbb{P}}(\beta, Q^2) = \sum_f e_f^2 [\beta q_f^{\mathbb{P}}(\beta, Q^2) + \beta \bar{q}_f^{\mathbb{P}}(\beta, Q^2)] \quad (2.33)$$

## 2.3 The pomeron and its phenomenological models

Many authors have proposed several models to explain diffractive interactions in  $p\bar{p}$  and  $ep$  scatterings. In this section we present three different approaches to that problem. The models differ not only in quantitative predictions, but also in the understanding of the nature of the diffractive scattering. One of the most important assumption is whether the pomeron can be treated as a particle or not. If the pomeron can be considered as a particle with an internal structure similar to the one of hadrons, one can speak about pomeron structure function and imagines that the virtual photon interacts with a constituent of the pomeron. In this approach, it is even reasonable to consider the diffractive scattering as two distinct processes: emission of the pomeron from the proton and deep inelastic scattering of the electron on the structure of the pomeron. Some models assume that the whole pomeron interacts with the hadronic fluctuation of the virtual photon. In this approach the pomeron is not treated as a particle and the factorization is strongly broken. However even in these models one can introduce some effective structure function and flux of the pomeron.

### 2.3.1 Ingelman–Schlein model

The idea of Ingelman and Schlein is that the proton couples to a spacelike pomeron and this pomeron consists of partons [19]. The pomeron is considered as a quasi-hadron that can be resolved by the virtual photon.

The model assumes the factorization of the proton diffractive structure function to the pomeron flux factor in the proton and to the structure function of the pomeron itself. The pomeron flux factor is defined as a ratio of single diffractive cross section and the pomeron–proton total cross section:

$$f_{\mathbb{P}/p}(x_{\mathbb{P}}, t) = \frac{d\sigma/dx_{\mathbb{P}}dt}{\sigma(\mathbb{P}p \rightarrow X)} = \frac{1}{\sigma(\mathbb{P}p \rightarrow X)} \frac{1}{x_{\mathbb{P}}^p} \sum_{i=1}^3 a_i e^{b_i t} \quad (2.34)$$

The parameters in the exponential  $t$ -dependence are extracted from hadron data. The factor  $1/x_{\mathbb{P}}^p$  with  $p = 1$  corresponds to the conventional  $1/m_X^2$  dependence of diffractive

scattering. The total pomeron–proton cross section equals 2.3 mb. The uncertainty of the flux factor is about 25%.

The model assumes that the pomeron is mainly composed of gluons. However, authors propose different pomeron structure functions. The two extreme possibilities are:

- $\beta_{q/P}(\beta) = \frac{6}{4}\beta(1 - \beta)$  – the pomeron is made of quarks and their distribution is hard (the pomeron is made of few partons).
- $\beta_{g/P}(\beta) = 6(1 - \beta)^5$  – the pomeron is dominated by gluons and their distribution is soft (the pomeron consists of many partons).

The normalization of these structure functions is determined by the momentum sum rule:

$$\sum_i \int_0^1 dx x f(x) = 1 \quad (2.35)$$

where the sum runs over all considered flavors. The pomeron is a much smaller object than a normal hadron. Therefore if the pomeron is essentially a gluonic object, QCD predicts the occurrence of a gluon recombination [20, 21, 22], which leads to a reduction of the gluon density as compared to the conventional GLAP evolution. The recombination is incorporated in the GLR equation [23].

### 2.3.2 Donnachie–Landshoff model

The authors use the data from  $pp$  and  $p\bar{p}$  experiments [24] to extract the phenomenological model of the pomeron [25, 26]. They do not propose a QCD based explanation for diffractive  $ep$  scattering. The pomeron is treated like a photon. In particular it couples to quarks like a  $C = +1$  isoscalar photon.

The coupling of the pomeron to the proton is  $3\beta_0 F_1(t)$  [26]. The parameter  $\beta_0 (= 1.8 \text{ GeV}^{-1})$  is the coupling constant of the pomeron to quarks and the function  $F_1(t)$  is the elastic form factor which is well parameterized by:

$$F_1(t) = \frac{4m_p^2 - 2.8t}{4m_p^2 - t} \left( \frac{1}{1 - t/0.7} \right)^2 \quad (2.36)$$

where  $m_p$  is the proton mass.

The flux of the pomerons in the proton in this model is:

$$f_{P/p}(t, x_P) = \frac{9\beta_0^2}{4\pi^2} [F_1(t)]^2 x_P^{1-2\alpha(t)} \quad (2.37)$$

$\alpha(t)$  is the Regge trajectory of the pomeron, which experiment finds to be:

$$\alpha(t) = 1 + \epsilon + \alpha' t, \quad \epsilon = 0.085, \quad \alpha' = 0.25 \text{ GeV}^{-2} \quad (2.38)$$

The pomeron structure function, by analogy to the photon structure function should have two pieces. There is a part that resembles the structure function of a hadron and there is a part that is peculiar to the photon. The latter corresponds to the box diagram and for the pomeron reads:

$$G_{q/P}^a = 0.2\beta(1 - \beta) \quad (2.39)$$

The other part of the pomeron structure function resembles the structure function of an ordinary hadron. Just as the hadronic piece of the photon structure function is associated with the vector meson dominance, one expects the hadronic piece of the pomeron structure function should be dominated by the vector meson  $f$ . The nonvalence part of this structure function reads:

$$G_{q/P}^b = 0.02 \left( \frac{-t}{-t + 0.36} \right) \left[ \alpha'(-t + 0.36) \right]^{-\epsilon} \beta^{-\epsilon} (1 - \beta)^5 \quad (2.40)$$

while the valence part can be approximated by:

$$G_{q/P}^c = 0.2 \left( \frac{-t}{-t + 0.85} \right) \left[ \alpha'(-t + 0.85) \right]^{0.56} \beta^{0.56} (1 - \beta) \quad (2.41)$$

For  $\beta > 0.1$  the first term  $G_{q/P}^a$  dominates and the last two terms can be neglected. The model predicts that the diffractive cross section is a few percent of the total DIS cross section.

### 2.3.3 Nikolaev-Zakharov model

The model proposed by Nikolaev and Zakharov [27, 28] assumes the existence of the perturbative QCD pomeron. The diffractive  $ep$  scattering holds as a photon diffractive dissociation on the proton. The authors have developed a detailed description of diffractive DIS in terms of the diffractive excitation of multiparton Fock space of the photon:

$$|\gamma\rangle = |\gamma\rangle_{bare} + |q\bar{q}\rangle + |q\bar{q}g\rangle + \dots \quad (2.42)$$

Exchange of the pomeron can be imagined as an exchange of the two noninteracting and seemingly uncorrelated gluons. A schematic view of the  $ep$  diffractive scattering proposed by the model is shown in Fig.2.5.

Although the pomeron in this model is not treated as a particle with a well defined partonic structure, the authors, however, propose a two-component pomeron structure function [29], whose both parts evolve according to the GLAP equations, respectively from the initial valence quark-antiquark and the valence gluon-gluon components. For these two components the fluxes of the pomeron in the proton are different. This leads to a specific breaking of the factorization.

Diffractive excitation of the  $q\bar{q}$  Fock state of the photon (we take into account only transverse photons) reads:

$$\left. \frac{d\sigma_D(\gamma^* \rightarrow q\bar{q})}{dt dM^2} \right|_{t=0} = \frac{1}{16\pi} \int_0^1 dz d^2\vec{r} |\Psi_{\gamma^*}(Q^2, z, r)|^2 \sigma(x, r)^2 \quad (2.43)$$

where  $\vec{r}$  is the transverse separation of the quark and antiquark in the photon,  $z$  and  $(1-z)$  are partitions of photon's lightcone momentum between quark and antiquark.  $\sigma(x, r)$  is the dipole cross section for scattering on the proton target [30], and  $|\Psi_{\gamma^*}(Q^2, z, r)|$  is the dipole distribution in the photon and was calculated in [31].

One can reinterpret the cross section (2.43) as DIS on the valence  $q\bar{q}$  of the pomeron. In that sense the  $x_P$  and  $\beta$  dependence can be factorized and we can write down the convolution representation:

$$x_P \frac{d\sigma_D(\gamma^* \rightarrow q\bar{q})}{dt dx_P} \Big|_{t=0} = \frac{\sigma_{tot}(pp)}{16\pi} \frac{4\pi^2 \alpha_{em}}{Q^2} \phi_P(x_P) F_{val}^P(\beta), \quad (2.44)$$

in which the valence  $q\bar{q}$  structure function of the pomeron is:

$$F_{val}^P(\beta) = 0.27\beta(1-\beta) \quad (2.45)$$

and the flux function is defined by:

$$\phi_P(x_P) = \frac{\int_0^1 dz \int d_2\vec{r} |\Psi_{\gamma^*}(Q^2, z, r)|^2 \sigma(x_P, r)^2}{\int_0^1 dz \int d_2\vec{r} |\Psi_{\gamma^*}(Q^2, z, r)|^2 \sigma(x_P^0, r)^2} \quad (2.46)$$

The authors propose the normalization  $\phi_P(x_P^0 = 0.03) = 1$ .

The second part of the pomeron structure function originates from the gluonic component of the pomeron. This part can be approximated by:

$$F_{sea}^P(\beta) = 0.063(1-\beta)^2 \quad (2.47)$$

The sea component of the pomeron structure function is endowed with the flux factor,  $f_P(x_P)$ , which differs from the  $\phi_P(x_P)$  and reads:

$$f_P(x_P) = \frac{1}{2\pi^4 \cdot 0.56} \cdot \left(\frac{9}{8}\right)^3 \cdot \int dr^2 \left[ \frac{\sigma(x_P, r)}{r^2} \right]^2 F(\mu_G r) \quad (2.48)$$

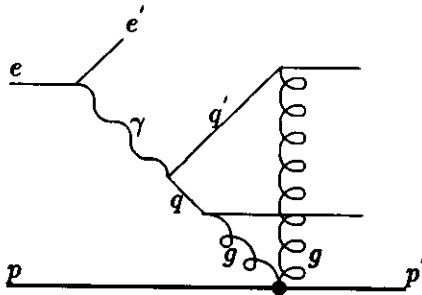


Figure 2.5: Pomeron exchange in the Nikolaev-Zakharov model.

where the form factor  $F(z) = z^2[K_1(z)^2 + zK_1(z)K_0(z) + \frac{1}{2}z^2K_0(z)^2]$ , and  $\mu_G=0.75$  GeV sets the correlation radius for the perturbative gluons. Functions  $\phi_{\mathbf{P}}(x_{\mathbf{P}})$  and  $f_{\mathbf{P}}(x_{\mathbf{P}})$  can be well parameterized by:

$$\phi_{\mathbf{P}}(x_{\mathbf{P}}), f_{\mathbf{P}}(x_{\mathbf{P}}) = \left(\frac{x_{\mathbf{P}}^0}{x_{\mathbf{P}}}\right)^{p_1} \cdot \left(\frac{x_{\mathbf{P}} + p_3}{x_{\mathbf{P}}^0 + p_3}\right)^{p_2} \quad (2.49)$$

with parameters shown in the table:

function	$p_1$	$p_2$	$p_3$
$\phi_{\mathbf{P}}(x_{\mathbf{P}})$	0.259	0.2142	0.00149
$f_{\mathbf{P}}(x_{\mathbf{P}})$	0.58	0.48	0.0023

Both parts of the pomeron structure function can be evolved with the GLAP equations taking as the starting point  $Q^2=10$  GeV. Predictions of the model for both parts of the structure function and for both flux factors are shown in Fig.2.6 and Fig.2.7 respectively. Now we can write the formula for the diffractive DIS cross section:

$$x_{\mathbf{P}} \frac{d\sigma_D(\gamma^* \rightarrow q\bar{q})}{dt dx_{\mathbf{P}}} \Big|_{t=0} = \frac{\sigma_{tot}(pp)}{16\pi} \frac{4\pi^2\alpha_{em}}{Q^2} [\phi_{\mathbf{P}}(x_{\mathbf{P}})F_{val}^{\mathbf{P}}(\beta, Q^2) + f_{\mathbf{P}}(x_{\mathbf{P}})F_{sea}^{\mathbf{P}}(\beta, Q^2)] \quad (2.50)$$

The authors focused on the forward diffraction dissociation,  $t=0$ . However, the  $t$ -dependence of the flux factors in the model is definite and different for valence and sea parts:  $\phi_{\mathbf{P}}(x_{\mathbf{P}}) \exp(-B_{el}|t|)$  and  $f_{\mathbf{P}}(x_{\mathbf{P}}) \exp(-B_{3\mathbf{P}}|t|)$ , where  $B_{el}(\approx 12 \text{ GeV}^{-2})$  is the diffraction slope of elastic scattering, whereas  $B_{3\mathbf{P}}(\approx 6 \text{ GeV}^{-2})$  is the slope connected with triple-pomeron regime. This leads to a  $t$ -dependent factorization breaking. The  $t$ -integrated mass spectrum equals:

$$x_{\mathbf{P}} \frac{d\sigma_D}{dt dx_{\mathbf{P}}} = \frac{\sigma_{tot}(pp)}{16\pi B_{3\mathbf{P}}} \frac{4\pi^2\alpha_{em}}{Q^2} \left[ \frac{B_{3\mathbf{P}}}{B_{el}} \phi_{\mathbf{P}}(x_{\mathbf{P}})F_{val}^{\mathbf{P}}(\beta, Q^2) + f_{\mathbf{P}}(x_{\mathbf{P}})F_{sea}^{\mathbf{P}}(\beta, Q^2) \right] \quad (2.51)$$

where  $\sigma_{tot}(pp)/16\pi \approx 1.8 \text{ GeV}^{-2}$ .

The diffractive proton structure function, integrated over  $t$ , predicted by the model reads:

$$F_2^{diff}(x_{\mathbf{P}}, \beta, Q^2) = \frac{\sigma_{tot}(pp)}{16\pi} \frac{1}{x_{\mathbf{P}}} \Phi_D(x_{\mathbf{P}}, \beta, Q^2) \quad (2.52)$$

where

$$\Phi_D(x_{\mathbf{P}}, \beta, Q^2) = \frac{1}{B_{el}} \phi_{\mathbf{P}}(x_{\mathbf{P}})F_{val}^{\mathbf{P}}(\beta, Q^2) + \frac{1}{B_{3\mathbf{P}}} f_{\mathbf{P}}(x_{\mathbf{P}})F_{sea}^{\mathbf{P}}(\beta, Q^2) \quad (2.53)$$

and  $\sigma_{tot}(pp) = 40 \text{ mb}$ .

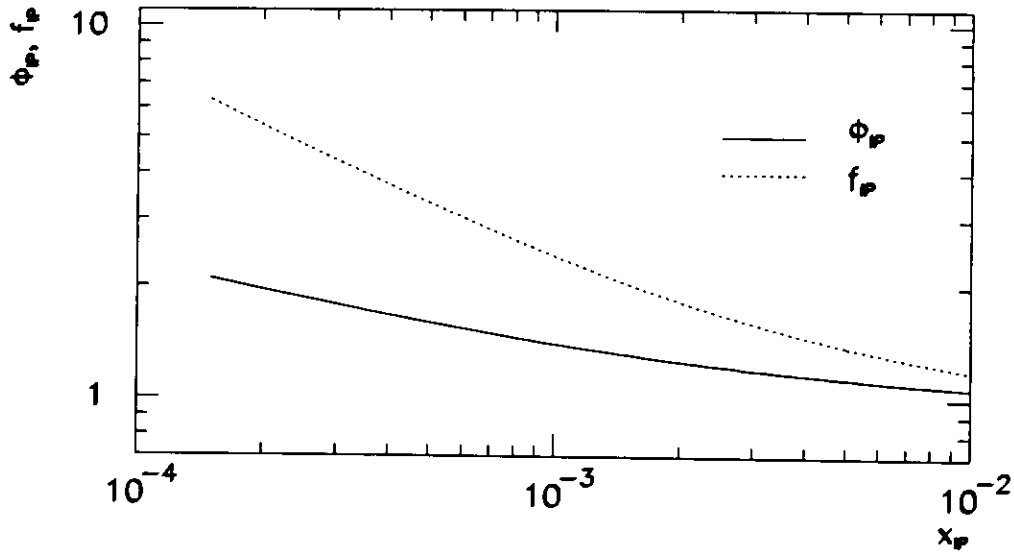


Figure 2.6: Predictions of the Nikolaev-Zakharov model for flux functions  $\phi_P(x_P)$  (solid curve) and  $f_P(x_P)$  (dashed curve).

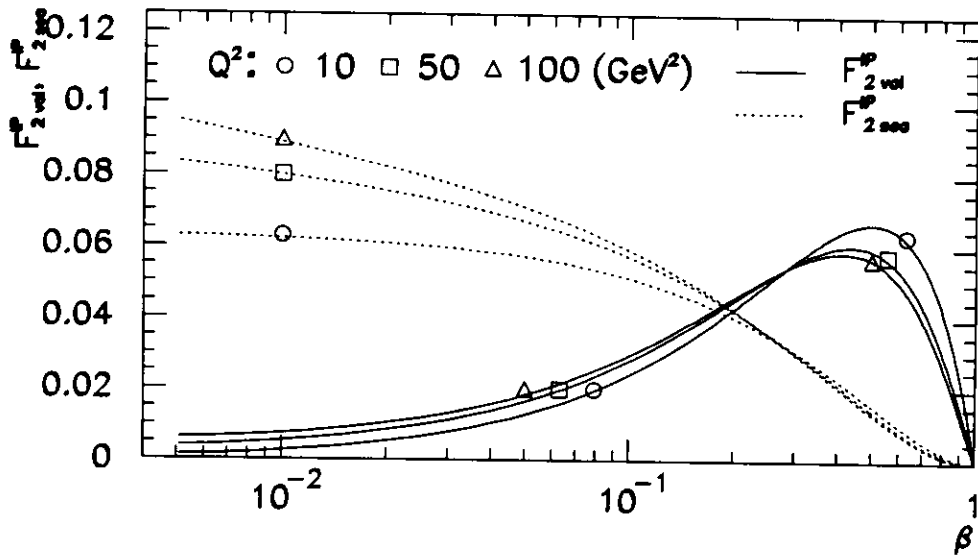


Figure 2.7: Predictions of the Nikolaev-Zakharov model for the  $\beta$  and  $Q^2$  dependencies of the components  $F_{val}^P(\beta, Q^2)$  (solid curves) and  $F_{sea}^P(\beta, Q^2)$  (dashed curves) of the pomeron structure function.

## 3 ZEUS – a detector at HERA

### 3.1 The HERA accelerator

HERA is the first electron–proton collider in the world. It is situated at the DESY laboratory in Hamburg, Germany. The project was authorized in April 1984 and began operation for two installed experiments, H1 and ZEUS, in the summer of 1992. HERA was built by an international collaboration from Canada, China, CSFR, France, Germany, Israel, Italy, Netherlands, Poland, United Kingdom and the USA.

The electron and proton beams are guided in two separate rings which cross each other in three experimental halls, two of which are occupied by H1 and ZEUS, and the third hall has been allocated for HERMES. The layout of the HERA collider is presented in Fig.3.1. The protons are accelerated up to an energy of 820 GeV with the use of superconducting magnets. The electron ring uses conventional magnets and store 30 GeV electrons. During the running period of 1992–1993 the energy of electrons was limited to 26.7 GeV.

The proton injection system begins with the Proton Linac, where  $H^-$  ions are accelerated up to 50 MeV. Then they are accelerated up to 7.5 GeV in the DESY III synchrotron. After stripping off, the hydrogen ions are accelerated to 40 GeV in PETRA II and then they are injected to HERA where the nominal energy is achieved.

Electrons are first accelerated to 500 MeV in the LINAC II and then up to 7.5 GeV in the DESY II synchrotron. Then electrons are transferred to the PETRA II storage ring, where their energy is increased to 12 GeV. Both, electron and proton bunches spacing in PETRA is the same as in HERA. The last step of the accelerating of the electrons take place in HERA, where they achieve their final energy.

Some of the design values of HERA parameters are shown in Table 3.1. For the 1993 data taking, 84 paired bunches were filled for each beam and in addition 10 electron and 6 proton bunches were left unpaired for background studies. The electron and proton beam currents were typically 10 mA. The proton ring RF frequency was 208 MHz which resulted in a root mean square proton bunch length of about  $\pm 20$  cm.

### 3.2 The ZEUS detector

The main components of the central ZEUS detector are shown in Fig.3.2. In the ZEUS coordinate system, the initial protons move in the positive  $z$  direction. The origin of the ZEUS coordinate system is defined at the nominal interaction point. The  $x$  coordinate points towards the center of the HERA ring, and the  $y$  coordinate points upwards. The ZEUS detector was designed to fulfill strong requirements on calorimetry, tracking and particle identification. Due to large momentum imbalance between the incident electrons and protons, most particles are produced close to the proton beam direction.

In the following only the components used in this analysis are described in detail. A full description of the ZEUS detector can be found in [32].

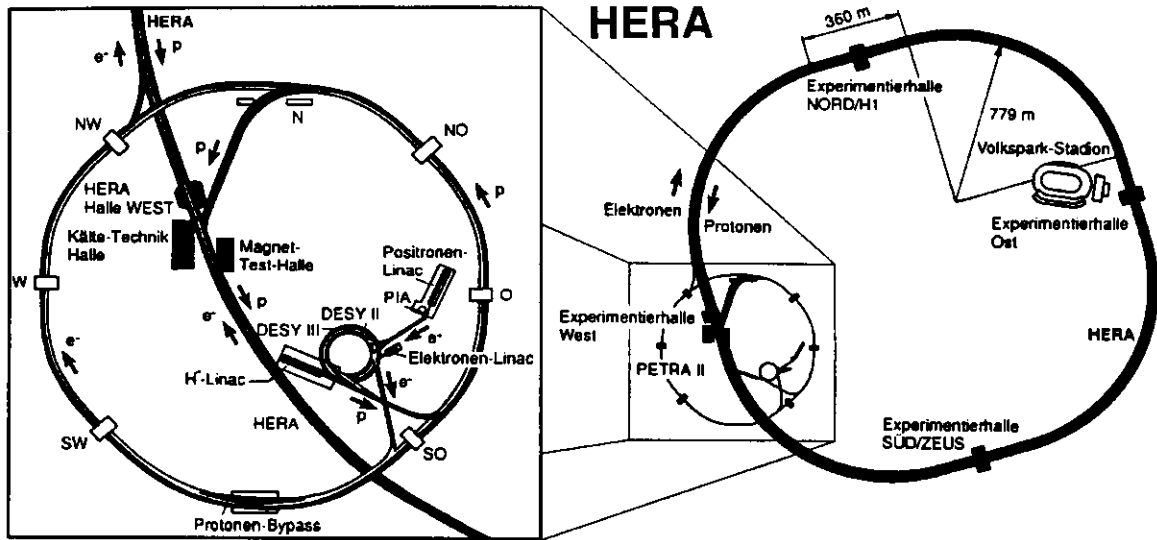


Figure 3.1: Layout of HERA accelerator with the zoom on the injection scheme.

HERA parameters	electron	proton
Nominal Energy (GeV)	30	820
C.M. Energy (GeV)	314	
Maximum $Q^2$ (GeV <sup>2</sup> )	$9 \times 10^4$	
Luminosity (cm <sup>-2</sup> s <sup>-1</sup> )	$1.5 \times 10^{31}$	
Circumference (m)	6336	
Magnetic Field (T)	0.165	4.65
Injection Energy (GeV)	14	40
Filling Time (min)	15	20
Circulating Current (mA)	58	163
Number of Bunches	210	
Time between Crossings (ns)	96	
Horizontal Beam Size $\sigma_x$ (mm)	0.26	0.29
Vertical Beam Size $\sigma_y$ (mm)	0.07	0.07
Longitudinal Beam Size $\sigma_z$ (cm)	0.8	11

Table 3.1: Design values of the main HERA parameters.

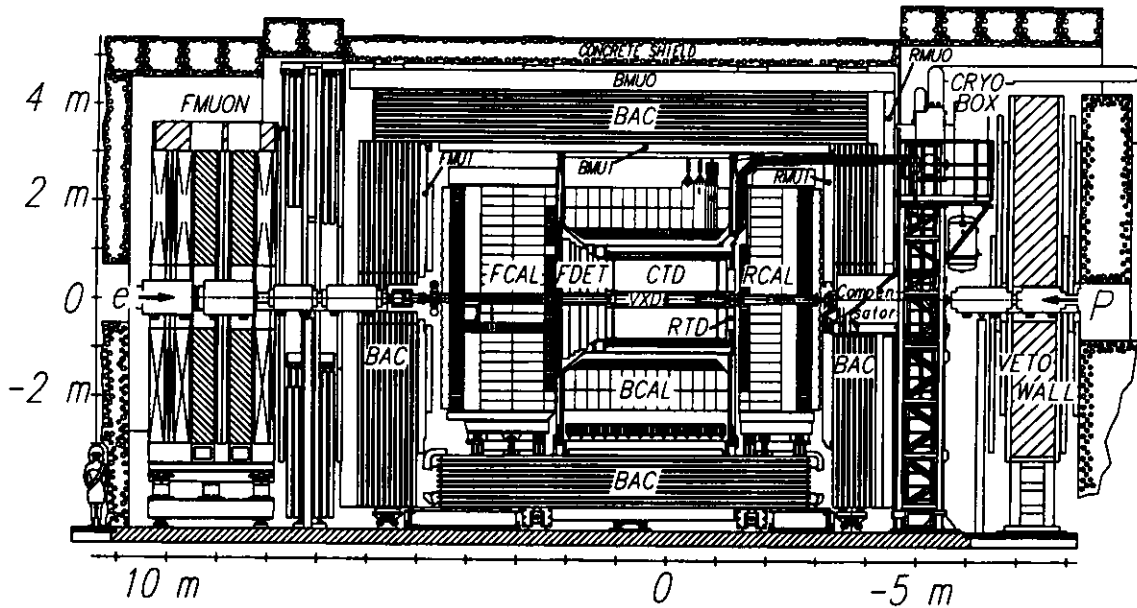


Figure 3.2: Schematic view of the ZEUS detector.

### 3.2.1 Central tracking system

The central tracking system consists of the vertex detector (VXD), the central tracking detector (CTD), the forward and rear tracking detectors (FTD and RTD) and the magnet coil (MAGNET). This system allows for a precise determination of the primary and secondary vertices, a good transverse momentum resolution and a reconstruction of tracks and momenta of charged particles.

The main tasks of the VXD are the measurement of the event vertex, the detection of short lived particles by reconstructing secondary vertices, and the improvement of the momentum and angular resolution of charged particles. It is a cylindrical drift chamber with wires running parallelly to the beam. A spatial resolution of  $50 \mu\text{m}$  has been achieved in the central region of the cell and  $150 \mu\text{m}$  near the edges. The CTD is used to reconstruct the direction and momentum of charged particles in the polar angle region of  $15^\circ < \theta < 164^\circ$  surrounding the interaction region. It is also used to measure the energy loss  $dE/dx$  that is used for particle identification. The CTD is a cylindrical drift chamber consisting of 4608 sense wires. The chamber is divided into nine superlayers. Each superlayer is further divided into cells containing eight sense wires. Five superlayers have wires parallel to the beam line, and four are stereo layers which have wires with a small angle with respect to the beam line. The arrangement of wires in one octant of the CTD is schematically shown in Fig.3.3. The position resolution in the  $z$  direction is between  $1.0$  and  $1.4 \mu\text{m}$ . The design hit resolution in the  $r - \phi$  plane is  $100\text{--}120 \mu\text{m}$ . For charged particles that traverse all nine superlayers, the design momentum resolution is  $\sigma(p)/p = (0.005)p \oplus 0.016$  (for  $p_T$  in GeV). Forward and rear tracking detectors enable measurement of tracks in

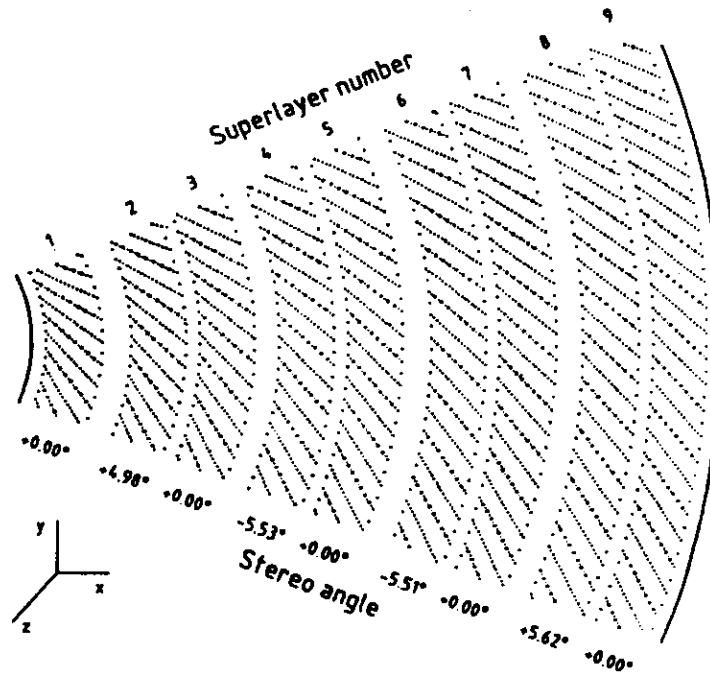


Figure 3.3: *Layout of an octant of the CTD. Sense wires are indicated by larger dots. The superlayer numbering convention and stereo angle of wires within the superlayer is also shown.*

the very forward and rear directions. The FTD consists of three planar drift chambers. It provides tracking with a polar angle coverage of  $7.5^\circ < \theta < 28^\circ$ . The RTD in the rear direction consists of a single drift chamber. It covers the polar region  $160^\circ < \theta < 170^\circ$ . Each chamber in the FTD and RTD consists of three layers of drift cells perpendicular to the beam line with fixed wires whose orientations are  $0^\circ$ ,  $+60^\circ$ ,  $-60^\circ$ . A superconducting solenoid (MAGNET) is positioned around the CTD in a 2.8 m long cryostat. It supplies the magnetic field 1.43 T that bends charged particles in the  $r - \phi$  plane and hence allows for a momentum measurement. The influence of the magnetic field on the beams is compensated by a special superconducting magnet (Compensator) installed behind the rear calorimeter.

### 3.2.2 Calorimeter

Good calorimetry was one of the strong requirements for the ZEUS detector. It is essential for precise measurements of particles energies and positions. An ideal calorimeter should be able to stop all incoming particles. But in real life the energy of a particle is measured through conversion of fraction of the initial energy into a visible signal. Incident particle

interacts with a dead material of the calorimeter producing secondary particles. This is the so called showering process. Calorimeters can measure energies of both charged and neutral particles. We distinguish electromagnetic and hadronic showers, and the difference between them is used to identify the scattered electron.

Electromagnetic showers are produced by incident high energy electrons and photons due to combined phenomena of bremsstrahlung and pair production. An electron radiates photons, which converts to pairs, which radiate and produce fresh pairs in turn. This process continues until the mean energy per particle equals to the definite energy  $E_c$ , when the energy loss by ionisation becomes important and no further radiation is possible. The shower will reach a maximum and then cease abruptly. The maximum will occur at:

$$t_{max} = \frac{\ln E_0/E_c}{\ln 2} \quad (3.1)$$

where  $t$  is measured in radiation lengths  $X_0$ , and  $E_0$  is the energy of the incident particle. The number of the particles at the maximum is:

$$N_{max} = \exp [t_{max} \ln 2] = \frac{E_0}{E_c} \quad (3.2)$$

In practice the development of a shower consists of an initial exponential rise, a broad maximum and a gradual decline. However, the above equations indicate the main qualitative features of an electromagnetic shower:

- (a) the maximum occurs at a depth increasing logarithmically with the primary energy  $E_0$ ,
- (b) the number of shower particles at the maximum is proportional to  $E_0$ ,
- (c) a total track-length integral is proportional to  $E_0$ .

The transverse size of the electromagnetic shower is determined by the Coulomb scattering. In all materials, this spread is of the order of one Moliere unit:

$$R_m = 21 \frac{X_0}{E_c} \quad (3.3)$$

with  $E_c$  in Mev. The effective  $R_m$  of the electromagnetic parts of the ZEUS calorimeter is 2 cm.

The physical processes that cause the propagation of a hadronic shower are considerably different from the processes in the electromagnetic shower. In conventional calorimeters a large fraction of hadronic energy is dissipated by the excitation or breakup of nuclei of the absorber material and remains undetected. The ratio of visible energy to the total energy is called sampling fraction and depends on the type of particle traversing the calorimeter. The sampling fraction is different for electrons and hadrons. A hadron

calorimeter is characterized by the ratio of the electron to the hadron response,  $e/h$ , which for an ideal calorimeter should approach one. The calorimeter which fulfill this requirement is called compensated. Otherwise the response of the calorimeter starts to be nonlinear with energy, because the number of produced  $\pi_0$ 's increases with increasing energy. Up to now equal response to the electrons and hadrons has been achieved only in calorimeters made from depleted uranium and scintillator. The energy in hadronic showers is deposited through the following processes:

- (a) electromagnetic cascades, which are the result of the decay of neutral hadrons ( $\pi_0$ ) into photons,
- (b) ionisation by charged hadrons that produce an energy loss described by the Bethe-Bloch equation:

$$-\frac{dE}{dx} = 0.307 \frac{Z}{A} \frac{1}{\beta^2} \left[ \ln \left( \frac{2m_e c^2 \gamma^2 \beta^2}{I} \right) - \beta^2 - \frac{\delta}{2} \right] \quad (3.4)$$

where  $I$  is the ionisation constant of the material.

- (c) the hadron nucleus scattering which leads to nuclear breakup and fission; this process results in energy dissipation,
- (d) in material with very high  $Z$  ( $^{238}\text{U}$ ), hadronic showers produce a significant number of neutrons with energies in the MeV range. These neutrons are moderated in energy by elastic collisions with hydrogen in the scintillator. The kinetic energy of the neutrons is converted into measurable proton-recoil energy. This boosts the hadron response considerably.
- (e) at very low neutrons energies the neutron capture process dominates which yields delayed gamma radiation and hence the delayed boost of the signal.

The ZEUS calorimeter is divided into three parts: FCAL which covers the azimuthal region  $2.2^\circ < \theta < 39.9^\circ$ , BCAL covering  $36.1^\circ < \theta < 129.1^\circ$  and RCAL covering  $128.1^\circ < \theta < 176.5^\circ$ . Each part consists of modules which are further divided into  $20 \times 20 \text{ cm}^2$  towers. Each tower is longitudinally divided into an electromagnetic (EMC) and hadronic (HAC) sections. FCAL and BCAL have two hadronic sections while the RCAL has only one. A tower in FCAL and BCAL consists of four  $5 \times 20 \text{ cm}^2$  EMC cells and two  $20 \times 20 \text{ cm}^2$  hadronic cells (HAC1 and HAC2). A tower in the RCAL consists of two  $10 \times 10 \text{ cm}^2$  EMC cells and one  $20 \times 20 \text{ cm}^2$  HAC1 cells. Each cell is read out by two photomultipliers (PMT) to provide redundancy and more accurate position measurement within a cell. Each cell consists of alternating layers of 3.3 mm thick depleted uranium (DU) as the passive absorber and 2.6 mm plastic scintillator. as the active material. The depleted uranium is an alloy of 98.4%  $^{238}\text{U}$ , 1.4% Nb and less than 0.2%  $^{235}\text{U}$ . The DU plates are wrapped by thin sheet of stainless steel in order to reduce noise from the natural radioactivity. This

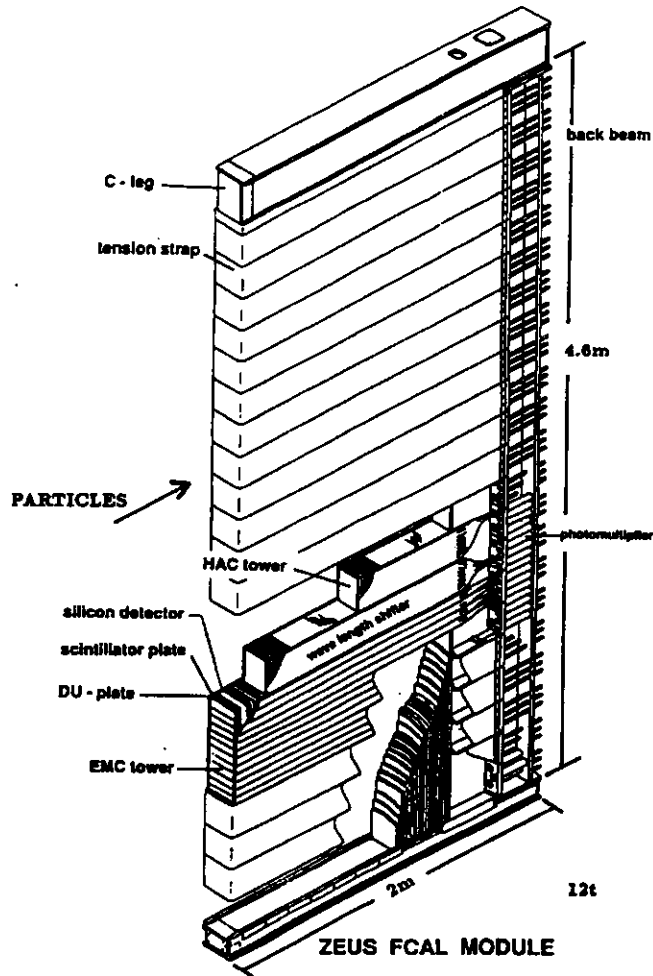


Figure 3.4: *Layout of the ZEUS FCAL module. The module is partitioned into towers of  $20 \times 20 \text{ cm}^2$  having three sections, an electromagnetic section EMC and two hadronic sections, HAC1 and HAC2.*

effectively lowers the  $e/h$  ratio, but on the other hand, neutrons produced in hadronic showers lose relatively more ionisation energy in the scintillator. The ratio of the thickness of absorber to the active material is chosen to achieve a full compensation and the best energy resolution.

Under test beam conditions the CAL has an energy resolution  $\sigma_E/E = 0.35/\sqrt{E(\text{GeV})}$  for hadrons and  $\sigma_E/E = 0.35/\sqrt{E(\text{GeV})}$  for electrons.

### 3.2.3 Other components

The veto wall and C5 counter advertise particles that enter the detector from the rear direction. The purpose of the veto wall is to veto upstream beam gas interactions and to shield the detector against particles from the proton beam halo. The veto wall is a large iron wall ( $8 \times 7.6 \times 0.87$  m) covered on both sides with scintillation counters. It is located at  $z = -748$  cm.

The C5 counter consists of two planes of scintillator separated with 5 cm of lead which surround the beam pipe at  $z = -315$  cm. Lead sheets in front and behind the scintillator suppress synchrotron radiation. The C5 counter provides accurate timing measurement for both electron and proton beams, which is useful for the rejection of the beam gas interactions.

Apart from the main ZEUS detector, there are the so called *small angle detectors* that measure particles emitted at very forward or backward directions, which escape undetected down the beam pipe.

The leading proton spectrometer (LPS) allows the measurement of forward scattered protons that have lost only a little of the longitudinal momentum ( $< 0.3p_{beam}$ ) and have small transverse momenta  $p_T < 1$  GeV.

The LPS was not fully instrumented in the 1993 running period and was not used in the analysis presented in this thesis. However, the LPS will be a very important tool in the further analysis of diffractive processes.

On the other side of the ZEUS detector one can find the luminosity monitor which allows for the measurement of small angle photons and electrons. It is described in the next paragraph.

## 3.3 Luminosity measurement in 1993

The luminosity,  $L$ , is defined by the formula:

$$N = L\sigma \quad (3.5)$$

where  $N$  is the event rate of the process which has a cross section  $\sigma$ . The determination of the luminosity in the ZEUS experiment is based on the measurement of the rate of Bethe-Heitler process  $ep \rightarrow e\gamma p$ . This process has both clear experimental signature and a large cross section.

Photons produced in the bremsstrahlung process and secondary electrons are measured in the luminosity monitor (LUMI). The layout of the luminosity monitor is shown in Fig.3.5. The LUMI is divided into two parts, the photon and electron branches, which measure the energy and position of the bremsstrahlung photon and electron, respectively.

The scattered electrons have energies lower than the beam energy and therefore are deflected by the magnet system from the nominal orbit. These electrons leave the vacuum

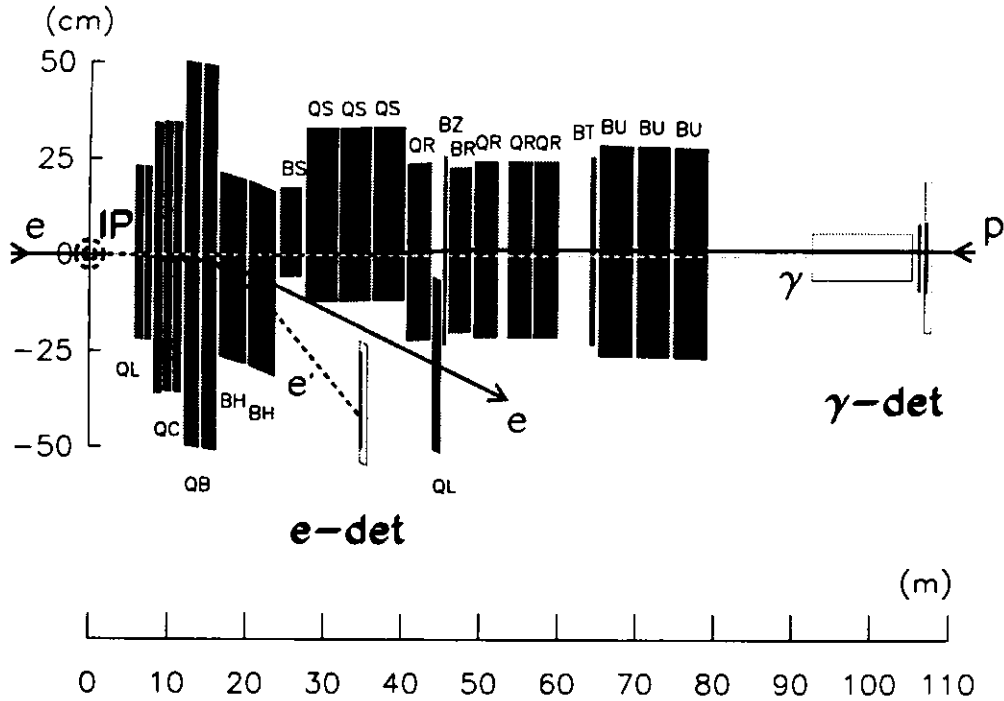


Figure 3.5: *Layout of the luminosity monitor detectors.*

pipe through a thin window located at  $z = -27$  m and are detected in the electromagnetic calorimeter (EDET) positioned at  $z = -36$  m. The bremsstrahlung photons are not deflected by the magnetic field and leave the beam pipe through an exit window located at  $z = -92$  m. They are measured in the photon calorimeter (GDET) installed at  $z = -108$  m.

Under test beam conditions both electromagnetic calorimeters had a resolution of  $\Delta E/E = 18.5\%/\sqrt{E(\text{GeV})}$ . Each calorimeter consists of alternate layers of lead as absorber and plastic scintillator as active material. The photon calorimeter has a depth of  $22X_0$  and the electron calorimeter has a depth of  $21X_0$ . In both calorimeters after  $7X_0$  the position detector is inserted. Each position detector consists of two layers of horizontal and vertical scintillator fingers. A carbon filter is placed in front of the photon calorimeter to reduce the flux of synchrotron radiation down to a negligible level.

The geometric acceptance of the photons is independent of the photon energy and is approximately 98%. In contrast, the electron acceptance is energy dependent and is over 70% in the range  $0.35E_e < E_e' < 0.65E_e$ .

Experimentally, the luminosity was calculated [33] from the rate of  $ep$  bremsstrahlung events  $R_{ep}$  and the luminosity definition formula:

$$L = \frac{R_{ep}}{\sigma_{obs}} \quad (3.6)$$

The observed cross section is determined by the convolution of the Bethe–Heitler cross section  $\sigma_{BH}$  and a probability  $A_{lumi}$  that a bremsstrahlung event will be identified as a luminosity event:

$$\sigma_{obs} = \int A_{lumi} d\sigma_{BH} \quad (3.7)$$

The integration runs over the whole relevant range of photon four-momenta. The bremsstrahlung of beam electrons on the rest gas has the same signature as the  $ep$  bremsstrahlung, but an even larger cross section. It therefore represents a significant background and has to be subtracted statistically using the electron pilot bunches. Thus the 'true' rate of the  $ep$  bremsstrahlung reads:

$$R_{ep} = R_{tot} - kR_{pilot} \quad (3.8)$$

where  $R_{tot}$  is the total rate of bremsstrahlung events,  $R_{pilot}$  is the rate measured from the electron pilot bunches and  $k$  is the ratio of the total electron current to that in the pilot bunches.

For luminosity determination photons with energy greater than 5 GeV were used. However, for systematic checks this cut value is changed. The main sources of systematic error in the luminosity measurement are:

- uncertainty in  $egas$  background subtraction (estimated error is 0.5%),
- counting errors due to wrong flagging of the 'luminosity events' (estimated errors are below 0.3%),
- correction for multiple events is less than 0.2%,
- uncertainty of the theoretical cross section (about 1%),
- acceptance error of the photon calorimeter (from MC studies an error of 0.5% is expected),
- a 1% uncertainty of the photon calorimeter calibration was established.

Since all contribution are independent, therefore errors can be summed up in quadrature resulting in a 2.5% total systematic error of the luminosity measurement. The integrated luminosity delivered by HERA and used in this analysis are shown in Fig.3.6.

### 3.4 The ZEUS trigger and the data acquisition system in 1993

At HERA, bunch crossings occur every 96 ns. This time is too short to allow components to read out data and issue a trigger decision. Most of the triggers come from collisions between the proton beam and the residual gas in the beam pipe. The selection of interesting events among many background events is performed in three level trigger system,

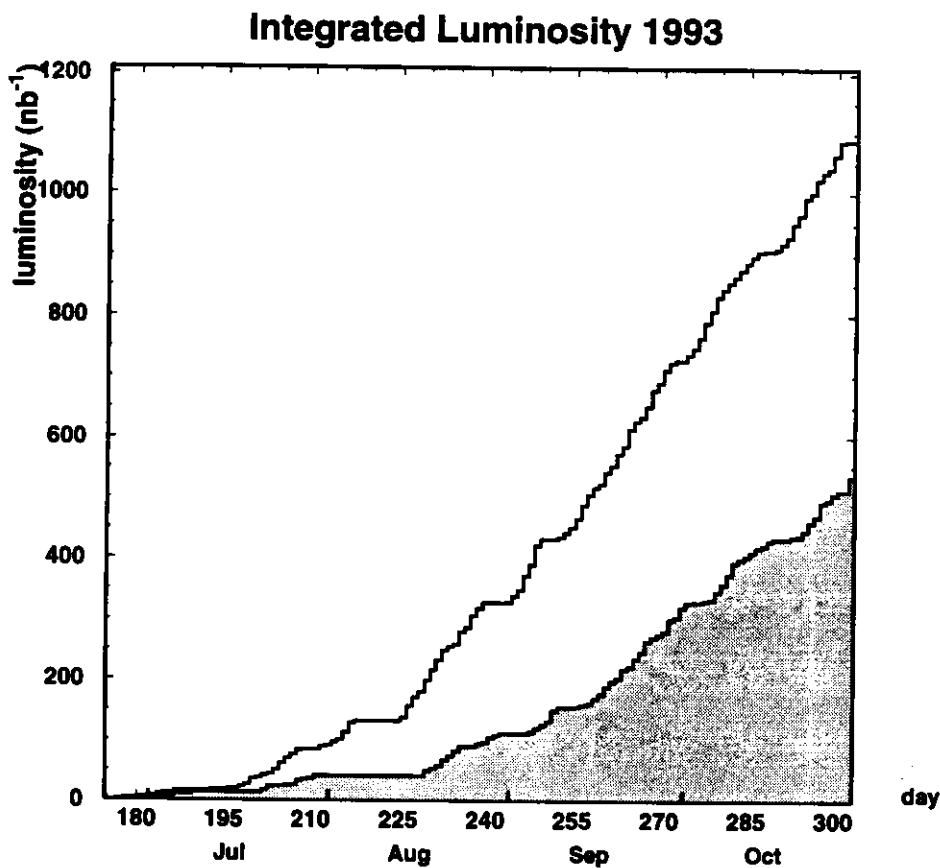


Figure 3.6: *Luminosity delivered by HERA and accumulated by ZEUS experiment in 1993 running period.*

which reduces the rate from about 50k Hz down to few Hz. The schematic view of the ZEUS trigger and the data acquisition system is shown in Fig.3.7.

The first level trigger (FLT) [34] is designed to reduce the event rate to 1k Hz. For every bunch crossing, the data from the components are stored in pipeline buffers for 5  $\mu$ s while the FLT calculations are performed. Each component can have its own local FLT. The decisions from the local FLT are passed to the global FLT (GFLT) which makes a final decision. The FLT for DIS events required a logical .OR. of three conditions on sums of energy in the EMC calorimeter cells:

- either the BCAL EMC energy exceeded 3.4 GeV
- or the RCAL EMC energy, excluding the towers immediately adjacent to the beam pipe, exceeded 2.0 GeV
- or RCAL EMC energy, including the beam pipe towers, exceeded 3.75 GeV.

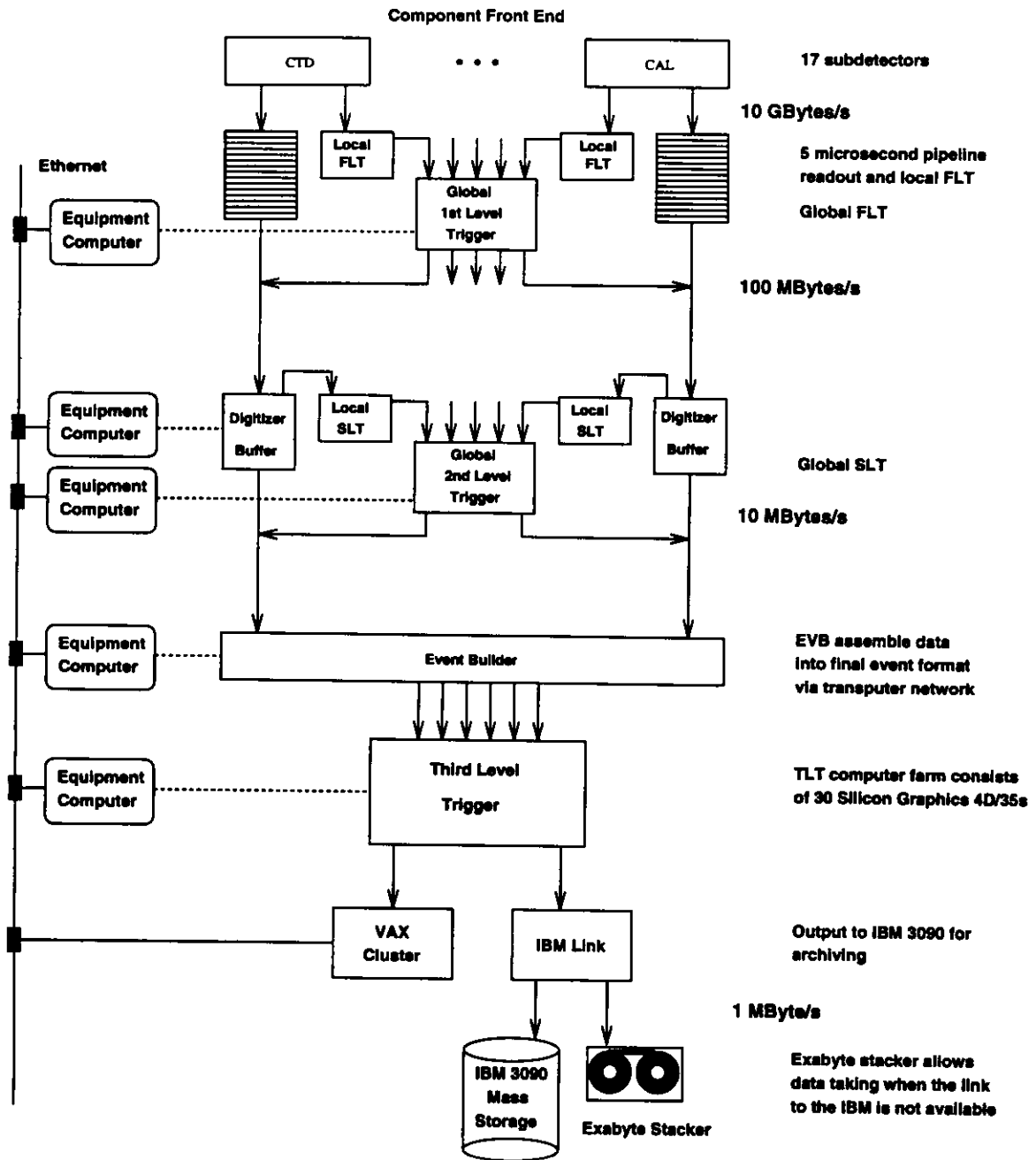


Figure 3.7: Overview of the ZEUS trigger and data acquisition system [95].

Additionally, an alternative high transverse energy trigger included DIS events with an electron in the FCAL. The FLT acceptance rises from about 95% at  $Q^2 = 5 \text{ GeV}^2$  to a value close to 100% for  $Q^2$  above  $10 \text{ GeV}^2$ . It was found from a study of independent triggers that the inefficiency due to bad channels and calibration errors is less than 1%. The events accepted by GFLT are passed to the second level trigger (SLT). While the FLT is a hardware trigger, the SLT is a software-based one and runs on a network of transputers. The SLT has access to a large fraction of data and has more time to make a decision. The SLT rejects proton beam-gas events using the event times measured in the calorimeter. It sets an output rate to about 100 Hz, but without loss of DIS events. After a positive decision of the SLT, the digitized data from all components are collected by the ZEUS event builder (EB) and sent to the third level trigger (TLT). The TLT is a software-based trigger which performs calculations on a farm of Silicon Graphics (SGI) workstations. It is designed to reduce the rate to few Hz. The output rate is limited by the rate at which data can be written on tapes. The TLT applies stricter cuts on the event timings and also rejects beam-halo muons and cosmic muons. Events remaining after these cuts are then selected by individual physics filters. In 1993 there were three different filters for DIS [36]:

1. *Normal neutral current* is meant to be an event with a  $Q^2$  value that is not very high, so that the electron is either in the RCAL or in the BCAL. In this case the FLT bits for the electromagnetic part of the BCAL or the RCAL should be set. In addition the following cuts were applied:
  - $\sum E - p_z + 2E_\gamma > 20 \text{ GeV}$ , where the sum runs over all calorimeter cells, and  $E_\gamma$  is energy measured in photon calorimeter of the luminosity monitor.
  - $\sum E - p_z < 100 \text{ GeV}$ . In this case  $E_\gamma$  is not included to avoid the loss of deep inelastic events which overlay with bremsstrahlung events.
2. *Very high  $Q^2$  neutral current* in which an electron enters BCAL or FCAL. In the latter case the FLT bits could not be set. Since in these events the transverse energy is very high, it was found that the cut  $E_T > 40 \text{ GeV}$ , where  $E_T$  is calculated from the calorimeter energy deposits, has an efficiency 100%. In addition ' $E - p_z$ ' cuts described above are applied.
3. *Charged current* events are characterized by a high measured missing transverse momentum  $P_T$  due to the outgoing neutrino. The following cuts are applied:
  - $P_T > 9 \text{ GeV}$
  - *and* (Number of tracks  $\geq 1$  *or*  $E_{FCAL} > 10 \text{ GeV}$ )
  - *and*  $E_{RCAL} < 70 \text{ GeV}$

The TLT result for each event can be read from the first three bits (0-2) of the ADAMO [44] word TLTEVT\_Subtrg(4).

## 4 Reconstruction of kinematics at HERA

An accurate reconstruction of kinematic quantities ( $x$ ,  $y$ ,  $Q^2$ ,  $x_F$ ,  $\beta$ ) is crucial for structure functions measurements at HERA. In this section, we present various reconstruction methods of the kinematical variables for inclusive, diffractive NC DIS. We compare smearings of the kinematical variables and select the best method which we use in following analysis. The determination of kinematical variables was extensively studied in [37].

### 4.1 Reconstruction methods

The quantities one measures in the experiment are the angles and energies of the final state electron and hadrons. In DIS the hadron flow is directly related to the kinematics of the struck quark. In the following we use the notation:

$E$	-	Energy of the initial electron
$E'$	-	Energy of the final electron
$\theta$	-	Polar angle of the final electron
$E_p$	-	Energy of the initial proton
$E_q$	-	Energy of the struck quark
$\gamma$	-	Polar angle of the struck quark

Using only the scattered electron energy  $E'$  and the scattered angle  $\theta$  we have:

$$y_{elec} = 1 - \frac{E'}{2E}(1 - \cos \theta) \quad (4.1)$$

$$Q_{elec}^2 = 2EE'(1 + \cos \theta) \quad (4.2)$$

$$x_{elec} = \frac{E}{E_p} \frac{E'(1 + \cos \theta)}{2E - E'(1 - \cos \theta)} \quad (4.3)$$

The electron energy scale at ZEUS is understood only at a few percent level due to a not exact knowledge of the dead material between the beam pipe and the calorimeter. Recently a method was proposed to correct the energy of the scattered electron [38].

The Jacquet-Blondel method [39] reconstructs kinematics of the  $ep$  DIS using the hadronic vertex ( $E_q$ ,  $\gamma$ ). From that method we obtain:

$$y_{JB} = \frac{\sum_i (E_i - p_{zi})}{2E} \quad (4.4)$$

$$Q_{JB}^2 = \frac{(\sum_i p_{xi})^2 + (\sum_i p_{yi})^2}{1 - y_{JB}} \quad (4.5)$$

$$x_{JB} = \frac{Q_{JB}^2}{s y_{JB}} \quad (4.6)$$

where the sum runs over all observed final state hadrons. The energy of hadrons is obtained from the energy of the calorimeter cells, and the polar angle of the cell is determined using the cell center at the face of the calorimeter and the event vertex.

The (*mixed*) method combines the electron and hadronic methods. The following equations relate the kinematical variables in terms of the measured quantities:

$$y_{mix} = y_{JB} \quad (4.7)$$

$$Q_{mix}^2 = Q_{elec}^2 \quad (4.8)$$

$$x_{mix} = \frac{Q_{elec}^2}{s y_{JB}} \quad (4.9)$$

In the *double angle* method the polar angles of the electron and of the struck quark are used. The current jet angle  $\gamma$  can be obtained by inverting the Jacquet–Blondel variables:

$$\cos \gamma = \frac{Q_{JB}^2(1 - y_{JB}) - 4E^2 y_{JB}^2}{Q_{JB}^2(1 - y_{JB}) + 4E^2 y_{JB}^2} \quad (4.10)$$

Neglecting the vector sum  $\vec{P}_T$  of the spectator jet and the jet mass one can show that the above formula determines the angle  $\gamma$  which is just the energy weighted average of the cosines of the particles in the current jet. Using a calorimeter to measure the energy we obtain:

$$\cos \gamma = \frac{\sum_c E_i \cos \gamma_i}{\sum_c E_i} \quad (4.11)$$

where the sum runs over all calorimeter cells not assigned to the scattered electron. Kinematic variables can then be determined from the following equations:

$$y_{DA} = \frac{\sin \theta(1 - \cos \gamma)}{\sin \gamma + \sin \theta - \sin(\theta + \gamma)} \quad (4.12)$$

$$Q_{DA}^2 = 4E^2 \frac{\sin \gamma(1 + \cos \theta)}{\sin \gamma + \sin \theta - \sin(\theta + \gamma)} \quad (4.13)$$

$$x_{DA} = \frac{E \sin \gamma + \sin \theta + \sin(\theta + \gamma)}{E_p \sin \gamma + \sin \theta - \sin(\theta + \gamma)} \quad (4.14)$$

This method is not sensitive to energy fluctuations of the hadronic system.

The kinematic variables which characterize diffractive scattering for different reconstruction methods can be determined from the equations:

$$\beta_{meth} = \frac{Q_{meth}^2}{Q_{meth}^2 + m_X^2}_{meth} \quad (4.15)$$

$$x_{P\ meth} = \frac{x_{meth}}{\beta_{meth}} \quad (4.16)$$

where subscript *meth* indicate any particular reconstruction method. For all methods but the *double angle* method, the invariant mass of the hadronic system (without the diffractively scattered proton) is calculated from the energies and angles of the calorimeter cells using the event vertex. The mass  $m_{X\ DA}$  is obtained from the equation:

$$m_{X\ DA} = \sqrt{E_h^2 - p_h^2} \quad (4.17)$$

where:

$$E_h = p_h \cos \gamma + 2E y_{DA} \quad (4.18)$$

$$p_h^2 = \frac{Q_{DA}^2(1 - y_{DA})}{\sin^2 \gamma} \quad (4.19)$$

The scattered electron energy determined from *double angle* method reads:

$$E'_{DA} = \frac{2E \sin \gamma}{\sin \gamma + \sin \theta - \sin(\theta + \gamma)} \quad (4.20)$$

## 4.2 Smearing of kinematic variables

A sample of MC events (*EPDIFFR*, see next section) was used to study the smearings for different reconstruction methods. In Fig.4.1 the smearing is shown from the true values for reconstruction using the *double angle*, *electron*, *JB*, *mixed* methods. The plots show the reconstructed value versus the MC generated value. The same plots after applying the final selection cuts (see Section 7) are shown in Fig.4.2. One can see that the cuts select the subsample for which the kinematical variables are measured much more better than before.

The reconstruction of  $\beta$  and  $x_P$  is affected by the poor determination of the mass  $m_X$ . The measurement of  $m_X$  is influenced by the energy and particle loss due to the dead material in the detector, which is not well simulated in Monte Carlo. Approximately 50% more hadronic energy is lost in the data than in MC simulation [40]. Also the calorimeter noise affects the reconstruction of low masses. The noise results in low energy isolated cells randomly distributed over the whole calorimeter. In this analysis isolated cells with energies less than 160 MeV for EMC cells and less than 180 MeV for HAC cells were removed [41].

The resolution in the measurement of the mass  $m_X$  was simulated in Monte Carlo. Results are shown in Fig.4.3 for two cases: a) the mass is calculated directly from calorimeter cells; b) the mass is calculated from the *double angle* method. In the first case the resolution is below 20% but the systematic shift is of the order of 20-30%. In the second case the resolution changes smoothly from 20% for low masses to 50% for high masses, but the systematic shift is not so dramatic as previously, thus is still observed. For a better measurement of the mass  $m_X$  we have scaled the mass spectrum by a factor of 1.15 to

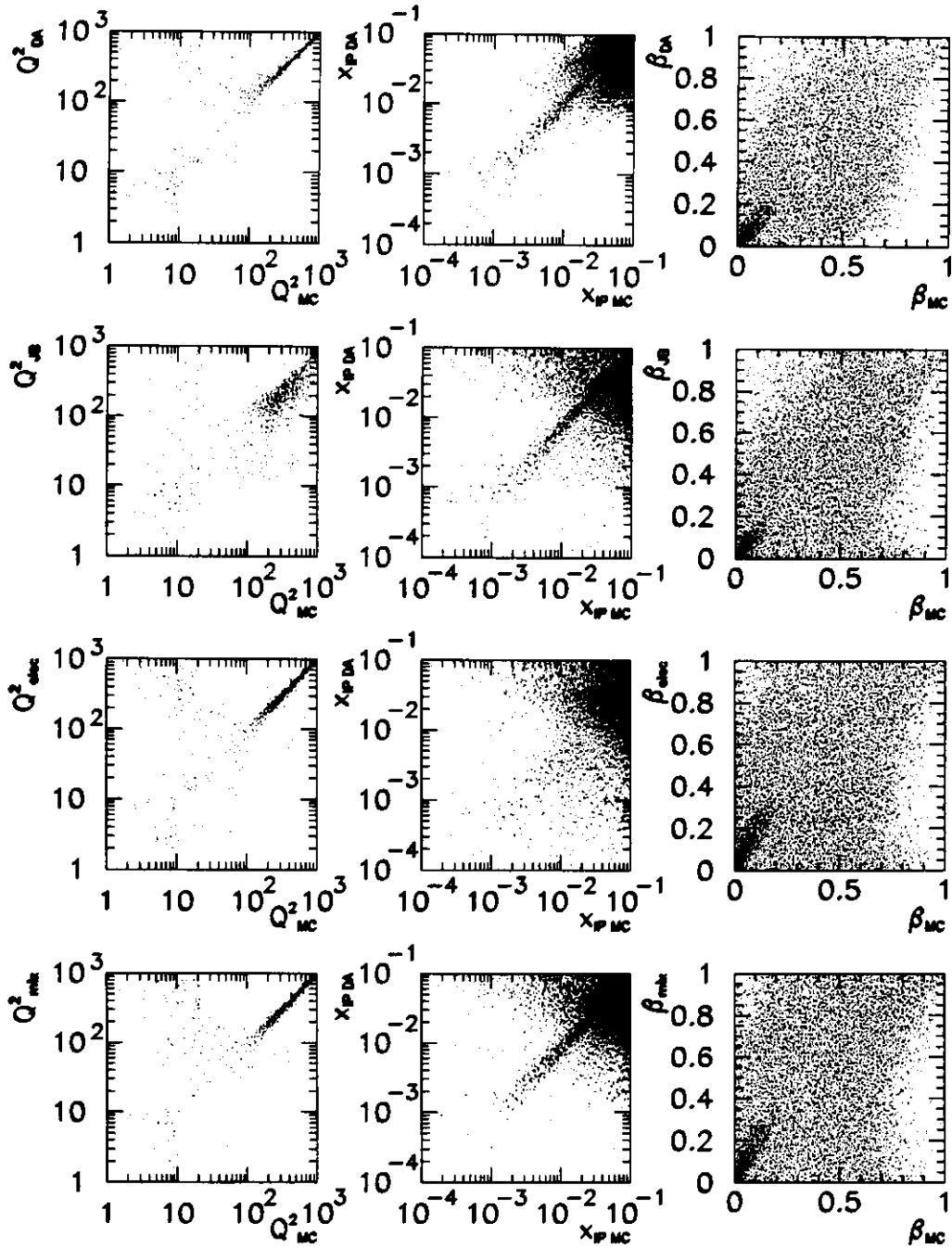


Figure 4.1: *Smearing of the kinematical variables for different reconstruction methods. No cuts applied.*

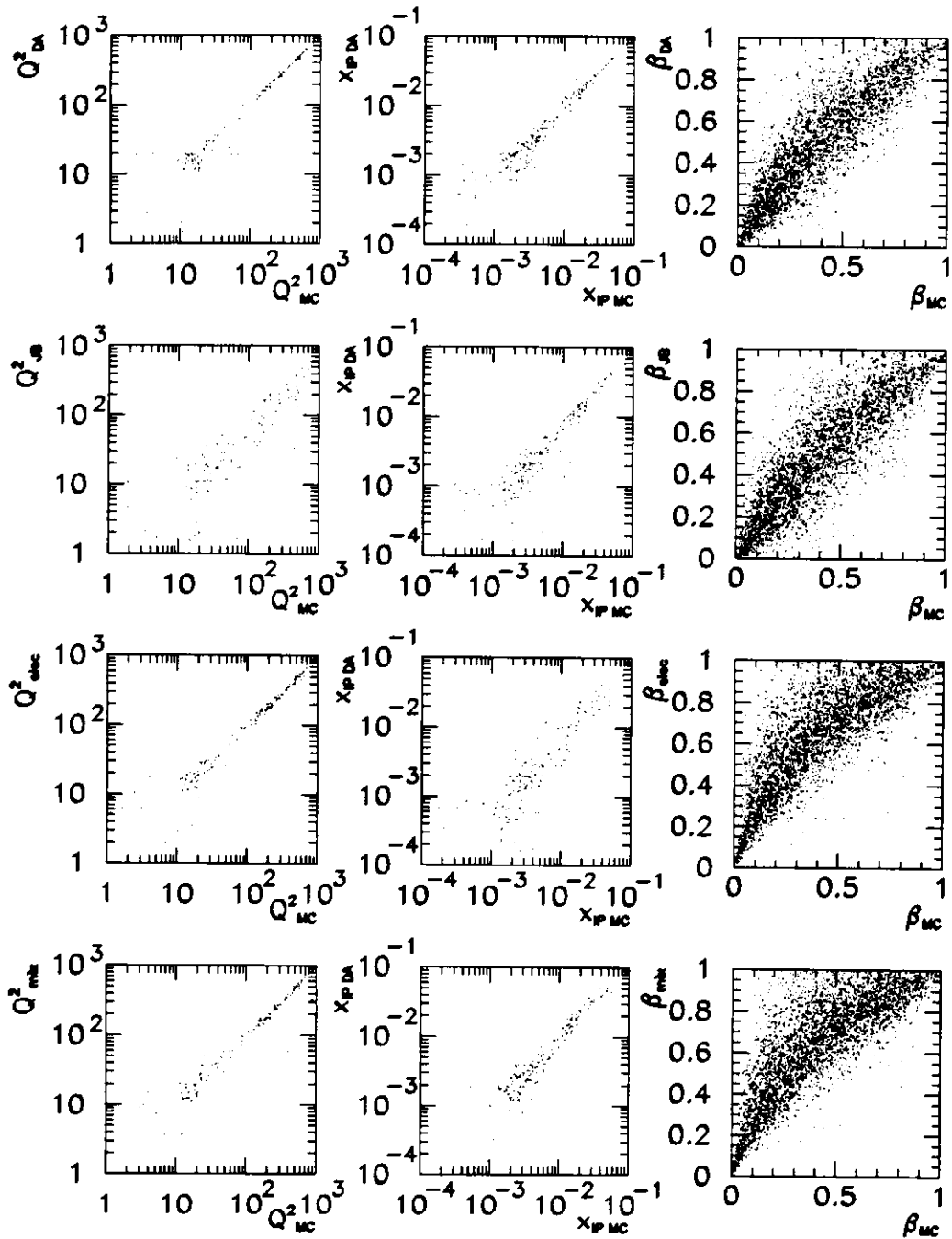


Figure 4.2: Smearing of the kinematical variables for different reconstruction methods. The final selection cuts are applied.

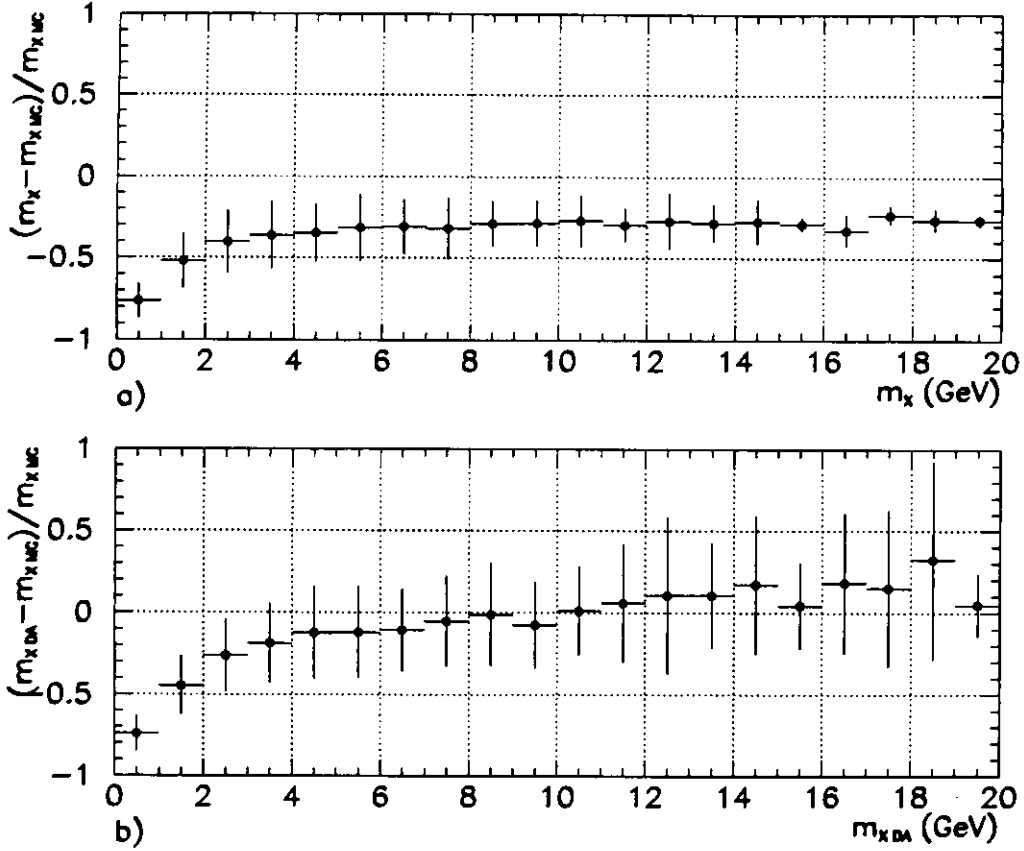


Figure 4.3: *Fractional difference between the reconstructed and generated value of  $m_x$  as a function of the reconstructed value. The horizontal lines give the systematic shift and the error bars give the resolution of the measurement. a) mass is calculated directly from calorimeter cells, b) mass is calculated from double angle method.*

reconstruct more precisely the true mean value. The resolution of mass measurement before and after this correction is shown in Fig.4.4. On the same figure we also show the Gaussian fit to the mass resolution distributions.

For a precise measurement of the angles, it is necessary to know exactly the event vertex. The vertex is determined from the combined measurement of tracks in CTD and in the vertex detector using the program VCTRAK [42]. The reconstructed vertex is used only if the number of tracks used for vertex determination is greater than or equal to 2 and if the reduced  $\chi^2$  is less than 10. In Fig.4.5 the reconstructed vertex in the data is compared with the Monte Carlo simulation. The resolution of about 20 cm comes from the proton bunch length.

For the analysis performed in this thesis the *double angle* method has been chosen, because this method depends only on the measured angles and not energies and gives the best resolution of the measurement of kinematical variables.

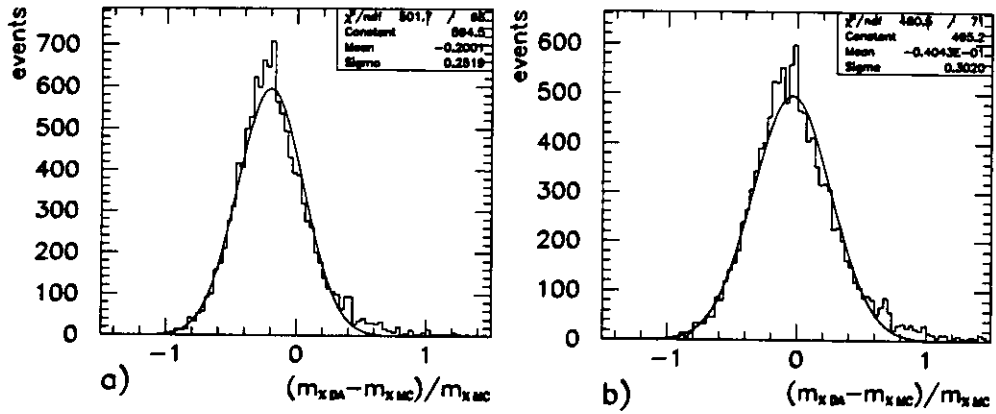


Figure 4.4: *The resolution of the mass reconstruction with double angle method before (a) and after (b) correction to the true mean value. The parameters of the fitted Gaussian distribution are also shown.*

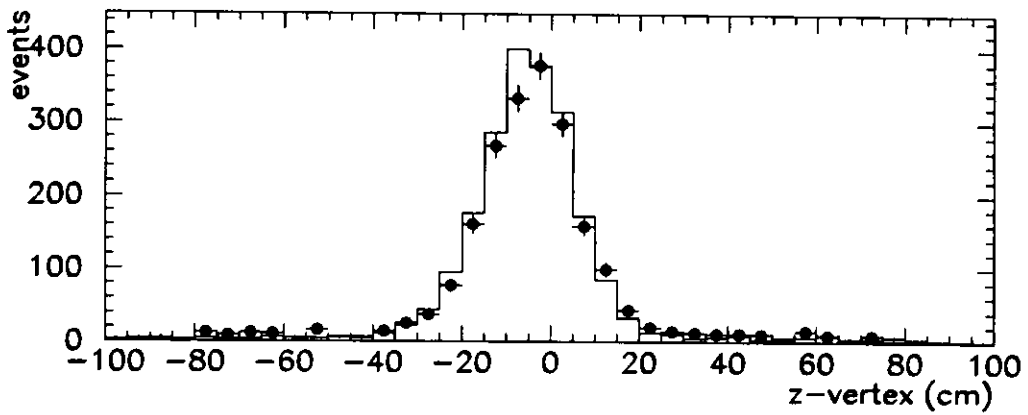


Figure 4.5: *Vertex distribution for Monte Carlo (solid line) and for data (full circles).*

## 5 Monte Carlo simulation

In high energy physics the Monte Carlo (MC) simulation is necessary to study the detector acceptance and the influence of the resolution on the reconstruction of kinematic variables. For every experiment, Monte Carlo simulation programs reflect the complete chain between particles collisions and the reconstruction of the event. An overview of the data taking and the MC simulation chains in ZEUS experiment is schematically shown in Fig.5.1. Event generators produce four-momenta of the final particles according to the desired process in  $ep$  scattering. Output from the generator is passed through the ZEUS detector Monte Carlo simulation program MOZART. The program is based on the GEANT [43] simulation package. The stable particles outgoing from the generator are traced through the whole detector and the response of each individual subdetector is simulated. The output is in the ADAMO [44] data format which is identical to that of ZEUS real data. The online trigger is simulated using the ZGANA trigger simulation program. The raw data and the output from the MC simulation are reconstructed using the ZEUS physics reconstruction program ZEPHYR. This program consists of many individual routines supplied by different physics groups. During the reconstruction several bits are set, which then simplify the selection of desired process in real data. More details of detector (MOZART) and trigger (ZGANA) simulation codes as well as of reconstruction program ZEPHYR are given in [32].

Two different MC programs were used to simulate the diffractive DIS process. The model proposed by Ingelman and Schlein was implemented in the POMPYT 1.0 [50] MC generator. To simulate hard scattering processes the PYTHIA 5.6 [51] MC generator was used, and the hadronisation process was simulated using the JETSET 7.3 [52] MC program. Two sample of events with different pomeron structure functions were generated:  $\beta q(\beta) = \frac{6}{4}\beta(1 - \beta)$  - about 70k events, and  $\beta q(\beta) = 6(1 - \beta)^5$  - about 20k events. The first sample is called *hard* (HP), and the second one *soft* (SP). In both cases the flux of

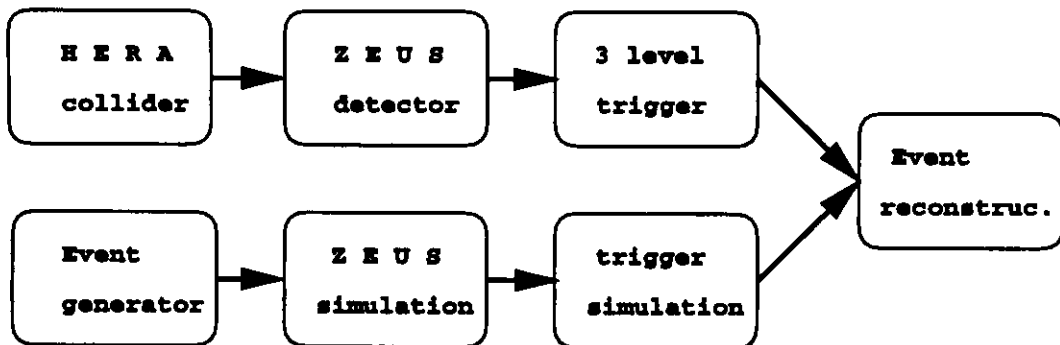


Figure 5.1: Overview of the data and MC simulation chains in the ZEUS experiment.

pomerons in the proton was chosen according to the function:

$$f_{P/p}(x_P, t) = \frac{1}{2.3} \frac{1}{x_P} (3.19e^{8t} + 0.212e^{3t}) \quad (5.1)$$

The model of Nikolaev and Zakharov was implemented in the EPDIFFR [53] MC generator. The model used in MC is based on reference [28] and slightly differs from the one described in Section 2. The Monte Carlo code does not use any prescription of the proton diffractive structure function, and events are generated according to the prescription for the cross section. However one can express the cross section used in MC program in terms of the diffractive structure function, which numerical form can be extracted from the Monte Carlo simulation. The hadronisation process was simulated using the JETSET 7.3 [52] MC program.

In the analysis about 120k events were used. The EPDIFFR generator uses weights to cover phase space more efficiently. For each event the weight is the cross section computed for the generated kinematic variables [54]:

$$\text{weight} = \frac{d\sigma}{d\xi} \cdot \frac{d\xi}{d(RN)} \quad (5.2)$$

where  $\xi$  is any variable or set of variables one uses to describe the process and  $(RN)$  is the generated random number. Cross section predicted by the MC for the simulated process in a given kinematical range reads:

$$\sigma = \frac{\sum_i w_i}{N_{gen}} \pm \frac{\sqrt{\sum_i w_i^2}}{N_{gen}} \quad (5.3)$$

where the sum runs over all generated events. If one wants to compute the cross section in a range smaller than the generation one, the sum of weights should cover only these events which are in the selected range, but the number of generated events in the denominator should still be the full one.

Neither of Monte Carlo programs used for simulation of diffractive events does not include simulation of radiative corrections.

To study the DIS background a sample of 200k neutral current DIS events with  $Q^2 > 4 \text{ GeV}^2$  was used. The hard scattering process was generated using the LEPTO 6.1 [45] program. The effects of the initial and final state photon radiation were included through the HERACLES 4.4 [46] program which was interfaced to LEPTO via the DJANGO 6.0 [47] program. The parametrisation of the proton structure function according to the *MRSD\_* [48] prescription was used because it provides a reasonable description of the proton structure function measured by ZEUS [1]. The hadronisation process was simulated using the color dipole model as implemented in ARIADNE 4.04 [49] program.

## 6 Data selection

### 6.1 Selection of diffractive NC DIS events

During the 1993 running period, a total of  $2 \times 10^6$  events were recorded with the DIS trigger described in subsection 3.5. Events which are written to the data summary tapes (DST) have to pass the TLT NC filters (*normal or high  $Q^2$* ) for the NC selection and the TLT CC filter for the charged current selection.

The event selection procedure is designed to recognize events with a scattered beam electron and to remove remaining beam-gas and photoproduction backgrounds. Electrons are recognized by the spatial pattern of energy deposition in the calorimeter and by the ratio of EMC to HAC energies. The first level of NC DIS event selection was performed during the offline reconstruction of the raw data. Selected events have to satisfy the following requirements:

1. The event has to pass at least one of the two TLT NC filters (*normal or high  $Q^2$* ).
2. The time at which the particle enters the calorimeter cell is extracted from the pulse of the photomultiplier (PMT). The resolution of the time measurement is approximately one nanosecond for a few GeV particle. Time offsets on the individual PMT's are adjusted such that for interactions originating from the nominal interaction point and at the nominal bunch crossing time, the calorimeter cell time equals zero. A time of the global section of the calorimeter (F/B/RCAL) is calculated as an energy weighted average of the individual PMT's.

The calorimeter timing is used to remove the upstream beam-gas interactions. For instance, the energy deposit in the RCAL from an upstream proton-gas interaction occurs early compared to the interactions originating from the nominal vertex. The proton bunch length broadens the time distribution of the particles that enter in the FCAL. For the  $ep$  interactions, the time width of the RCAL is insensitive to the proton bunch length (electron bunch length can be neglected). But for upstream proton-gas interactions, both the FCAL and RCAL time distributions are affected by the proton bunch length.

The following cuts were applied on the timings:  $|t_R| < 6$  ns,  $|t_F| < 8$  ns,  $|t_F - t_R| < 8$  ns,  $|t_G| < 8$  ns.

3. Cosmic muons and further halo muons are rejected using muon finding programs. The programs (MUTRIG, ALHALO2 [55]) use the time signature and characteristic energy deposits in the calorimeter to identify the muons.
4. Sparks (the events with sudden discharges between the calorimeter PMT and PMT shielding) and events with no energy deposit in the calorimeter are rejected using the subroutine RMSPART [55].

5. The quantity  $\delta = \sum_i E_i - p_{z_i} + 2E_\gamma$  has to be greater than 25 GeV, where the sum runs over all calorimeter cells, and  $E_\gamma$  denotes the energy measured in the photon calorimeter of the luminosity monitor.  $\delta$  is calculated forcing the vertex to be at position  $z = 0$ .

After this selection about  $3.8 \times 10^5$  events remained. In order to obtain a clean sample of DIS NC events, the following final selection cuts are applied to the data sample:

1. A minimum energy is required for the electron candidate,  $E'_e > 5$  GeV, in order to have both a high efficiency and purity in the neutral current sample. This cut is also very effective at removing photoproduction background events.
2. Stricter cuts on timing,  $|t_F - t_R| < 6$  ns and  $|t_R| < 6$  ns were applied to reject beam related backgrounds and cosmic rays.
3. The requirement  $y_e < 0.95$  removes fake electrons in the FCAL. This cut has no effect for RCAL electrons, since the 5 GeV cut corresponds to a cut on  $y_e < 0.84$ . The fake electrons arise primarily from photoproduction background.
4. A cut on  $y_{JB}$  is important in reducing the effect of noise on the measurement of kinematic variables. The  $y_{JB}$  cut removes low  $y$  events which have migrated to low  $x$  when using the double angle method. We have chosen the cut value of  $y_{JB} > 0.04$ .
5. The angle and energy of scattered electrons which enters the RCAL close to the beam pipe have is poor determined due to energy leakages. Therefore a 'box' cut on the reconstructed electron position was applied. The position was reconstructed using the ELECPO routines [56]. We require that the reconstructed electron position should satisfy:

$$|x| > 16 \text{ cm} \quad \text{and} \quad |y| > 16 \text{ cm}$$

This cut is further justified by the fact that the amount of dead material is very high in front of the RCAL in this region and is not quite properly simulated in the Monte Carlo.

6. The DIS accepted events were required to have a measured tracking vertex. The correct position of the vertex is very important because it influences the angles of the outgoing particles and hence the reconstruction of kinematic variables. A cut on vertex position  $|V_z| < 40$  cm was applied.

After this selection about 110k events remained. Diffractive DIS events were selected using the cut on the maximum pseudorapidity  $\eta_{max}$  in the event.  $\eta_{max}$  is defined as the pseudorapidity of the calorimeter condensate with energy greater than  $E_{cut}$  that is closest to the outgoing proton beam direction. A condensate is a set of adjacent calorimeter cells with an energy deposit above 100 MeV for pure EMC and above 200 MeV for HAC or mixed energy deposits. The parameter  $E_{cut}$  was chosen to be equal 400 MeV. It

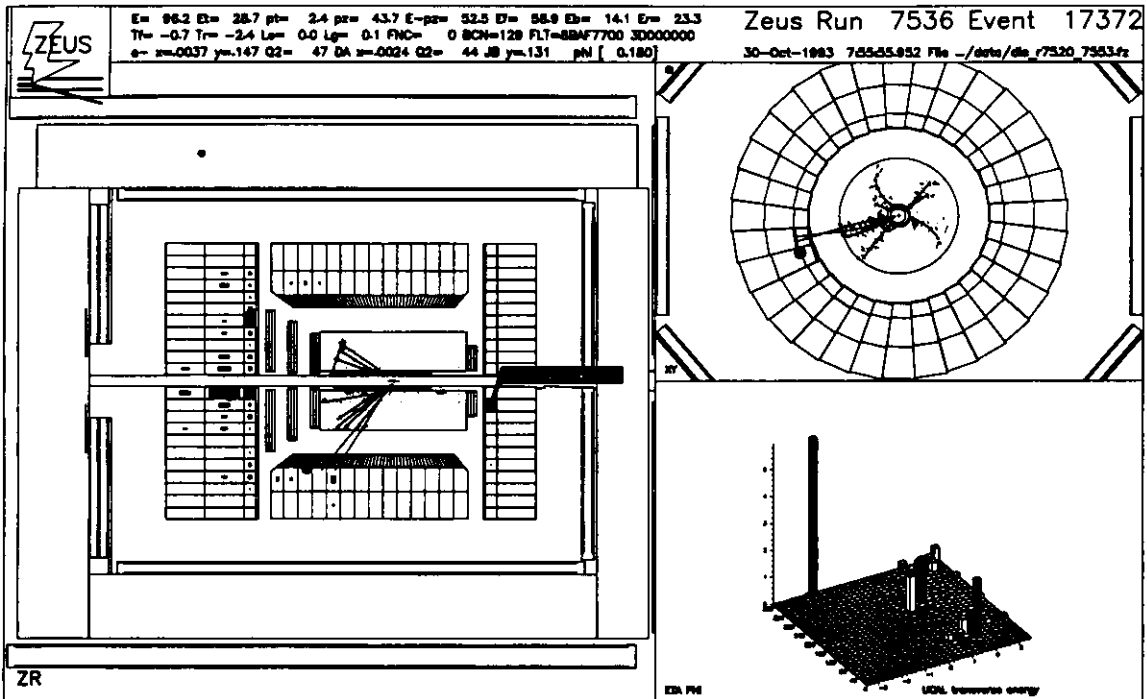


Figure 6.1: Event display of neutral current DIS candidate. Selection cuts described above were applied.

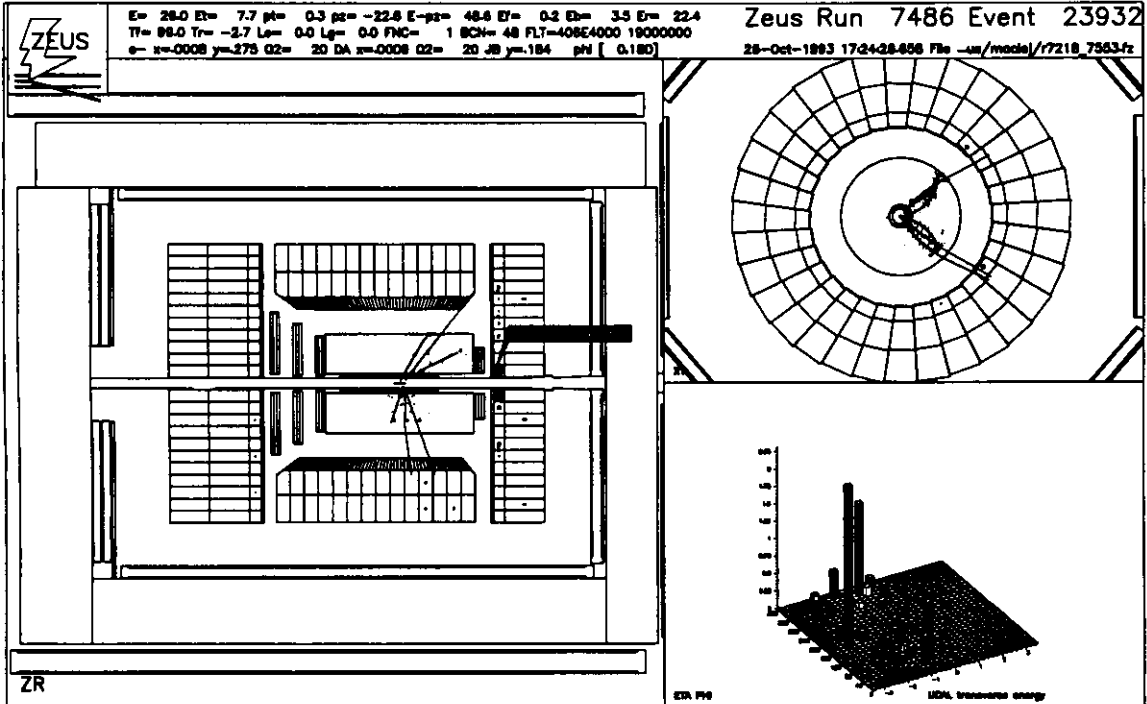


Figure 6.2: Event display of a diffractive DIS candidate. Apart of the DIS selection cuts, the  $\eta_{max}$  cut was applied.

was proved, however, that changes  $\pm 100$  MeV do not influence the distributions. After  $\eta_{max} < 1.5$  cut, 1949 events remained. The cut  $\eta_{max} < 1.5$  selects a pure sample [3] of diffractive events. The contamination from non-diffractive DIS is small.

## 6.2 Background estimation

For a correct measurement of the diffractive structure function, we have to estimate the remaining background in the selected sample, and eventually subtract it. We can distinguish two different types of background in the diffractive subsample: the background to DIS and the DIS background to diffractive events. The main sources of background leading to a fake electron found in the calorimeter arise from photoproduction and beam interactions with the residual gas. In the case of photoproduction, the scattered electron escapes down the beam pipe and a false electron is identified from the energy deposits in the calorimeter. The large cross section for photoproduction makes this background significant. The second class of background comes from statistical fluctuations of the hadronization process which lead to the gap in pseudorapidity in the DIS events. In the following, we present the methods used to estimate the background in the final sample.

### 6.2.1 Photoproduction background

We have determined the photoproduction background from the data itself by investigating the  $\delta$  distribution. From the shape of  $\delta$  as determined from the Monte Carlo, the contribution of diffractive DIS events in the  $\delta$  distribution of the data was fitted. The background contribution from photoproduction events, characterized by lower values of  $\delta$ , was fitted in the data sample as well, such that contributions from the two event types could be disentangled. During the photoproduction background subtraction, all final selection cuts were applied to the data but the  $\delta$  cut.

The  $\delta$  distribution for the DIS MC peaks around a two electron beam energy value and has a radiative tail towards lower values. The shape of the DIS  $\delta$  distribution is well parameterized [57] by the Gaussian distribution (with different widths on either side of a central value) and with an exponential form responsible for the radiative tail. The phenomenological function used to fit the DIS  $\delta$  distribution reads:

$$\Delta_{DIS}^{MC}(\delta) = \begin{cases} p_1 \exp \left[ -\frac{(\delta - \delta_0^{MC})^2}{2\sigma_1^2(MC)} \right] & \delta > \delta_0^{MC} \\ p_2 \exp \left[ -\alpha(\delta - \delta_0^{MC}) \right] + (p_1 - p_2) \exp \left[ -\frac{(\delta - \delta_0^{MC})^2}{2(\sigma_1^2(MC) + \sigma_2^2(MC))} \right] & \delta \leq \delta_0^{MC} \end{cases} \quad (6.1)$$

We fit to the data the same functional form but allowing the central value and width to be different from MC distribution:

$$\Delta_{DIS}^{data}(\delta) = \begin{cases} p_3 p_1 \exp \left[ -\frac{(\delta - \delta_0^{data})^2}{2\sigma_1^2(data)} \right] & \delta > \delta_0^{data} \\ p_3 p_2 \exp \left[ -\alpha(\delta - \delta_0^{data}) \right] + (p_1 - p_2) \exp \left[ -\frac{(\delta - \delta_0^{data})^2}{2(\sigma_1^2(data) + \sigma_2^2(MC))} \right] & \delta \leq \delta_0^{data} \end{cases} \quad (6.2)$$

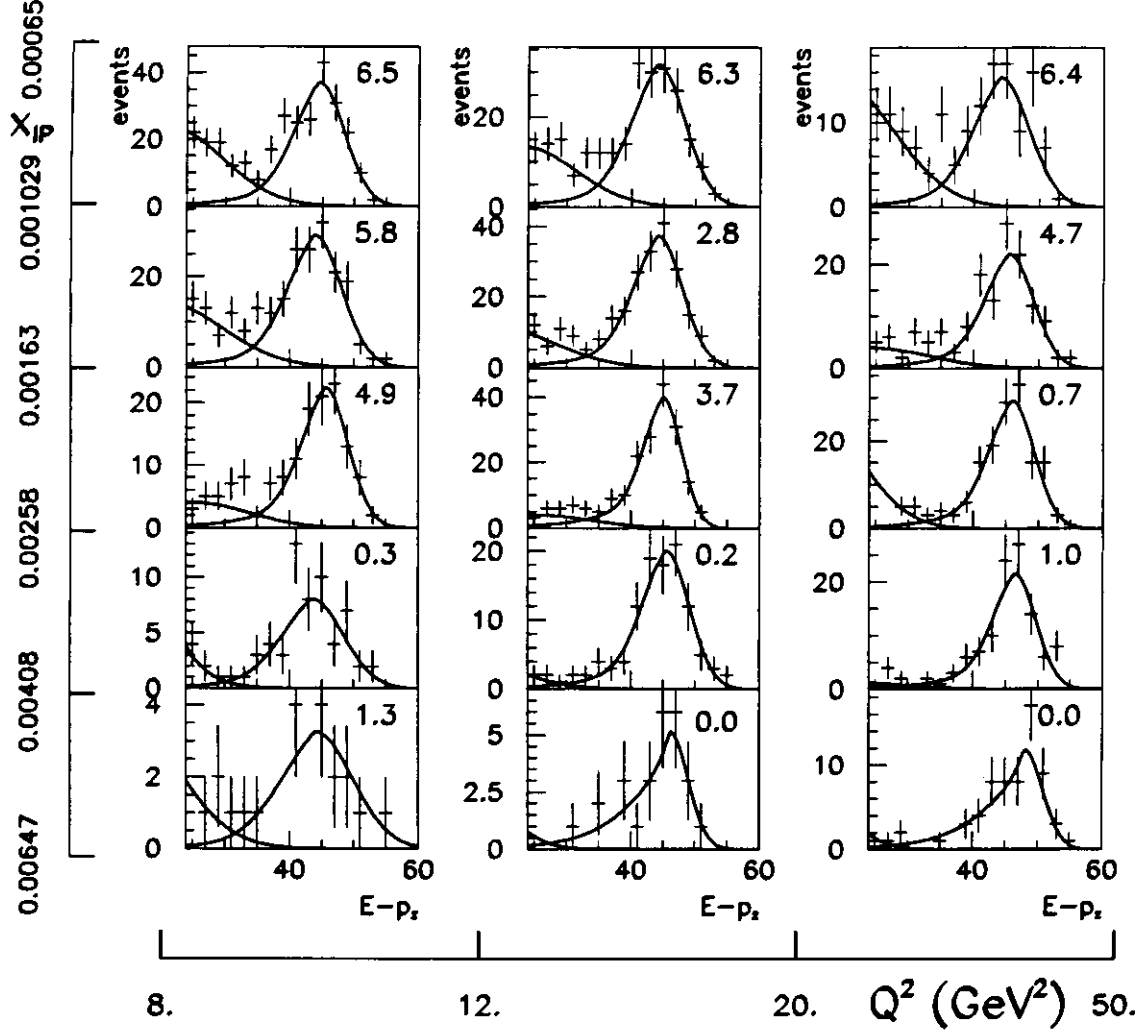


Figure 6.3: *Photoproduction background as estimated from fits to  $E - p_z$  distributions in different  $(x_P, Q^2)$  bins. In the right upper corners the percentage of photoproduction background in selected bin are shown.*

We fit the photoproduction background in the data with the Gaussian shape:

$$\Delta_{PH}^{data}(\delta) = p_4 \exp \left[ -\frac{(\delta - \delta_0^{PH})^2}{2\sigma_3^2(PH)} \right] \quad (6.3)$$

which was found to well parameterize the photoproduction events which pass the DIS selection cuts. The mean value for the photoproduction background was required to be less than 32 GeV, and the width should be in the range between 5 and 10 GeV. For each  $(x_P, Q^2)$  bin used in measurement of  $F_2^{diff}$  the  $\delta$  distribution was fitted with the function:

$$\Delta^{data}(\delta) = \Delta_{DIS}^{data}(\delta) + \Delta_{PH}^{data}(\delta) \quad (6.4)$$

Due to the lack of statistics each bin was integrated over  $\beta$ . The results of the photoproduction background estimation in each bin are shown in Fig.6.3. One can see that the  $\delta > 35$  GeV cut was chosen optimally to distinguish between DIS and photoproduction background. Since the photoproduction background is small in comparison to the errors of the measured structure function, it was not subtracted from data.

### 6.2.2 Beam-gas interactions

In the selected sample we can also have some background from beam interactions with the residual gas in the beam pipe. Proton beam gas interactions are very effectively removed by the calorimeter timing cut, but this cut cannot be used to remove electron gas interactions, because they do not deposit energy in FCAL. After final selection cuts, there were only three events from unpaired bunches left, one from proton-gas collision and two from electron-gas collisions, but only one *e-gas* event fall into the final bins. One can estimate the number of background events in the bin using the electron and proton pilot bunches. The ratio of the electron current in the *ep* bunches to the current in the electron pilot bunch is  $7.8 \pm 1.9$ , and the ratio of the proton current in the *ep* bunches to the current in the proton pilot bunch is  $13.0 \pm 1.9$ . These factors mean that the background from beam-gas collisions is below 1%. An example of electron-gas collision is shown in Fig.6.4.

### 6.2.3 Non-diffractive DIS background

The  $\eta_{max} < 1.5$  cut selects quite a clean diffractive sample, nevertheless we have some contamination of non-diffractive DIS background. This type of background was estimated from the Monte Carlo studies. The number of DIS events which pass the final selection cuts was estimated in each  $(x_P, \beta, Q^2)$  bin during the extraction of  $F_2^{diff}$ . Then the amount of non-diffractive DIS events in each bin was reweighted to the luminosity of the data and subtracted from the sample. The results are presented in the Section 8. In Fig.6.5 we show an example of DIS event which passed the  $\eta_{max} < 1.5$  cut as simulated in MC.

### 6.2.4 Background from double diffractive events

Since the proton system is not detected with present data, we use the term *diffractive* to indicate a single diffractive dissociation of the photon on the proton and double dissociative events where also the proton dissociate. The events with exited proton states with mass  $M_N < 4$  GeV pass the diffractive selection cuts. From the proton-proton measurements of the ratio of double to single dissociative events it was estimated [63], that the fraction of double dissociative events in the data sample is of the order of  $\simeq (15 \pm 10)\%$ . This is independent of  $\beta$  and  $Q^2$  and do not vary significantly with  $x_P$ .

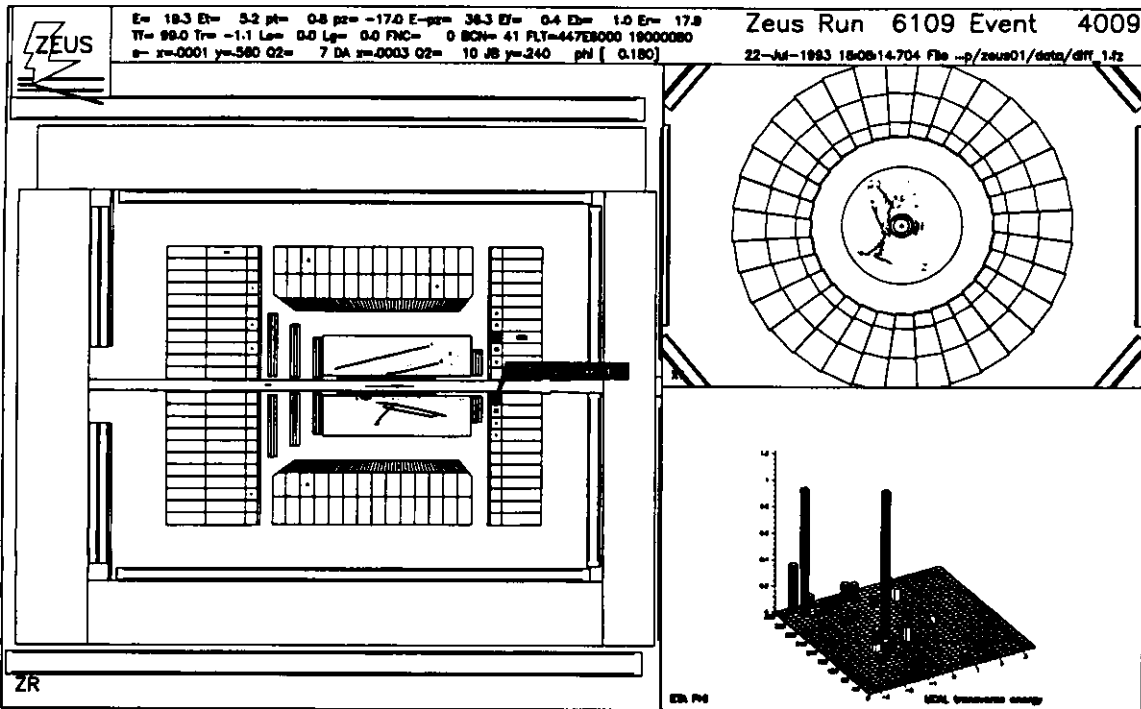


Figure 6.4: Event display of an electron-gas interaction which passed the final diffractive selection cuts.

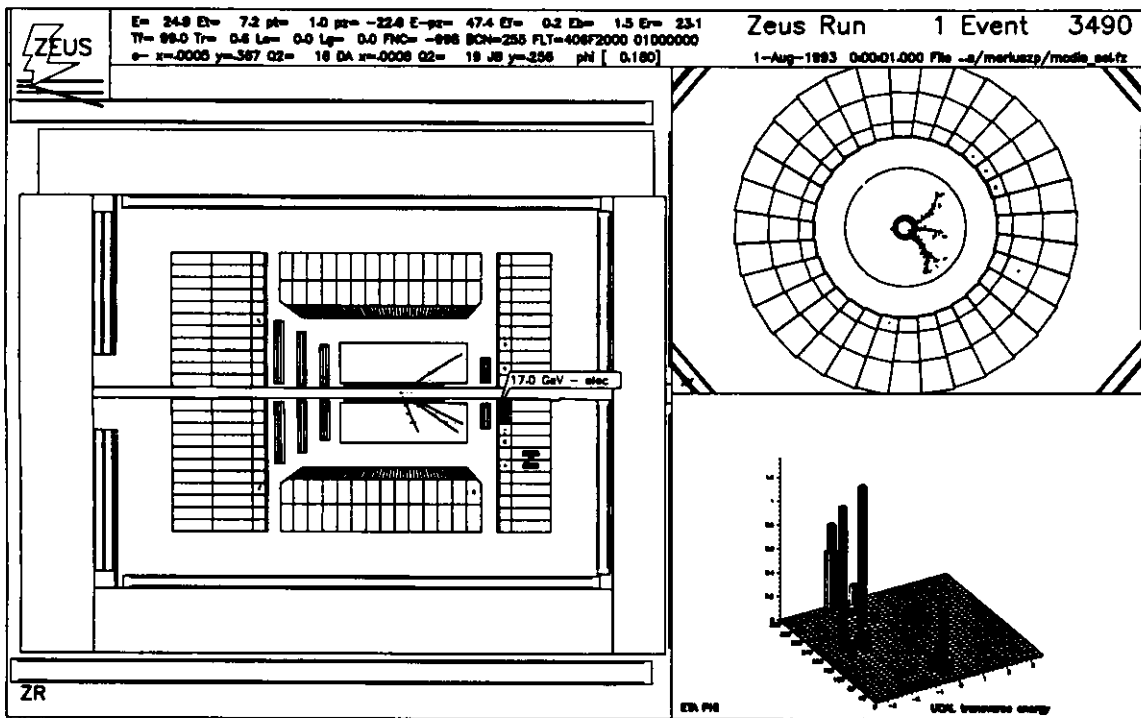


Figure 6.5: Event display of an example of DIS event (taken from Monte Carlo) which passed the final diffractive selection cuts.

## 7 Characteristics of the diffractive DIS events

In this section we present inclusive distributions of diffractive DIS events. We compare the data with various Monte Carlo models disregarding the absolute normalization of the MC, leaving it as a free parameter to be fitted to the data. The properties of diffractive DIS events were extensively studied in [58, 59].

### 7.1 Estimation of diffractive fraction in the DIS cross section

To estimate the fraction of diffractive and non-diffractive events in the DIS data sample one can use the distribution of the maximum pseudorapidity  $\eta_{max}$ . It should be possible to obtain the distribution of the data as a weighted sum of diffractive and non-diffractive parts:

$$\frac{dN}{d\eta_{max}^{data}} = w_{diff} \frac{dN}{d\eta_{max}^{MC\ diff}} + w_{DIS} \frac{dN}{d\eta_{max}^{MC\ DIS}} \quad (7.1)$$

By minimizing  $\chi^2$  for the three distribution, we obtain the weights  $w_{diff}$  and  $w_{DIS}$ . Since the proton fragmentation region is not well reproduced by MC simulation, we use one wide bin for  $\eta_{max} > 4$ . That bin is filled in majority by the non-diffractive DIS component and it gives very little information about relative contribution of diffractive and non-diffractive components in the data. Before fitting the data with diffractive and non-diffractive MC samples, we have to subtract the remaining photoproduction background (it was estimated to be 7% of the total DIS sample). The photoproduction background which pass the final DIS selection cuts is concentrated in the proton fragmentation region (about 80%). For systematic checks, we have tried three different distribution of the photoproduction background:

- (a) all the background events in the proton fragmentation region,
- (b) 80% of the background in the proton fragmentation region and 20% equally distributed among the other bins,
- (c) we do not remove photoproduction background.

As an another systematic check, we changed the number of bins in the distributions. The results are shown in Fig.7.1 and in Table 7.1. The errors shown in the Table 7.1 come from the above systematic checks. In all fits the low  $\eta_{max}$  region is not well fitted because neither NZ nor POMPYT describes the low mass states. The SP model alone does not describes the real data and was not considered in further analysis. The fraction of diffractive component in DIS obtained with a mixture of HP (75%) and SP (25%) is similar to the one determined using the NZ model. The HP model alone predicts a little smaller fraction. This can be understood because both, NZ and HP models have the hard component which is responsible for low  $\eta_{max}$ , but only NZ model has additional soft component which is predicted to be  $\sim 40\%$  of the diffractive cross section.

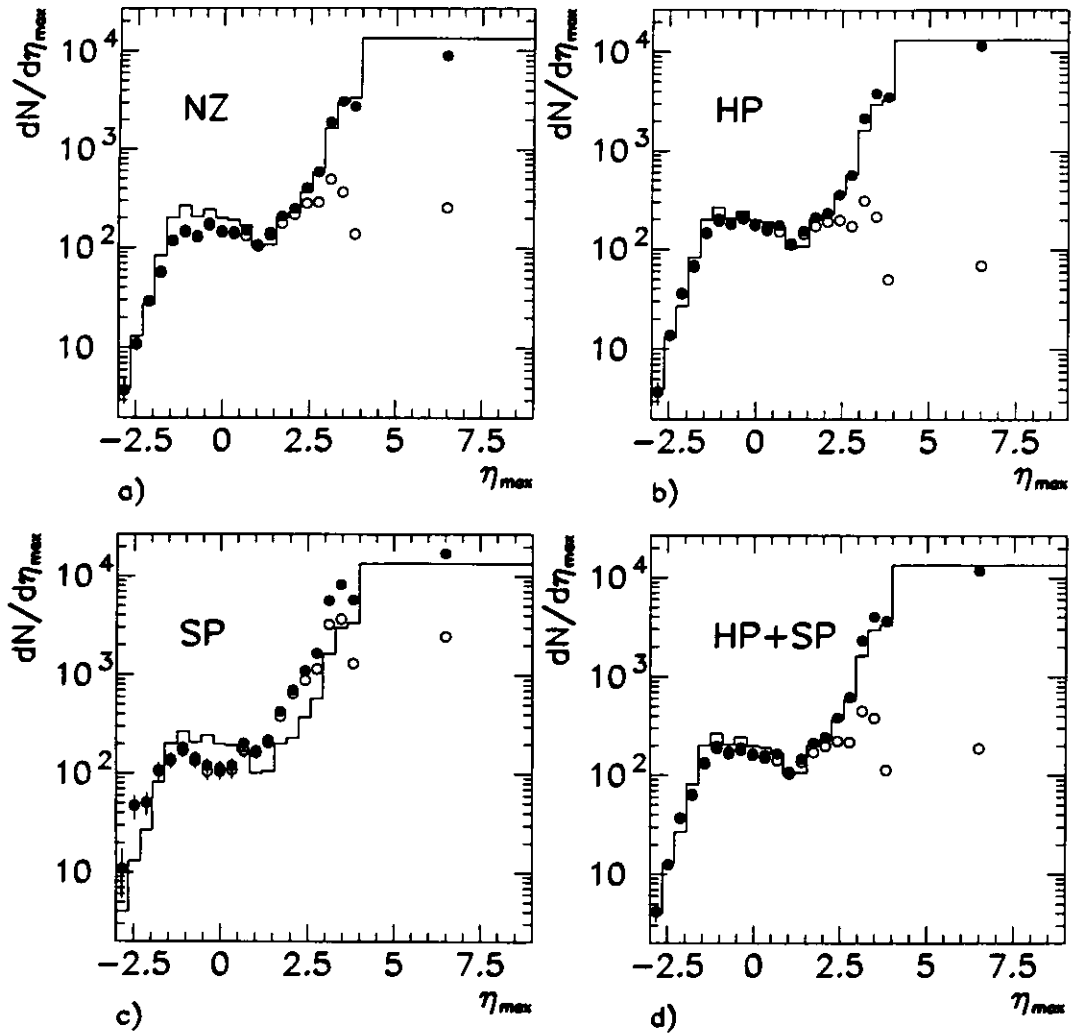


Figure 7.1: Contributions of diffractive and non-diffractive components in the DIS data sample. The open circles represents the contribution from diffractive MC. The filled circles represents the best estimate of the contributions from diffractive and non-diffractive parts. (a) NZ model, (b) HP model, (c) SP model, (d) HP+SP model.

Diffractive MC type	Diffractive contribution (%)	$\frac{\chi^2}{\text{dof}}$
NZ	$14.5 \pm 1.2$	27.1
HP	$12.2 \pm 1.1$	17.3
SP	$39.3 \pm 1.2$	55.7
HP+SP	$14.6 \pm 1.1$	22.3

Table 7.1: Contributions of the diffractive and non-diffractive components to the total DIS cross section.

## 7.2 Inclusive properties of events with a large rapidity gap

In this paragraph, we present the main features of large rapidity gap events. The data shown are uncorrected for detector effects and selection cuts.

We divide the DIS sample into two parts: one with  $\eta_{max} < 1.5$  and the other with  $\eta_{max} > 1.5$ . The correlation between the invariant mass  $m_X$  of the hadrons observed in the calorimeter and the invariant mass  $W_{DA}$  of the  $\gamma^*p$  system is shown in Fig.7.2. The diffractive events are characterized by small values of  $m_X$  in comparison to  $W_{DA}$ . The events span the range of  $W_{DA}$  from 60 to 270 GeV, and for  $W_{DA} > 150$  GeV are well separated from the rest of the sample.

The distributions of kinematic variables,  $x_P$ ,  $\beta$ ,  $x$ ,  $Q^2$ ,  $m_X$ ,  $W$ , after applying final selection cuts are shown in Fig.7.3.

The data are compared with MC predictions of NZ and HP models. The errors on the data points are only statistical. In general, both models describe the data. But in

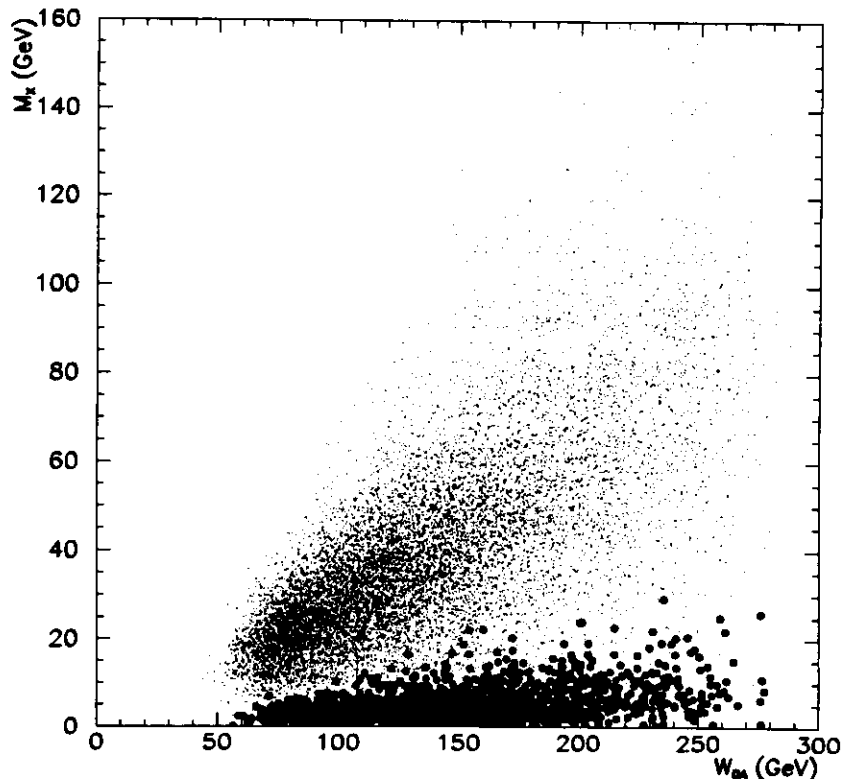


Figure 7.2: Correlation between the invariant mass  $m_X$  of the hadrons observed in the calorimeter and the invariant mass,  $W_{DA}$ , of the  $\gamma^*p$  system. Events with a large rapidity gap,  $\eta_{max} < 1.5$  are shown as a big dots, and events with  $\eta_{max} > 1.5$  are shown as points.

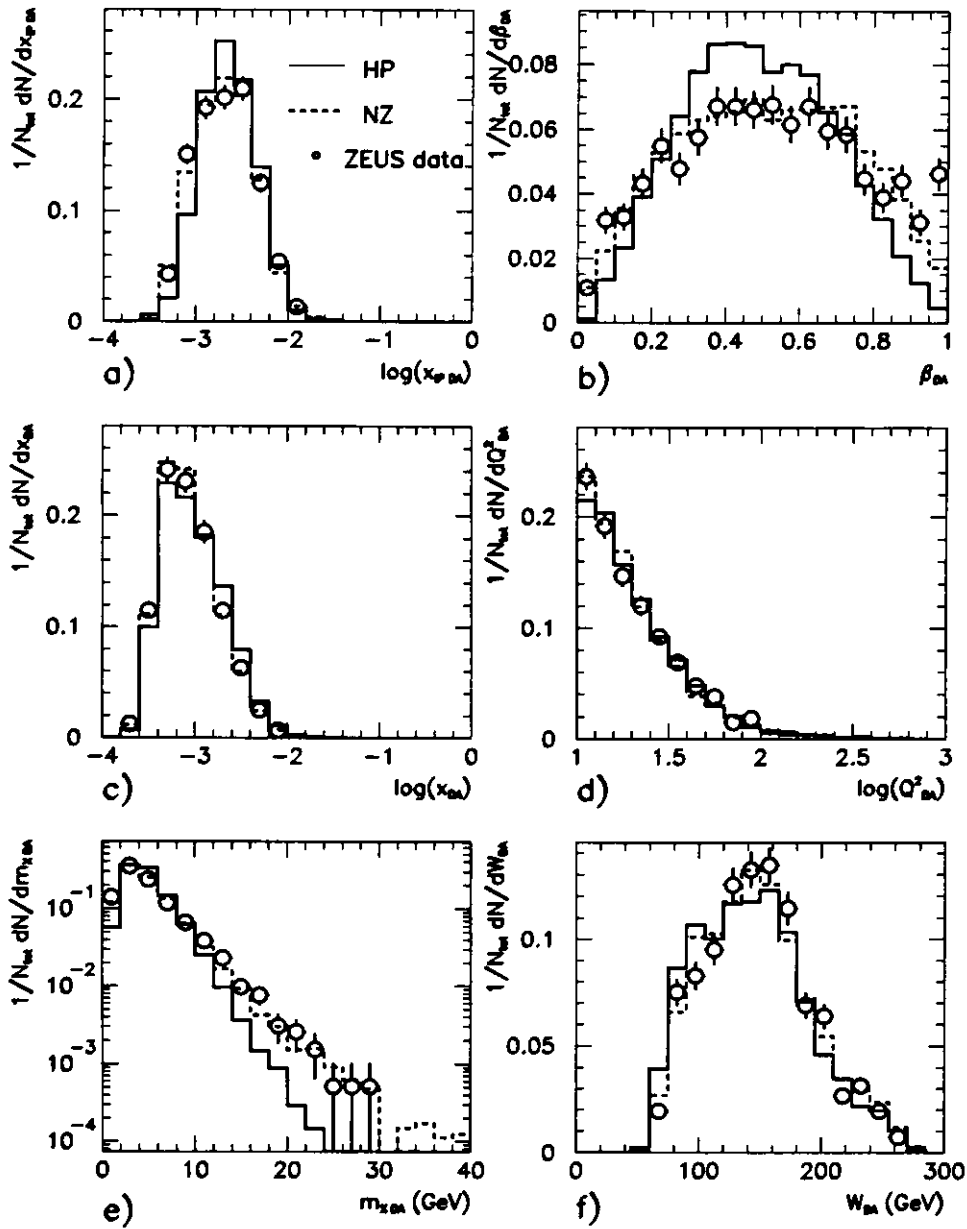


Figure 7.3: Comparison of different kinematic variables of events with large rapidity gap with Monte Carlo predictions. Hard POMPYT MC - solid line, EPDIFFR MC - dashed line, ZEUS data - open circles.

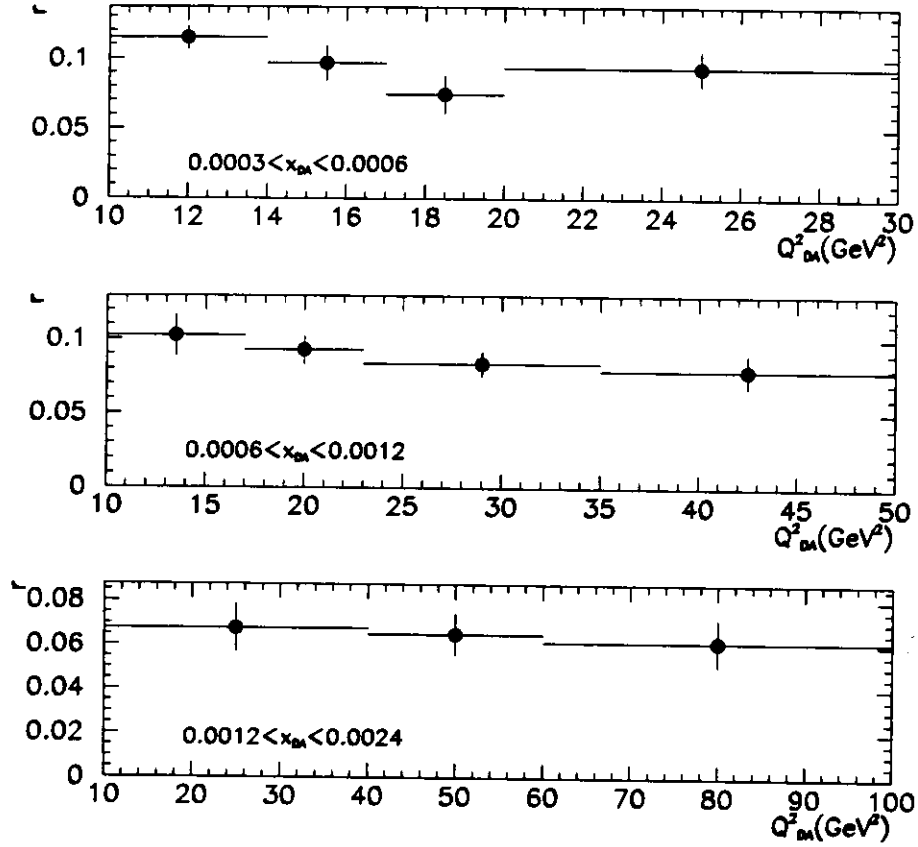


Figure 7.4: Fraction of events with a large rapidity gap,  $\eta_{max} < 1.5$ , as a function of  $Q_{DA}^2$  for different ranges of Bjorken  $x_{DA}$ . No acceptance corrections have been applied.

distributions of  $m_X$  and  $\beta$ , can be observed differences. The NZ model fit to the data still quite well, whereas the HP model does not reproduce the large  $m_X$  tail and underestimates the observed number of events at low  $\beta$  values.

In Fig.7.4 the ratio  $r$  of the number of events with  $\eta_{max} < 1.5$  to the total number of DIS events as a function of  $Q_{DA}^2$  for three different intervals in Bjorken  $x_{DA}$  is shown. The constancy of  $r$  with  $Q_{DA}^2$  suggests that the production mechanism responsible for the large rapidity gap events should be a leading twist effect (the same was observed in the total DIS sample [60]).

## 8 Determination of $F_2^{diff}(x_P, \beta, Q^2)$

### 8.1 Bin selection and acceptances

The bin sizes in  $x_P$ ,  $\beta$  and  $Q^2$  used during the extraction of  $F_2^{diff}$  were chosen to be larger than the measurement resolutions:

$$\Delta\beta \geq \sigma_\beta(x_P, \beta, Q^2) \quad (8.1)$$

$$\Delta x_P \geq \sigma_{x_P}(x_P, \beta, Q^2) \quad (8.2)$$

$$\Delta Q^2 \geq \sigma_{Q^2}(x_P, \beta, Q^2) \quad (8.3)$$

The resolution and the systematic shift of  $x_P$ ,  $\beta$  and  $Q^2$  after final selection cuts are shown in Fig.8.1. The fractional difference between measured and true values is plotted as a function of the measured value. The systematic shift is given by the horizontal lines and the resolution is given by the error bars. Due to the lack of statistic and by requiring that relations (8.1-3) are to be satisfied, we only use three bins in  $Q^2$ : 8 – 12, 12 – 20 and 20 – 50 GeV<sup>2</sup>. The fourth bin, 50 <  $Q^2$  < 100 GeV<sup>2</sup> is discussed in this section, but is not used in final measurements. The selected bin ranges in the  $(x_P, \beta)$  plane are shown in Figs.8.2–4.

The events measured in a given bin could have originated from other bins in the  $(x_P, \beta)$  plane. The migration of events in the  $(x_P, \beta)$  plane is shown in Fig.8.2. The base of the arrow is at the average  $x_P$  and  $\beta$  for a given bin. The head of the arrow is at the average reconstructed  $x_P$  and  $\beta$ . The migration between different  $Q^2$  bins is small and was neglected in the following analysis.

To check the quality of chosen bins, we define the notions of *acceptance* and *smearing*. The acceptance is defined as the number of events which are generated in a given bin and are selected after final selection cuts divided by the number of events which are generated in this bin:

$$a_i(x_P, \beta) = \frac{N_i^{sel}(x_P, \beta)}{N_i(x_P, \beta)} \quad (8.4)$$

The values of acceptance are shown in Fig.8.3. The better bin the closer to one is the value of acceptance. However, numbers very close or exactly equal to one (especially for high  $\beta$  and  $Q^2$  bins) are connected with very low statistics in these bins and therefore errors for these numbers are big.

The smearing is the number of events which are generated in the bin and measured in the bin divided by the number of events which are generated in the bin and selected:

$$s_i(x_P, \beta) = \frac{M_i^{in}(x_P, \beta)}{N_i^{sel}(x_P, \beta)} \quad (8.5)$$

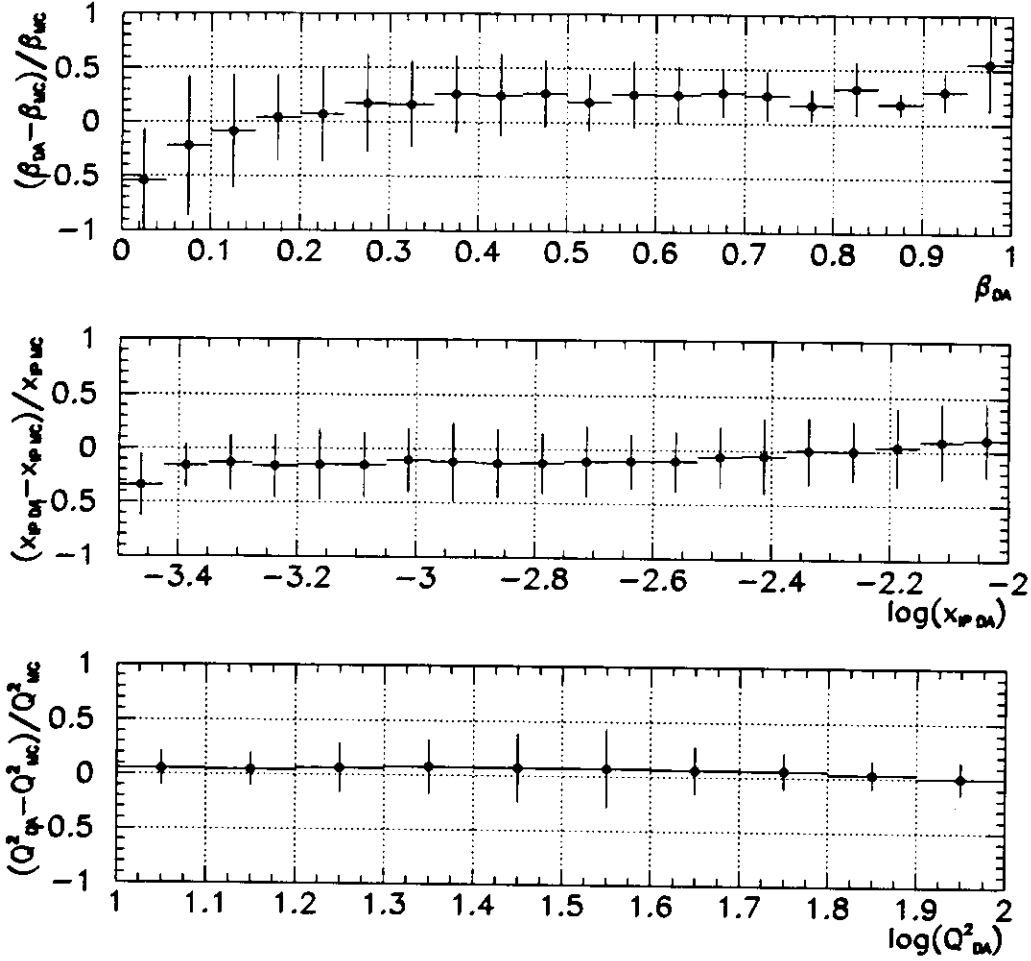


Figure 8.1: *Fractional difference between reconstructed and generated values of  $\beta$ ,  $x_P$  and  $Q_{DA}^2$  as a function of the reconstructed value. The horizontal lines give the systematic shift and the error bars give the measurement resolution.*

The values of smearing are shown in Fig.8.4. Low values of smearing indicate that events are lost either by selection cuts or by migration. No number given in a bin on Fig.8.3–4 means that the value is less than 1%.

One can also define the *purity* of the bin as the number of original events measured in the bin divided by the number of events generated in the bin. The purity can be obtained by multiplying the smearing by the acceptance.

In the final analysis, we use only bins with a smearing above 20% (typically about 35%) and with an acceptance above 10% (typically about 60%). These requirements allow only to consider bins with  $x_P < 0.01$  and  $\beta > 0.1$ . In that range the non-diffractive component can also be safely estimated and removed from the diffractive sample. We do not use bins having  $\beta > 0.8$ , because for so small masses vector-meson production dominates. For  $Q^2$  less than 8 GeV<sup>2</sup>, the event acceptance is below 50% due to the box cut on the electron position. Therefore, we do not consider bins below that value of  $Q^2$ .

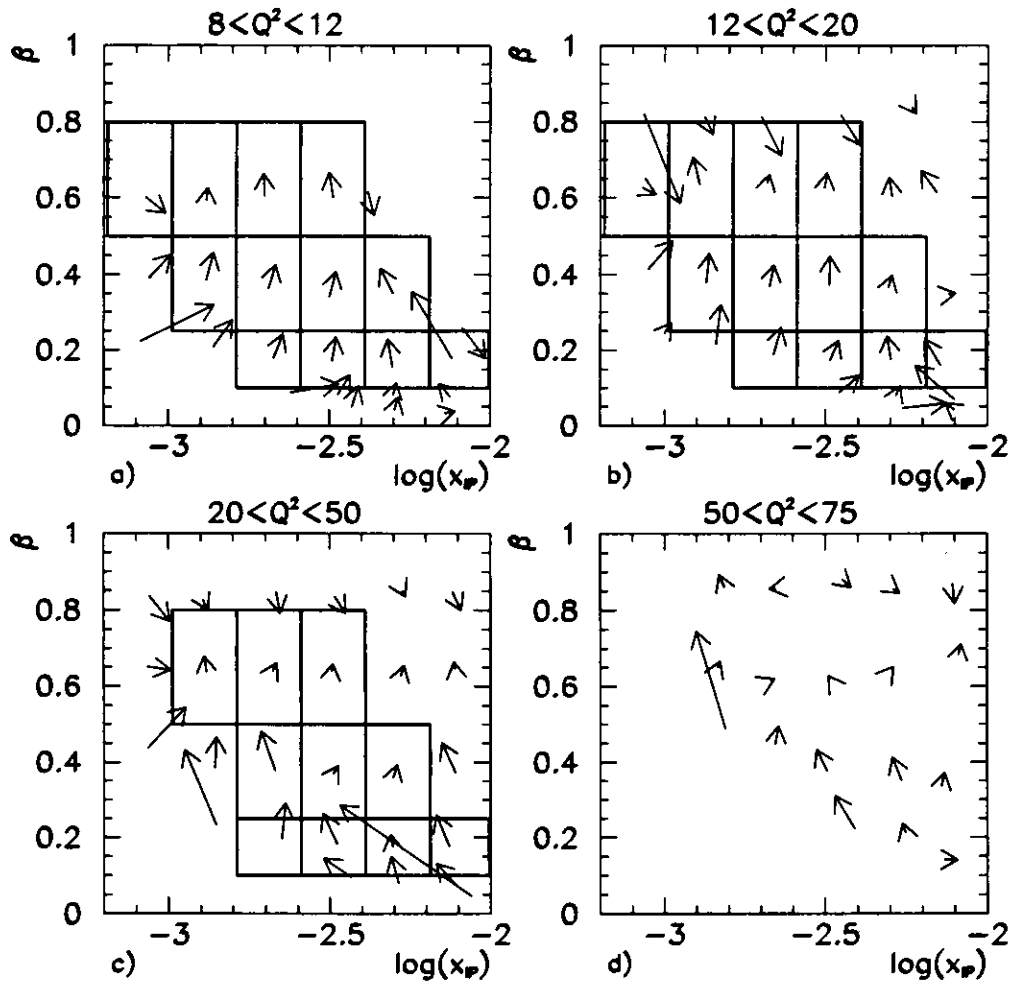


Figure 8.2: Migration in  $(x_P, \beta)$ -plane for different  $Q^2$  bins. The base of the arrow is at the average  $x_P$  and  $\beta$  for a given bin. The head of the arrow is at the average reconstructed  $x_P$  and  $\beta$  for the events which originated in the bin. The bins chosen for the final analysis are also shown.

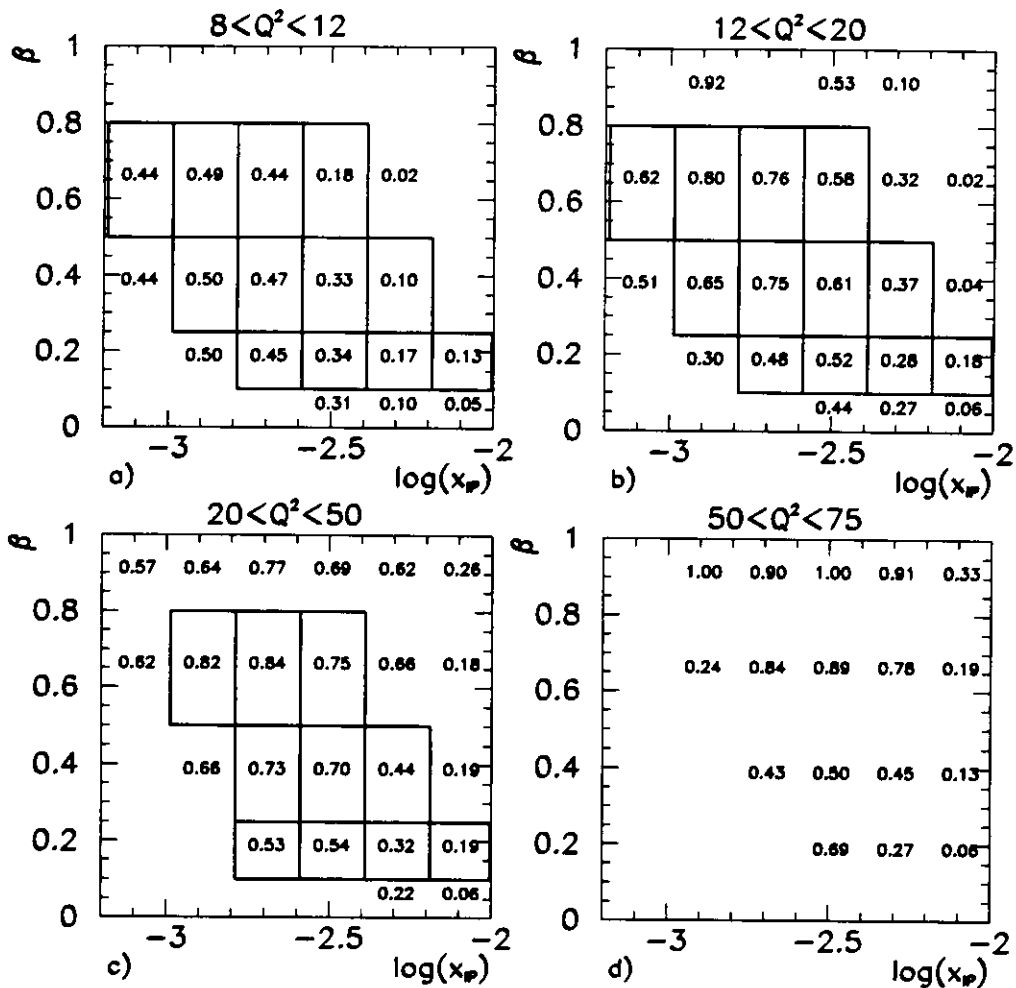


Figure 8.3: Acceptance for each bin. The better bin the the closer to one is the value of the acceptance. The bins chosen for the final analysis are also shown. Note, that bins with high values of  $\beta$  and  $Q^2$  are not too much populated and therefore the numbers given for these bins have big errors.

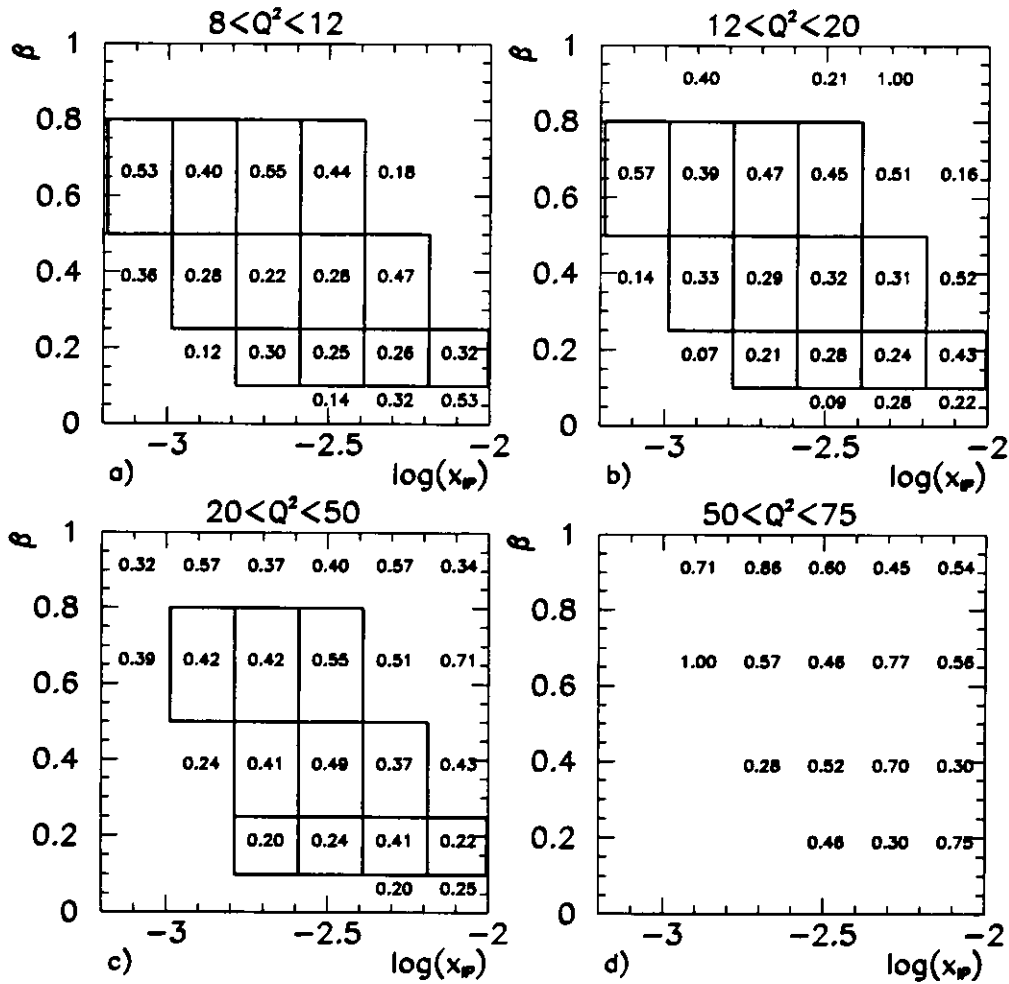


Figure 8.4: Smearing for each bin. Low values of smearing indicate that event are lost either by selection cuts or by migration. The bins chosen for the final analysis are also shown. Note, that bins with high values of  $\beta$  and  $Q^2$  are not too much populated and therefore the numbers given for these bins have big errors.

## 8.2 Unfolding procedure

The experimentally measured distributions are always affected by trigger, selection cuts, reconstruction methods and detector acceptance and resolution. They differ significantly from the “true” distributions which can be compared with our theoretical predictions. In order to determine true distributions from the measured ones we often use an unfolding procedure. There are many different unfolding techniques [61]. The method used in this analysis is based on the Bayes theorem and was proposed in [62].

Let us assume we have several independent causes ( $C_i$ ,  $i = 1, 2, \dots, n_c$ ) which can produce several possible effects ( $E_j$ ,  $j = 1, 2, \dots, n_E$ ) and we know the initial probability of the causes  $P(C_i)$  and the conditional probability of the  $i$ -th cause to produce the  $j$ -th effect  $P(E_j|C_i)$ . Then the Bayes formula can be written down in the form:

$$P(C_i|E_j) = \frac{P(E_j|C_i) \cdot P(C_i)}{\sum_{l=1}^{n_c} P(E_j|C_l) \cdot P(C_l)} \quad (8.6)$$

It means that if we observe a single  $j$ -th event, the probability that it has been due to the  $i$ -th cause is proportional to the probability of the cause times the probability of the cause to produce the effect. The Bayes formula has the power to increase the knowledge of  $P(C_i)$  by increasing the number of observations. We indicate the initial probability of the causes with  $P_0(C_i)$ . If there is no a priori prejudice on  $P_0(C_i)$ , the unfolding process can be started from a uniform distribution. The final distribution depends also on  $P(E_j|C_i)$ . These probabilities must be calculated with Monte Carlo methods.

After  $N_{obs}$  experimental observations, one obtains a distribution of frequencies  $\underline{n}(E) \equiv \{n(E_1), n(E_2), \dots, n(E_{obs})\}$ . The expected number of events to be assigned to each of the causes and only due to the observed events can be calculated using the formula:

$$\hat{n}(C_i)|_{obs} = \sum_{j=1}^{n_E} n(E_j) P(C_i|E_j) \quad (8.7)$$

Taking into account the inefficiency  $\epsilon_i \equiv \sum_{j=1}^{n_E} P(E_j|C_i)$ , the best estimate of the true number of events is then:

$$\hat{n}(C_i) = \frac{1}{\epsilon_i} \sum_{j=1}^{n_E} n(E_j) P(C_i|E_j) \quad \epsilon_i \neq 0 \quad (8.8)$$

If  $\epsilon_i = 0$  then  $\hat{n}(C_i)$  will be set to zero, since the experiment is not sensitive to the cause  $C_i$ . From these unfolded events, we can estimate the true total number of events, the final probabilities of the causes and the overall efficiency:

$$\hat{N}_{true} = \sum_{i=1}^{n_c} \hat{n}(C_i) \quad (8.9)$$

$$\hat{P}(C_i) \equiv P(C_i|\underline{n}(E)) = \frac{\hat{n}(C_i)}{\hat{N}_{true}} \quad (8.10)$$

$$\hat{\epsilon} = \frac{N_{obs}}{\hat{N}_{true}} \quad (8.11)$$

It is important to remark that  $\hat{\epsilon}$  may differ from the a priori overall efficiency  $\epsilon_0$  calculated from reconstructed and generated Monte Carlo events:

$$\epsilon_0 = \frac{N_{rec}}{\hat{N}_{gen}} = \frac{\sum_{i=1}^{n_C} \epsilon_i P_0(C_i)}{\sum_{i=1}^{n_C} P_0(C_i)} \quad (8.12)$$

Using the method described above, the unfolding procedure is performed through the following steps:

1. choose the initial distribution of  $\underline{P}_0(C_i)$  from the best knowledge of the process under study,
2. calculate  $\hat{n}(C)$  and  $\hat{P}(C)$ ,
3. make a  $\chi^2$  comparison between  $\hat{n}(C)$  and  $\underline{n}_0(C)$ ,
4. replace  $\underline{P}_0(C)$  by  $\hat{P}(C)$ , and  $\underline{n}_0(C)$  by  $\hat{n}(C)$  and start again;  
if, after the second iteration the value of  $\chi^2$  is "small enough", stop the iteration;  
otherwise go to step 2.

The uncertainties of the unfolded distribution come mainly from the statistical error on  $n(E_j)$  and from the limited number of simulated events used for the calculation of  $P(E_j|C_i)$ .

In the case of the measurement of  $F_2^{diff}$  the effects  $E_j$  are the observations of an event in a bin of measured quantities  $(\Delta x_P, \Delta\beta)_{meas}$ , and the causes  $C_i$  are all the possible bins of the true values  $(\Delta x_P, \Delta\beta)_{true}$ . As the initial distribution of  $\underline{P}_0(C_i)$  we use the prediction of the Nikolaev-Zakharov model (EPDIFFR MC) which fits the data very well.

The number of true events in a bin is related to the differential cross section and luminosity by:

$$\iiint \frac{d^2\sigma}{dx_P d\beta dQ^2} dx_P d\beta dQ^2 = \frac{N(x_P, \beta, Q^2)}{L} \quad (8.13)$$

where the integration is only taken over the bin and  $L$  is the integrated luminosity. Different models of the pomeron lead to different values of  $F_2^{diff}$ . The differential cross sections for two different parametrisations of  $F_2^{diff}$  can be related by:

$$\frac{d^2\sigma_1/dx_P d\beta dQ^2}{d^2\sigma_2/dx_P d\beta dQ^2} = \frac{F_{21}^{diff}(x_P, \beta, Q^2)}{F_{22}^{diff}(x_P, \beta, Q^2)} \quad (8.14)$$

Once the true distribution of data  $N^{data}(x_P, \beta, Q^2)$  is found, the value of  $F_{2\ data}^{diff}$  for the selected bin can be determined from:

$$F_{2\ data}^{diff}(x_P, \beta, Q^2) = \frac{N^{data}(x_P, \beta, Q^2)/L^{data}}{N^{MC}(x_P, \beta, Q^2)/L^{MC}} F_{2\ MC}^{diff}(x_P, \beta, Q^2) \quad (8.15)$$

The statistical error on the measured  $F_{2\ data}^{diff}$  is calculated from the statistical uncertainties of the MC distribution  $N^{MC}(x_P, \beta, Q^2)$  and from the distribution of unfolded data  $N^{data}(x_P, \beta, Q^2)$ .

### 8.3 Presentation of the final results

The proton diffractive structure function  $F_2^{diff}$  has been measured in the kinematic range of  $6.5 \cdot 10^{-4} < x_P < 10^{-2}$ ,  $0.1 < \beta < 0.8$  and  $8 < Q^2 < 50 \text{ GeV}^2$ . The final results for  $F_2^{diff}$ , for the  $540 \text{ nb}^{-1}$  ( $\pm 2.5\%$ ) integrated luminosity, are shown in Table 8.1 and in Fig.8.5. The statistical errors include statistical uncertainties from the Monte Carlo program used for the unfolding. The systematic errors were obtained on the base of systematic checks discussed in the next subsection, adding in quadrature deviations from the central values (obtained for nominal cuts).

The data show that  $F_2^{diff}$  falls rapidly as a function of  $x_P$ . The dependence on  $\beta$  and  $Q^2$  in the measured kinematical range is weak.

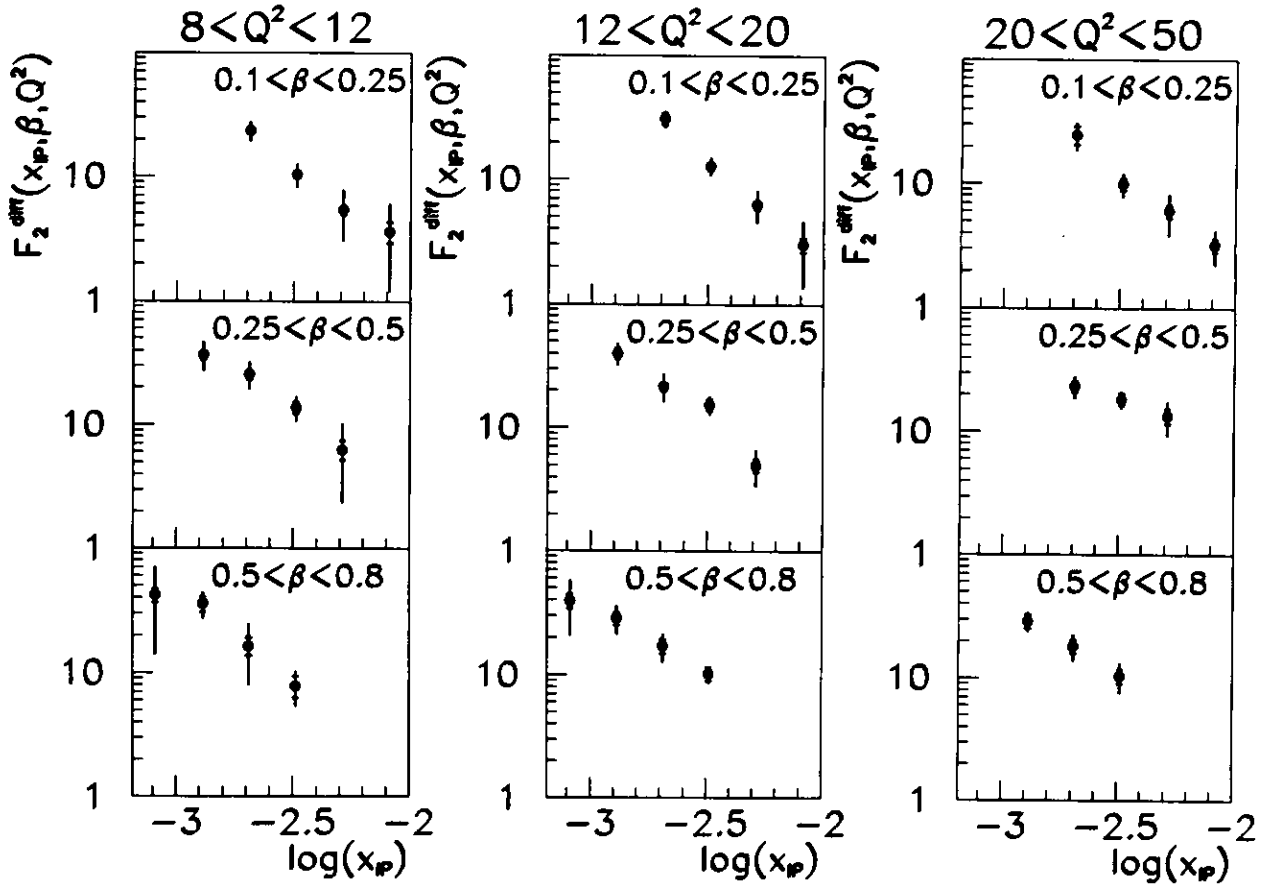


Figure 8.5: Final results for  $F_2^{diff}$  measurement.  $F_2^{diff}$  is shown as a function of  $x_P$  in different  $\beta$  and  $Q^2$  bins. The inner error bars show statistical errors, the full error bars correspond to the statistical and systematic errors added in quadrature. The data include an estimated 15% contribution due to double dissociation. The overall normalization uncertainty of 2.5% due to the luminosity uncertainty is not included.

$Q^2$ (GeV <sup>2</sup> )	$\beta$	$x_F$	#events	DIS back.	$F_2^{diff}$	$\pm$ (stat)	$\pm$ (sys)
10	0.175	0.00205	52	2.5	23.4	$\pm$ 2.0	$\pm$ 3.6
10	0.175	0.00325	54	5.1	10.4	$\pm$ 0.9	$\pm$ 2.1
10	0.175	0.00515	24	5.1	5.4	$\pm$ 0.5	$\pm$ 2.3
10	0.175	0.00815	10	0.0	3.6	$\pm$ 0.7	$\pm$ 2.3
10	0.375	0.00130	69	0.0	36.9	$\pm$ 3.5	$\pm$ 9.3
10	0.375	0.00205	48	5.1	25.6	$\pm$ 2.5	$\pm$ 5.8
10	0.375	0.00325	28	2.5	13.7	$\pm$ 1.5	$\pm$ 2.8
10	0.375	0.00515	11	0.0	6.3	$\pm$ 1.1	$\pm$ 3.8
10	0.650	0.00081	51	0.0	42.0	$\pm$ 5.1	$\pm$ 27.6
10	0.650	0.00130	23	1.3	35.8	$\pm$ 4.9	$\pm$ 6.9
10	0.650	0.00205	33	1.3	16.5	$\pm$ 2.7	$\pm$ 8.1
10	0.650	0.00325	9	0.0	7.8	$\pm$ 1.5	$\pm$ 2.0
15	0.175	0.00205	31	2.5	30.8	$\pm$ 3.5	$\pm$ 3.3
15	0.175	0.00325	47	11.4	13.0	$\pm$ 1.2	$\pm$ 1.9
15	0.175	0.00515	38	2.5	6.3	$\pm$ 0.6	$\pm$ 1.7
15	0.175	0.00815	17	5.1	3.0	$\pm$ 0.4	$\pm$ 1.6
15	0.375	0.00130	83	1.3	40.0	$\pm$ 4.0	$\pm$ 7.3
15	0.375	0.00205	65	5.1	21.7	$\pm$ 2.1	$\pm$ 5.2
15	0.375	0.00325	57	3.8	15.3	$\pm$ 1.6	$\pm$ 2.1
15	0.375	0.00515	27	2.5	5.0	$\pm$ 0.6	$\pm$ 1.5
15	0.650	0.00081	45	1.3	39.4	$\pm$ 5.0	$\pm$ 18.0
15	0.650	0.00130	49	1.3	28.7	$\pm$ 3.5	$\pm$ 6.6
15	0.650	0.00205	32	2.5	17.1	$\pm$ 2.2	$\pm$ 3.9
15	0.650	0.00325	36	0.0	10.2	$\pm$ 1.3	$\pm$ 1.0
32	0.175	0.00205	19	1.3	24.6	$\pm$ 4.0	$\pm$ 4.7
32	0.175	0.00325	33	0.0	9.9	$\pm$ 1.1	$\pm$ 1.9
32	0.175	0.00515	34	5.1	6.0	$\pm$ 0.7	$\pm$ 2.1
32	0.175	0.00815	15	1.3	3.2	$\pm$ 0.4	$\pm$ 0.9
32	0.375	0.00205	46	3.8	23.2	$\pm$ 2.5	$\pm$ 4.2
32	0.375	0.00325	41	3.8	18.2	$\pm$ 2.0	$\pm$ 2.3
32	0.375	0.00515	34	3.8	13.3	$\pm$ 1.7	$\pm$ 3.8
32	0.650	0.00130	44	0.0	29.0	$\pm$ 3.7	$\pm$ 3.5
32	0.650	0.00205	38	2.5	18.2	$\pm$ 2.3	$\pm$ 3.8
32	0.650	0.00325	31	5.1	10.4	$\pm$ 1.4	$\pm$ 2.5

Table 8.1: Final results for  $F_2^{diff}$  measurement. The data include an estimated 15% contribution due to double dissociation. The overall normalization uncertainty of 2.5% due to the luminosity uncertainty is not included.

## 8.4 Systematic errors

The systematic error assigned to the measured  $F_2^{diff}$  in each  $(x_P, \beta, Q^2)$  bin has been obtained from several systematic checks of conditions under which the structure function was extracted.

The following systematic effects increase the systematic error assigned to the measured  $F_2^{diff}$  in each  $x_P$  and  $\beta$  bins:

1. Error due to the luminosity uncertainty (2.5%).
2. Error due to the electron energy scale. This error comes from the fact that dead material is not well simulated in Monte Carlo. However, since the double angle method, which is not sensitive to electron energy, is used, the error affects only selection cuts and not the kinematic reconstruction.
3. Error due to the electron position measurement. The reconstruction of the electron position affects the reconstructed kinematic variables since the angle  $\theta$  is determined using the measured position in the calorimeter.
4. Error due to the reconstruction of the event vertex. The determination of the vertex influence the kinematic reconstruction since the vertex is used to determine the angles. Error on the vertex has also an effect on selection criteria through the  $\delta$ -cut.
5. Error due to simulation of hadronic energy distribution in the calorimeter. A mismatch in the angular distribution of the hadronic activity in the detector and in the Monte Carlo leads to an error on the reconstructed  $\gamma$ .
6. Photoproduction background leads to larger values of measured  $F_2^{diff}$ . The photoproduction background was estimated to be below the measurement resolution.
7. Error due to noise in the calorimeter. The noise leads generally to a larger measured  $y$ .
8. Choice of the reconstruction and unfolding methods.
9. The effects of the QED radiation on the smearing of the kinematic variables and of the  $F_L^{diff}$  contribution to the  $F_2^{diff}$  were checked to be smaller than the statistical errors of measured  $F_2^{diff}$  [3].

The following systematic checks were performed to estimate the uncertainties due to selection cuts, background estimation and unfolding:

1. The cut on electron energy was changed from 5 GeV to 10 GeV.

2. The electron finder EEXOTIC [55] was used instead of ELEC5 [55] to select electron candidates.
3. The cut on  $y_{JB}$  was lowered to 0.3 and raised to 0.5.
4. The cut on  $E - p_z$  was changed to  $40 < E - p_z < 60$  and to  $30 < E - p_z < 60$ .
5. Hard POMPYT was used to unfold the data instead of Nikolaev–Zakharov MC.
6. The cut on  $\eta_{max}$  was changed to  $\eta_{max} < 1$  and to  $\eta_{max} < 2$ .
7. The number of iteration in unfolding procedure was changed by two.
8. The cut on the vertex was changed to  $|z| < 30cm$  and to  $|z| < 50cm$ .

The results of the above systematic checks are summarized in Tables 8.2–4. In most bins, the  $F_2^{diff}$  extracted under different conditions agree with the values obtained by nominal cuts within the statistical errors. The total systematic error attributed to each measured  $F_2^{diff}$  point, was obtained by adding in quadrature deviations from the nominal  $F_2^{diff}$  value for each systematic check.

## 8.5 Test of the factorization theorem

In order to check the factorization theorem discussed in section 2, (formula (2.31)) we have investigated whether the  $x_P$ -dependence of  $F_2^{diff}$  is the same in each  $(\beta, Q^2)$  bin. We have performed a global fit to the all data points of the form:

$$a_i \cdot (x_P)^b \quad (8.16)$$

where the normalizations  $a_i$  were allowed to differ in different  $(\beta, Q^2)$  bins, but the exponent should be the same. The results of the fit are shown in Fig.8.6. Within the experimental errors the data are consistent with the constant slope:

$$b = -1.25 \pm 0.07(\text{stat}) \pm 0.09(\text{sys}) \quad (8.17)$$

The statistical error is obtained when the fitted points were assumed to have only statistical errors. The systematic error was calculated by refitting the measured data points obtained by different systematic checks and adding deviations from the central value of  $b$  in quadrature. The  $\chi^2$  values for each  $(\beta, Q^2)$  bin were between 0.05 and 1.5 per degree of freedom.

The results are consistent with an independent analysis performed by the ZEUS Collaboration ( $b = -1.3 \pm 0.08(\text{stat})_{-0.14}^{+0.08}(\text{sys})$ ) [63] and with recent results from the H1 Collaboration ( $b = -1.19 \pm 0.06(\text{stat}) \pm 0.07(\text{sys})$ ) [64].

$Q^2$ (GeV <sup>2</sup> )	$\beta$	$x_F$	Nominal $F_2^{diff} \pm (stat)$	Systematic checks			
				$E' > 10$	EEXOTIC	$y_{JB} > 0.03$	$y_{JB} > 0.05$
10	0.175	0.00205	23.4 ± 2.0	24.2	26.5	23.4	23.4
10	0.175	0.00325	10.4 ± 0.9	10.9	11.9	10.4	10.2
10	0.175	0.00515	5.4 ± 0.5	5.6	6.0	5.6	5.3
10	0.175	0.00815	3.6 ± 0.7	3.5	3.6	4.0	3.3
10	0.375	0.00130	36.9 ± 3.5	38.2	45.2	36.9	37.1
10	0.375	0.00205	25.6 ± 2.5	26.4	29.5	25.6	24.5
10	0.375	0.00325	13.7 ± 1.5	13.9	14.6	13.9	12.4
10	0.375	0.00515	6.3 ± 1.1	6.3	6.6	5.7	9.6
10	0.650	0.00081	42.0 ± 5.1	43.4	56.6	42.0	41.9
10	0.650	0.00130	35.8 ± 4.9	36.5	42.6	35.8	35.1
10	0.650	0.00205	16.5 ± 2.7	16.5	16.8	16.9	14.8
10	0.650	0.00325	7.8 ± 1.5	7.8	8.3	7.5	9.0
15	0.175	0.00205	30.8 ± 3.5	31.2	31.8	30.8	30.8
15	0.175	0.00325	13.0 ± 1.2	13.6	13.8	13.0	13.1
15	0.175	0.00515	6.3 ± 0.6	6.4	6.7	6.7	6.4
15	0.175	0.00815	3.0 ± 0.4	5.0	5.4	5.6	5.5
15	0.375	0.00130	40.0 ± 4.0	41.2	43.4	40.0	40.0
15	0.375	0.00205	21.7 ± 2.1	22.4	25.5	21.7	21.8
15	0.375	0.00325	15.3 ± 1.6	15.4	16.8	15.5	15.5
15	0.375	0.00515	5.0 ± 0.6	3.0	3.2	3.6	3.1
15	0.650	0.00081	39.4 ± 5.0	41.2	50.1	39.4	39.4
15	0.650	0.00130	28.7 ± 3.5	29.5	34.8	28.6	28.8
15	0.650	0.00205	17.1 ± 2.2	17.1	16.8	17.1	17.2
15	0.650	0.00325	10.2 ± 1.3	10.1	10.3	10.2	10.0
32	0.175	0.00205	24.6 ± 4.0	27.6	26.1	24.6	24.6
32	0.175	0.00325	9.9 ± 1.1	11.1	10.0	9.9	9.9
32	0.175	0.00515	6.0 ± 0.7	6.7	6.3	6.0	6.0
32	0.175	0.00815	3.2 ± 0.4	3.3	3.1	3.2	3.1
32	0.375	0.00205	23.2 ± 2.5	24.8	23.6	23.2	23.1
32	0.375	0.00325	18.2 ± 2.0	18.8	17.7	18.1	18.1
32	0.375	0.00515	13.3 ± 1.7	13.5	12.9	13.2	13.2
32	0.650	0.00130	29.0 ± 3.7	29.3	28.9	29.0	29.0
32	0.650	0.00205	18.2 ± 2.3	18.5	18.2	18.2	18.2
32	0.650	0.00325	10.4 ± 1.4	10.4	10.3	10.3	10.5

Table 8.2:  $F_2^{diff}$  extracted under different conditions. The values of  $F_2^{diff}$  are tabulated for the different systematic checks. The values of  $Q^2$ ,  $\beta$  and  $x_F$  at which  $F_2^{diff}$  is specified are listed.

$Q^2$ ( $\text{GeV}^2$ )	$\beta$	$x_F$	Nominal $F_2^{diff} \pm (\text{stat})$	Systematic checks			
				$30 < \delta < 60$	$40 < \delta < 60$	$\eta_{max} < 1$	$\eta_{max} < 2$
10	0.175	0.00205	$23.4 \pm 2.0$	24.0	23.8	23.1	23.5
10	0.175	0.00325	$10.4 \pm 0.9$	10.1	10.3	10.5	10.1
10	0.175	0.00515	$5.4 \pm 0.5$	5.4	5.4	6.2	5.4
10	0.175	0.00815	$3.6 \pm 0.7$	3.6	3.5	5.8	3.7
10	0.375	0.00130	$36.9 \pm 3.5$	37.0	37.4	37.3	36.9
10	0.375	0.00205	$25.6 \pm 2.5$	25.6	24.2	24.3	25.4
10	0.375	0.00325	$13.7 \pm 1.5$	13.6	12.6	14.0	13.5
10	0.375	0.00515	$6.3 \pm 1.1$	6.3	6.0	6.5	5.9
10	0.650	0.00081	$42.0 \pm 5.1$	41.9	45.2	42.8	42.0
10	0.650	0.00130	$35.8 \pm 4.9$	35.8	36.1	35.9	35.8
10	0.650	0.00205	$16.5 \pm 2.7$	16.5	13.5	16.0	16.4
10	0.650	0.00325	$7.8 \pm 1.5$	7.8	6.7	7.8	6.9
15	0.175	0.00205	$30.8 \pm 3.5$	30.7	28.5	30.2	30.5
15	0.175	0.00325	$13.0 \pm 1.2$	12.8	12.6	13.2	12.2
15	0.175	0.00515	$6.3 \pm 0.6$	6.1	6.0	7.1	6.1
15	0.175	0.00815	$3.0 \pm 0.4$	3.0	3.0	3.8	3.1
15	0.375	0.00130	$40.0 \pm 4.0$	40.1	37.8	40.4	39.6
15	0.375	0.00205	$21.7 \pm 2.1$	21.5	20.4	21.6	21.0
15	0.375	0.00325	$15.3 \pm 1.6$	15.3	14.6	15.5	15.2
15	0.375	0.00515	$5.0 \pm 0.6$	5.0	5.0	6.1	5.2
15	0.650	0.00081	$39.4 \pm 5.0$	39.5	40.4	39.6	39.4
15	0.650	0.00130	$28.7 \pm 3.5$	28.6	28.5	28.7	28.7
15	0.650	0.00205	$17.1 \pm 2.2$	17.1	16.6	16.8	17.0
15	0.650	0.00325	$10.2 \pm 1.3$	10.2	9.6	10.2	10.4
32	0.175	0.00205	$24.6 \pm 4.0$	25.3	22.1	24.1	24.1
32	0.175	0.00325	$9.9 \pm 1.1$	9.9	9.2	9.6	9.6
32	0.175	0.00515	$6.0 \pm 0.7$	5.9	6.0	5.7	5.7
32	0.175	0.00815	$3.2 \pm 0.4$	3.2	3.2	2.9	2.9
32	0.375	0.00205	$23.2 \pm 2.5$	23.2	22.4	23.0	23.0
32	0.375	0.00325	$18.2 \pm 2.0$	18.2	17.0	17.8	17.8
32	0.375	0.00515	$13.3 \pm 1.7$	13.2	13.1	12.3	12.3
32	0.650	0.00130	$29.0 \pm 3.7$	28.9	29.3	29.0	29.0
32	0.650	0.00205	$18.2 \pm 2.3$	18.2	17.8	18.1	18.1
32	0.650	0.00325	$10.4 \pm 1.4$	10.5	10.1	10.4	10.4

Table 8.3:  $F_2^{diff}$  extracted under different conditions, continued.

$Q^2$ (GeV <sup>2</sup> )	$\beta$	$x_P$	Nominal $F_2^{diff} \pm (stat)$	Systematic checks			
				$ V_z  < 30$	$ V_z  < 50$	# iter	HP
10	0.175	0.00205	23.4 ± 2.0	23.5	23.3	23.2	22.0
10	0.175	0.00325	10.4 ± 0.9	10.5	10.2	10.3	9.2
10	0.175	0.00515	5.4 ± 0.5	5.4	5.4	5.4	7.5
10	0.175	0.00815	3.6 ± 0.7	3.6	3.6	3.3	3.8
10	0.375	0.00130	36.9 ± 3.5	36.9	36.9	36.8	33.0
10	0.375	0.00205	25.6 ± 2.5	25.9	25.8	25.6	22.0
10	0.375	0.00325	13.7 ± 1.5	13.9	13.8	13.5	11.8
10	0.375	0.00515	6.3 ± 1.1	6.3	6.3	6.0	8.0
10	0.650	0.00081	42.0 ± 5.1	41.9	42.1	41.8	65.2
10	0.650	0.00130	35.8 ± 4.9	36.0	36.4	35.9	35.2
10	0.650	0.00205	16.5 ± 2.7	16.5	16.5	16.5	9.2
10	0.650	0.00325	7.8 ± 1.5	7.8	7.8	7.6	7.8
15	0.175	0.00205	30.8 ± 3.5	31.5	30.9	29.9	29.0
15	0.175	0.00325	13.0 ± 1.2	13.3	13.1	12.4	14.3
15	0.175	0.00515	6.3 ± 0.6	6.3	6.3	5.8	7.6
15	0.175	0.00815	3.0 ± 0.4	3.1	3.1	2.8	4.2
15	0.375	0.00130	40.0 ± 4.0	39.4	40.0	39.4	34.1
15	0.375	0.00205	21.7 ± 2.1	21.7	21.8	20.6	18.5
15	0.375	0.00325	15.3 ± 1.6	15.4	15.4	14.0	16.5
15	0.375	0.00515	5.0 ± 0.6	5.0	5.1	4.7	5.6
15	0.650	0.00081	39.4 ± 5.0	38.1	39.1	39.5	53.7
15	0.650	0.00130	28.7 ± 3.5	27.8	29.0	27.2	31.0
15	0.650	0.00205	17.1 ± 2.2	17.1	17.3	15.0	16.6
15	0.650	0.00325	10.2 ± 1.3	10.1	10.3	9.1	9.5
32	0.175	0.00205	24.6 ± 4.0	24.4	24.4	22.8	23.2
32	0.175	0.00325	9.9 ± 1.1	9.7	9.7	9.2	10.9
32	0.175	0.00515	6.0 ± 0.7	5.9	6.0	5.7	6.4
32	0.175	0.00815	3.2 ± 0.4	3.2	3.4	3.1	2.4
32	0.375	0.00205	23.2 ± 2.5	22.9	22.6	22.7	19.8
32	0.375	0.00325	18.2 ± 2.0	17.6	17.6	17.8	16.6
32	0.375	0.00515	13.3 ± 1.7	13.1	13.3	13.0	10.0
32	0.650	0.00130	29.0 ± 3.7	29.2	28.4	28.3	26.9
32	0.650	0.00205	18.2 ± 2.3	18.2	18.0	17.1	14.4
32	0.650	0.00325	10.4 ± 1.4	10.4	10.4	9.8	10.5

Table 8.4:  $F_2^{diff}$  extracted under different conditions, continued.

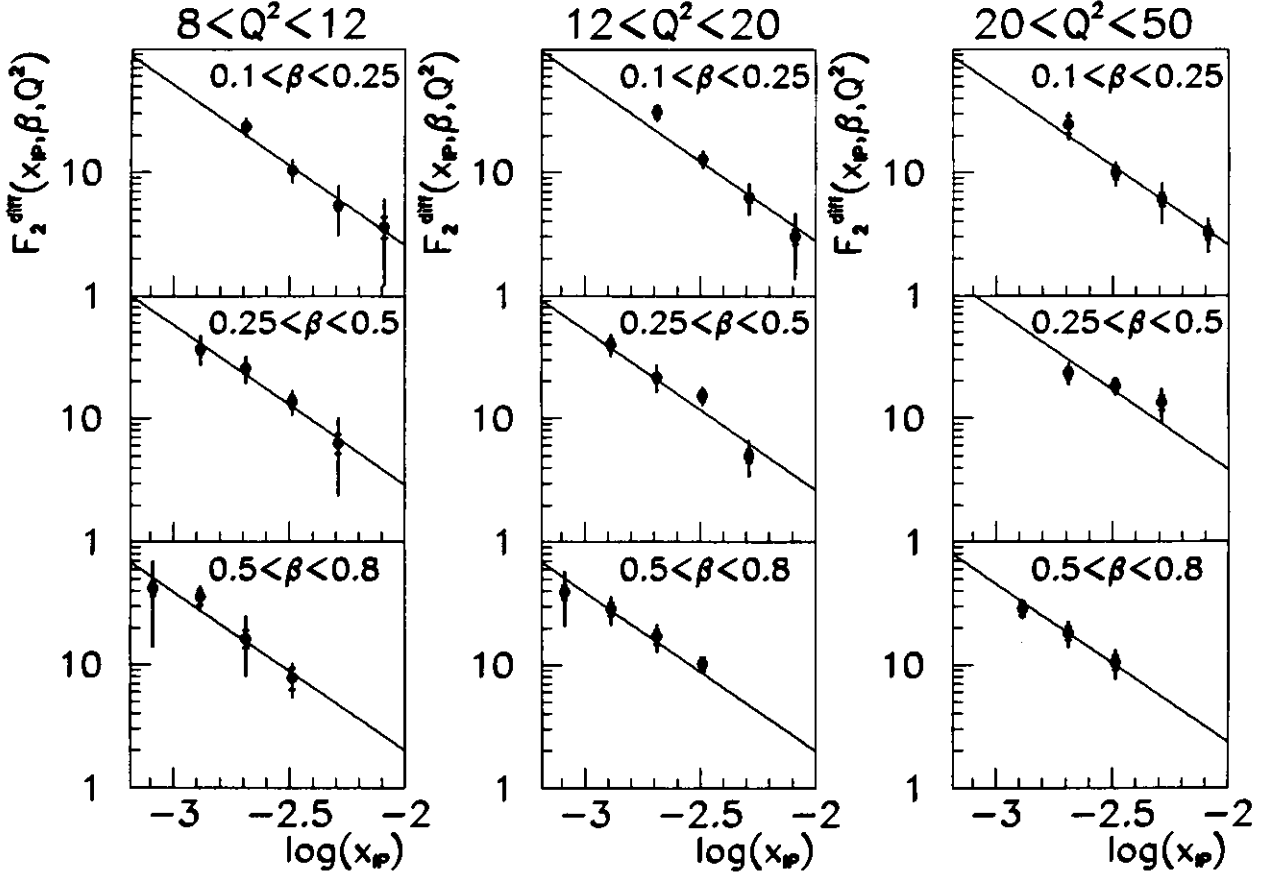


Figure 8.6: Test of factorization of  $F_2^{diff}$ . The solid lines are the results of the global fit of the function (8.16) to the data points which are represented as full dots. The inner error bars show statistical errors, the full error bars correspond to the statistical and systematic errors added in quadrature. The data include an estimated 15% contribution due to double dissociation. The overall normalization uncertainty of 2.5% due to the luminosity uncertainty is not included.

The  $\beta$  and  $Q^2$  dependences of the  $F_2^{diff}$  were obtained by integration over the measured range of  $x_P$ :

$$F_2^{diff}(\beta, Q^2) = \int_{x_P^{low}}^{x_P^{high}} F_2^{diff}(x_P, \beta, Q^2) dx_P \quad (8.18)$$

where  $x_P^{low} = 6.3 \cdot 10^{-4}$  and  $x_P^{high} = 10^{-2}$ . We integrated the fitted  $x_P$  dependence, hence we assumed that the factorization theorem holds in the range of integration. The resulting function  $F_2^{diff}(\beta, Q^2)$  is proportional to the structure function of the pomeron. The  $\beta$  and  $Q^2$  dependences of  $F_2^{diff}(\beta, Q^2)$  are shown in Fig.8.7.

The  $F_2^{diff}(\beta, Q^2)$  values as a function of  $\beta$  for fixed  $Q^2$  are consistent with a flat  $\beta$  dependence as expected from the aligned jet model [65]. For fixed  $\beta$  the  $F_2^{diff}(\beta, Q^2)$  is

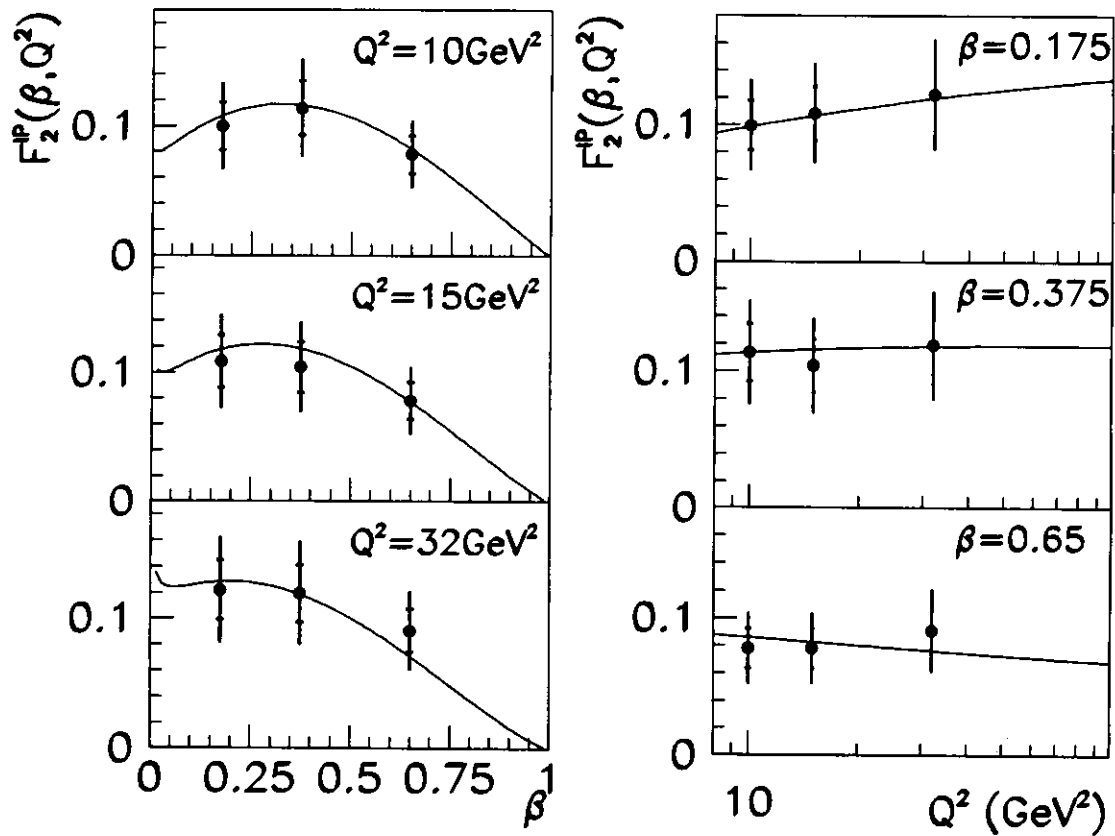


Figure 8.7: Results of  $F_2^P(\beta, Q^2)$  compared to the predictions of [18] indicated as a solid line. The inner error bars correspond to the statistical errors, the outer error bars correspond to the statistical and systematic errors added in quadrature. The systematic errors combine in quadrature the fits of the  $x_P$  dependence due to each of the systematic checks discussed in the text. The overall normalization is determined by the experimental integration limits over  $x_P$  ( $6.3 \cdot 10^{-4} < x_P < 10^{-2}$ ). The data include an estimated 15% contribution due to double dissociation. The overall normalization uncertainty of 2.5% due to the luminosity uncertainty is not included.

approximately independent of  $Q^2$  which is consistent with scattering off point-like partons within the pomeron.

There are analysis of the pomeron structure functions based on QCD evolution equations with different phenomenologically motivated parametrisations of initial parton distributions in the pomeron. They predict a very mild scaling violation of  $F_2^P$  with  $Q^2$  [18, 66, 67].

In Fig.8.7, we have compared the results of the measurements with predictions of  $\beta$  and  $Q^2$  dependence of [18]. The authors proposed the following parton distributions in

the pomeron at the reference scale  $Q_0^2 = 4 \text{ GeV}^2$ :

$$\begin{aligned}
\beta u^{\mathbf{P}}(\beta, Q_0^2, t) &= 0.4(1 - \delta)S^{\mathbf{P}}(\beta) \\
\beta d^{\mathbf{P}}(\beta, Q_0^2, t) &= 0.4(1 - \delta)S^{\mathbf{P}}(\beta) \\
\beta s^{\mathbf{P}}(\beta, Q_0^2, t) &= 0.2(1 - \delta)S^{\mathbf{P}}(\beta) \\
\beta c^{\mathbf{P}}(\beta, Q_0^2, t) &= \delta S^{\mathbf{P}}(\beta) \\
\beta g^{\mathbf{P}}(\beta, Q_0^2, t) &= (0.218\beta^{-0.08} + 3.09\beta)(1 - \beta)
\end{aligned} \tag{8.19}$$

where the function  $S^{\mathbf{P}}(\beta)$  is parameterized as follow:

$$S^{\mathbf{P}}(\beta) = (0.0528\beta^{-0.08} + 0.801\beta)(1 - \beta) \tag{8.20}$$

and  $\delta = 0.02$  [68]. The parton distributions defined by equations (8.19) and (8.20) were next evolved up to the values of  $Q^2$  for the measured points using the LO GLAP equations.

The agreement with the data is very good for both the shape in  $\beta$  as well as the evolution with  $Q^2$ .

In Fig.8.8 we present the prediction of [18] for the  $x_{\mathbf{P}}$  dependence of  $F_2^{\text{diff}}(x_{\mathbf{P}}, \beta, Q^2)$ . The factorization property (2.31) and the value of intercept  $\alpha_{\mathbf{P}}(0) = 1.1$  are built into this model. We have subtracted from the data the estimated 15% of double dissociative events in order to compare with this model. Again we see that the analyzed data confirm very well this assumptions.

## 8.6 Comparison with theoretical models

In this paragraph, we will compare the results of  $F_2^{\text{diff}}(x_{\mathbf{P}}, \beta, Q^2)$  measurement with theoretical models of single diffractive dissociation discussed in section 2. We have subtracted from the data the estimated 15% of double dissociative events in order to compare with these models. The measured data points and the models are compared in Fig.8.9.

At high  $\beta$ -values the predictions of Nikolaev–Zakharov and Donnachie–Landshoff are in reasonable agreement with the data. At smaller  $\beta$ -values, the Donnachie–Landshoff model underestimates the observed  $F_2^{\text{diff}}$ , because it includes only a hard component of the pomeron structure function. The Nikolaev–Zakharov prediction, which also include a soft component, describes the data also at smaller  $\beta$ -values. The analysis performed in this thesis is unable to observe the factorization breaking effects predicted by Nikolaev–Zakharov model. In both above considered models, the momentum sum rule for quarks is not satisfied.

The Ingelman–Schlein model with a hard pomeron structure function for which the momentum sum rule is assumed for the light quarks, predicts values of  $F_2^{\text{diff}}$  above the measured ones. Hence the data break the model in this form. There are two possibilities to make the model more consistent with the recent measurements:

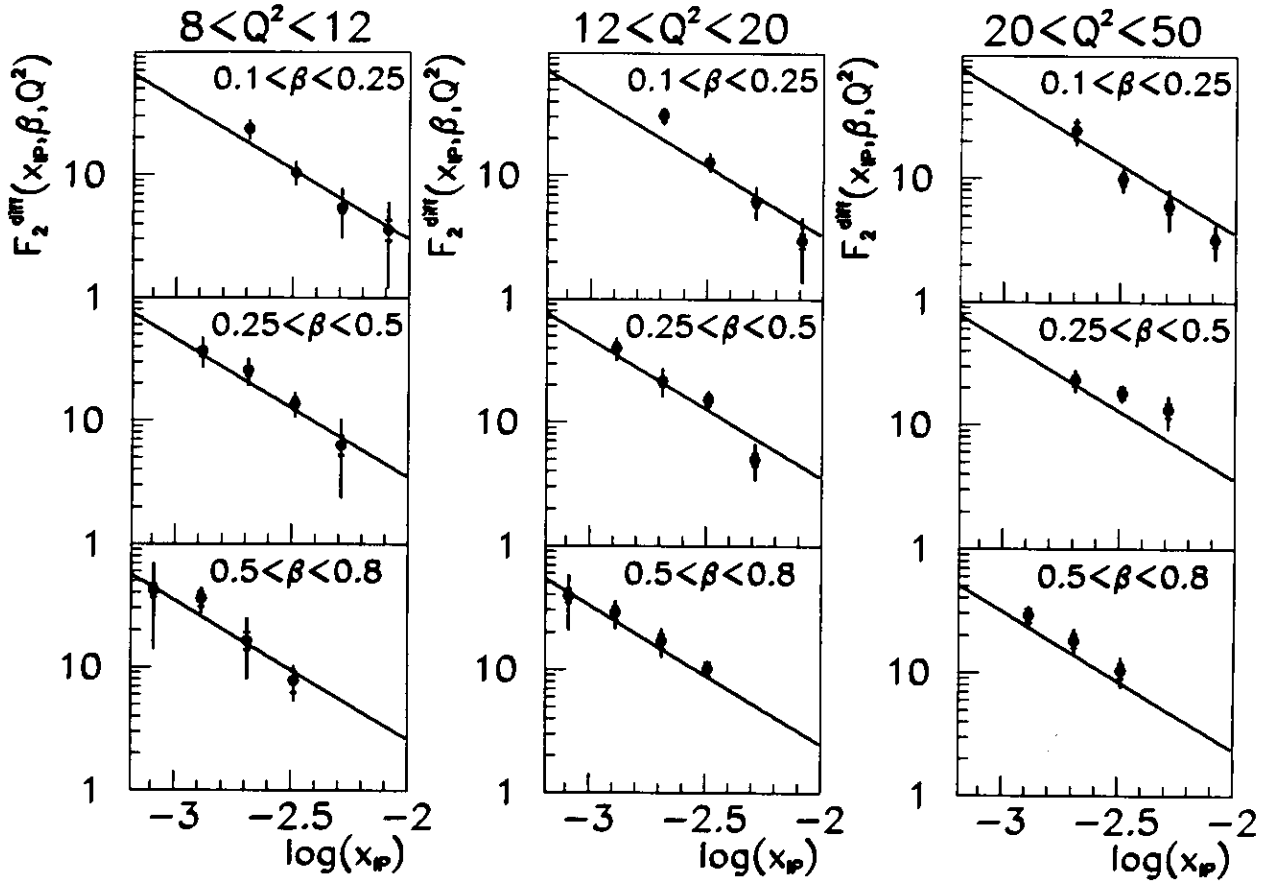


Figure 8.8: Results of  $F_2^{diff}(x_P, \beta, Q^2)$  compared to the predictions of [18] indicated as a solid line. The inner error bars show statistical errors, the full error bars correspond to the statistical and systematic errors added in quadrature. The overall normalization uncertainty of 2.5% due to the luminosity uncertainty and 10% due to the subtraction of the double dissociation events is not included.

- a) One can change the  $\beta$  spectrum of valence quarks by adding more soft quarks. Then one can still require the momentum sum rule to be fulfilled.
- b) One can allow for existence of gluons and use the GLAP evolution equations.

In the framework of Regge theory, the results can be interpreted as a hadronic exchange in  $t$ -channel which couples to the incident proton. The dependence of  $F_2^{diff}(x_P, \beta, Q^2)$  on  $x_P$  can be interpreted as the intercept:

$$\alpha(0) = 1.13 \pm 0.04(\text{stat}) \pm 0.05(\text{sys})$$

of the leading Regge trajectory. Within the experimental errors the results are still consistent with the Donnachie–Landshoff intercept. The measured value is inconsistent with

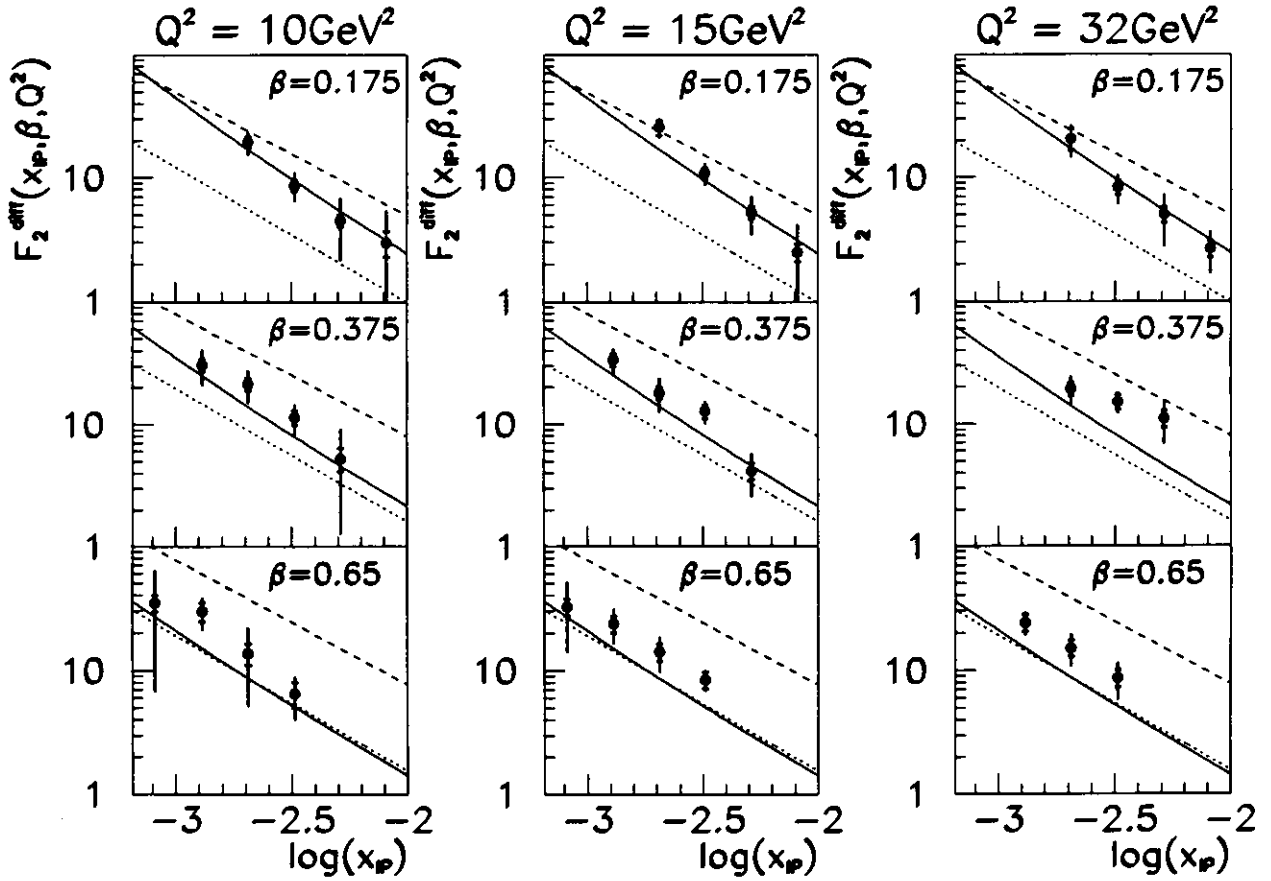


Figure 8.9: Results of  $F_2^{diff}(x_P, \beta, Q^2)$  (full dots) compared to various theoretical models: Nikolaev-Zakharov (solid line), Ingelman-Schlein (dashed line) and Donnachie-Landshoff (dotted line). The inner error bars show statistical errors, the full error bars correspond to the statistical and systematic errors added in quadrature. The overall normalization uncertainty of 2.5% due to the luminosity uncertainty and 10% due to the subtraction of the double dissociation events is not included.

the intercept of the leading meson Regge trajectories ( $\alpha(0) = 0.5$ ), which suggest that the colorless object in the proton responsible for diffractive deep inelastic scattering is the pomeron. The precision of the measurements does not exclude the higher intercept, more consistent with BFKL motivated pomeron.

## 9 Conclusions

The measurement of the proton diffractive structure function in deep inelastic  $ep$  scattering at HERA has been presented. In the analysis the full 1993 ZEUS data sample, which corresponds to the integrated luminosity of about  $540 \text{ nb}^{-1}$ , has been used.

Diffractive deep inelastic events were selected by the requirement of a large rapidity gap between the diffractively scattered proton and the rest of the hadronic system. Comparison of the data with Monte Carlo predictions (POMPYT and EPDIFFR) showed that both models generally described the inclusive distributions of the observed kinematic variables. However the distributions of  $m_X$  and  $\beta$  are more consistent with models where along with the hard, also the soft component is present in the pomeron structure function. This is why the Nikolaev–Zakharov model was used for unfolding of the data.

The proton diffractive structure function  $F_2^{diff}$  has been measured as a function of  $x_P$  (fraction of the proton momentum carried by the pomeron), of  $\beta$  (fraction of the pomeron momentum carried by a struck quark) and of  $Q^2$ . It was not possible to measure  $t$ , the momentum transfer squared to the proton, and therefore the results are integrated over  $t$ . The proton diffractive structure function  $F_2^{diff}$  was measured in the kinematic range of  $6.5 \cdot 10^{-4} < x_P < 10^{-2}$ ,  $0.1 < \beta < 0.8$  and  $8 < Q^2 < 50 \text{ GeV}^2$ . The data show that  $F_2^{diff}$  falls rapidly for fixed  $\beta$  and  $Q^2$  as a function of  $x_P$ . Within the experimental errors, the data show factorization of the proton diffractive structure function to the pomeron flux in the proton and to the pomeron structure function. The universal  $x_P$  dependence of  $F_2^{diff}$  in all  $(\beta, Q^2)$  bins has been found to be:

$$F_2^{diff}(x_P, \beta, Q^2) \sim (x_P)^b$$

where  $b = -1.25 \pm 0.07(\text{stat}) \pm 0.09(\text{sys})$ .

Using the data considered in this analysis we are unable to observe the factorization breaking effects predicted by the Nikolaev–Zakharov model. The diffractive structure function is well described by the Nikolaev–Zakharov model, although this model does not use the concept of a particle-like pomeron.

In the measured  $Q^2$  range the pomeron structure function scales with  $Q^2$  at fixed  $\beta$ . However, a mild scaling violation is not excluded. The data is in a good agreement with the model [18] based on factorization and QCD evolution equations, which leads to scaling violation in this model. The gluon content of the pomeron can only indirectly manifest itself through the QCD evolution of the pomeron structure function with  $Q^2$ . The relatively large gluon distribution in the pomeron with a hard spectrum  $(1 - \beta)$  is responsible for increase of the pomeron structure function with  $Q^2$  at fixed  $\beta$  up to relatively large values of  $\beta \approx 0.5$ . It should be noted that the proton structure function starts to decrease with increasing  $Q^2$  already for  $x_{Bj} > 0.1$ .

$F_2^P$  has not vanishing values for a significant range of  $\beta$ . The  $\beta$  dependence of the pomeron structure function requires both a hard and a soft component for the quark content of the pomeron. At moderate  $\beta$  values, the pomeron structure function is dominated by the hard component. The soft component is important at the small values of  $\beta$  – this fact could be attributed to the QCD evolution [18].

No scaling violation (or a very mild one, described by standard perturbative QCD evolution equations) support the idea of the pomeron in the diffractive deep inelastic  $ep$  scattering behaving effectively as a particle, which consists of point-like constituents.

## Acknowledgments

I am very grateful to Professor Danuta Kisielewska and to Professor Andrzej Eskreys for their constant encouragements during the writing of this thesis.

I would like to thank Professor Jan Kwieciński for his suggestion of working on diffraction in DIS.

I thank Professor Marek Jeżabek for a critical reading of the manuscript and very useful comments.

I would like to thank Dr Krzysztof Golec for many useful discussions and comments about the theory of diffractive physics.

I would like to thank my colleagues from the ZEUS experiment, especially from the LUMI group, for fruitful cooperation. The collaboration with Leszek Adamczyk, Dr Krzysztof Piotrkowski and Dr Leszek Zawiejski was very important for my work.

I wish to thank the Directorate of the DESY laboratory for supporting my stay in Hamburg.

And last but not least, I am very grateful to Wojciech Świętek for his work on correcting my English style.

## Bibliography

- [1] ZEUS Collaboration, M.Derrick et al., *Phys. Lett.* **B316**(1993)412,  
ZEUS Collaboration, M.Derrick et al., *Z. Phys.* **C65**(1995)379.
- [2] H1 Collaboration, T.Ahmed et al., *Nucl. Phys.* **B407**(1993)515.  
H1 Collaboration, T.Ahmed et al., *Phys. Lett.*, **B348**(1995)681.
- [3] ZEUS Collaboration, M.Derrick et al., *Phys. Lett.* **B315**(1993)481.
- [4] H1 Collaboration, T.Ahmed et al., *Nucl. Phys.* **B429**(1994)477.
- [5] UA8 Collaboration, R.Bonino et al., *Phys. Lett.* **B211**(1988)239,  
UA8 Collaboration, A.Brandt et al., *Phys. Lett.* **B297**(1992)417.
- [6] J.D.Bjorken, *Phys. Rev.* **179**(1969)1547.
- [7] J.I.Friedman and H.W.Kendall, *Ann. Rev. Nucl. Sci.* **22**(1972)203.
- [8] C.G.Callan and D.J.Gross, *Phys. Rev. Lett.* **22**(1969)156.
- [9] A.Bodek, et al., *Phys. Rev.* **D20**(1979)1471.
- [10] J. Kwieciński, *Small x physics*, INP-1620-PH (1993).
- [11] J.Kwieciński, *J. Phys.* **G19**(1993)1443.
- [12] B. Badelek, M.Krawczyk, K.Charchuła and J. Kwieciński, *J. Rev. Mod. Phys.* **64**(1992)927
- [13] F.Halzen and A.D.Martin, *Quarks and Leptons: An introductory course in modern particle physics*, John Wiley & Sons, Inc., New York (1984).
- [14] R.G.Roberts, *The structure of the proton*, Cambridge University Press, Cambridge (1990).
- [15] G.Altarelli and G.Parisi, *Nucl. Phys.* **B126**(1977)298.
- [16] V.N.Gribov and L.N.Lipatov, *Sov. Jour. Nucl. Phys.* **15**(1972)438.
- [17] J.D.Bjorken, Eilat Workshop (1994).
- [18] K.Golec-Biernat and J.Kwieciński, *QCD analysis of deep inelastic scattering at HERA*, INP Report PH/1670..
- [19] G.Ingelman and P.E.Schlein, *Phys. Lett.* **B152**(1985)256.
- [20] G.Ingelman, Partons and QCD effects in the Pomeron, DESY 1993-109.

- [21] G.Ingelman and K.Prytz, *Z.Phys.* **C58**(1993)285.
- [22] K.Prytz, *Antishadowing contribution to the Pomeron structure function*, RAL-94-054.
- [23] L.V.Gribov, E.M.Levin and M.G.Ryskin, *Phys. Rep.* **100**(1983)1.
- [24] A.Donnachie and P.V.Landshoff, *Nucl. Phys.* **B244**(1984)322.
- [25] A.Donnachie and P.V.Landshoff, *Phys. Lett.* **B191**(1987)309.
- [26] A.Donnachie and P.V.Landshoff, *Nucl. Phys.* **B303**(1988)634.
- [27] N.N.Nikolaev and B.G.Zakharov, *Phys. Lett.* **B260**(1991)414.
- [28] N.N.Nikolaev and B.G.Zakharov, *Z. Phys.* **C53**(1992)331.
- [29] M.Genovese, N.N.Nikolaev and B.G.Zakharov, *KFA-IKP-1994/37* and *CERN-Th.13/95*.
- [30] N.N.Nikolaev and B.G.Zakharov, *Phys. Lett.* **B327**(1994)149.
- [31] N.N.Nikolaev and B.G.Zakharov, *Z. Phys.* **C49**(1991)607.
- [32] ZEUS Collaboration, *The ZEUS detector, Status Report 1993*, DESY.
- [33] K.Piotrkowski and M.Zachara, *Determination of the ZEUS luminosity in '93*, ZEUS Note 94-167.
- [34] I.Ali et al., *The ZEUS calorimeter first level trigger*, preprint DESY 94-183.
- [35] F.Chlebana, *First measurement of the proton structure function  $F_2$  with the ZEUS detector*, Ph.D. Thesis, Internal Report DESY F35D-94-02.
- [36] E.Gallo, S.Nickel and J.K.Sedgbeer, *The 1993 TLT and DST selection of the structure function group*, ZEUS Note 94-26.
- [37] S.Bentvelsen, J.Engelen and P.Kooijman, *Proc. of the DESY Workshop 'Physics at HERA*. Ed. W.Buchmüller and G.Ingelman. Hamburg (1991)23.
- [38] A.Caldwell et al., *An electron energy correction method*, ZEUS Note 94-051.
- [39] F.Jacquet and A.Blondel, in *An ep facility for Europe*, Proc. Hamburg (1979)391.
- [40] S.Magill, *Energy corrections to jets in the ZEUS calorimeter*, ZEUS Note 94-042.
- [41] J.Biltzinger, *Effect of noise on the reconstruction of kinematical variables in DIS events*, ZEUS Note 93-073.
- [42] D.Bandyopadhyay et al., *VCTRAK: Offline output information*, ZEUS Note 93-122.

- [43] R.Brun et al., *GEANT 3.13*, CERN DD/EE/84-1 (1987).
- [44] S.M.Fisher and P.Palazzi, *The ADAMO data system*, RAL/CERN Documentation.
- [45] G.Ingelman, *LEPTO 6.1 - The Lund Monte Carlo for deep inelastic lepton-nucleon scattering*, Proc. of the DESY Workshop 'Physics at HERA. Ed. W.Buchmüller and G.Ingelman. Hamburg (1991)1366.
- [46] A.Kwiatkowski et al., *HERACLES 4.1 - An event generator for ep interactions at HERA*. Proc. of the DESY Workshop 'Physics at HERA. Ed. W.Buchmüller and G.Ingelman. Hamburg (1991)1294.
- [47] K.Charchula, G.Schuler and H.Spiesberger, *Comp. Phys. Comm.*, **81**(1994)381.
- [48] A.D.Martin, R.G.Roberts and W.J.Stirling, *Phys.Lett.* **B306**(1993)145.
- [49] L.Lonnblad, *ARIADNE v. 4*, Proc. of the DESY Workshop 'Physics at HERA. Ed. W.Buchmüller and G.Ingelman. Hamburg (1991)1440.
- [50] P.Bruni and G.Ingelman, *POMPYT 1.0 - A Monte Carlo to simulate diffractive hard scattering processes*, (unpublished).
- [51] H.U.Bengtsson and T.Sjöstrand, *PYTHIA 5.6*, *Comp. Phys. Comm.* **46**(1987)43;  
T.Sjöstrand, Proc. of the DESY Workshop 'Physics at HERA. Ed. W.Buchmüller and G.Ingelman. Hamburg (1991)1405.
- [52] T.Sjöstrand, *Comp. Phys. Comm.* **71**(1986)347;  
T.Sjöstrand and M.Bengtsson, *Comp. Phys. Comm.* **43**(1987)367.
- [53] A.Solano, Ph.D. Thesis, University of Torino 1993 (unpublished).
- [54] L.Lamberti and A.Solano, *How to use MC weights for physics analysis*, ZEUS Note 94-091.
- [55] ZEUS Collaboration, PHANTOM - Physics analysis techniques, operations and methods - Collection of subroutines/functions and packages of routines for data analysis.
- [56] T.Doeker, A.Frey and M.Nakao, *Electron position reconstruction*, ZEUS Note 94-123.
- [57] H.Abramowicz et al., *A determination of  $F_2$  with the 1992 data*, ZEUS Note 93-078.
- [58] E.Barberis et al., *On the properties of diffractive events in deep inelastic ep scattering*. ZEUS Note 94-037.
- [59] ZEUS Collaboration, M.Derrick et al., *Comparison of energy flows in Deep Inelastic Scattering with and without a large rapidity gap*, DESY 94-117.
- [60] ZEUS Collaboration, M.Derrick et al., *Phys. Lett.* **B332**(1994)228.

- [61] V.Blobel, *Unfolding methods in high energy physics experiments*, DESY 84-118.  
N.D.Gagunashvili, *Unfolding of true distributions from experimental data distorted by detectors with finite resolutions*, *Nucl. Instrum. Meth.* **A343**(1994)606.
- [62] G.D'Agostini, *A multidimensional unfolding method based on Bayes' theorem*, preprint DESY 94-099.
- [63] ZEUS Collaboration, M.Derrick et al., *Measurement of the diffractive structure function in deep inelastic scattering at HERA*, DESY 95-093.
- [64] H1 Collaboration, T.Ahmed et al., *First measurement of the deep inelastic structure of proton diffraction*, DESY 95-036.
- [65] J.D.Bjorken and J.Kogut, *Phys. Lett.* **B335**(1994)479.
- [66] A.Capella et al., *Phys. Lett.* **B343**(1995)403.
- [67] T.Gehrmann and W.J.Stirling, DTP/95/26.
- [68] A.D.Martin, R.G.Roberts and W.J.Stirling, *Phys. Rev.* **D50**(1994)6734,  
A.D.Martin, R.G.Roberts and W.J.Stirling, DTP/95/14 (RAL-95-021).

